NATIONAL ACADEMY OF SCIENCES OF UKRAINE ● G. V. KURDYUMOV INSTITUTE FOR METAL PHYSICS

A MONTHLY RESEARCH JOURNAL

METALLOPHYSICS AND ADVANCED TECHNOLOGIES

(Metallofizika i Noveishie Tekhnologii)

FOUNDED IN SEPTEMBER, 1979

Volume 48, No. 9; September 2026

CONTENTS

Editorial Announcements	Information for Foreign Subscribers	V
	Information for Contributors	VII
Amorphous and Liquid States	The Hall Effect, Electrical Resistivity, and Spin–Orbit Interaction Parameters in Amorphous Alloys of the Fe–Cr–B System *O. K. KUVANDIKOV, I. SUBKHANKULOV, N. S. HAMRAEV, R. M. RAZHABOV, Sh. A. KHOMITOV, and O. Z. TURGUNOV*	919
Crystal-Lattice Defects	Length of a Critical Dislocation Segment under the Influence of Thermal Fluctuations *M. I. LUGOVY, D. G. VERBYLO, M. P. BRODNIKOVSKYY, T. I. VERBYTSKA, D. S. LEONOV, and M. Yu. BARABASH*	931
Physics of Strength and Plasticity	On the Effect of Residual Stresses on the Strength of Oxidized Plates under Thermomechanical Loading *I. P. SHATSKYI, V. M. PETRASHCHUK, L. Ya. ROPYAK, and O. O. LAZARIEVA*	949
New Metallic Materials and Synthetic Metals	Synthesis and Characterization of a Ti_3SiC_2–TiC–$TiSi_2$ Composite for High-Temperature Applications *I. M. KIRIAN, A. M. LAKHNIK, M. A. SKORYK, S. O. KOTRECHKO, O. V. ZATSARNA, T. O. MONASTYRSKA, I. V. GURIN, and O. D. RUD*	963
	Mechanism of *in situ* WC Formation during Mechanical Alloying of the Medium-Entropy $W_{1.5}$FeCoNi Alloy *S. Yu. TESLIA, O. I. YURKOVA, D. S. LEONOV, and P. I. LOBODA*	973
Medical Metals	Characteristic Features of the Selective Dissolution of	

© G. V. Kurdyumov Institute for Metal Physics, N.A.S. of Ukraine, 2026
© Publisher Publishing House 'Akademperiodyka' of the N.A.S. of Ukraine, 2026

Science	the NZ30K Magnesium Alloy in Ringer–Locke Solution *V. L. GRESHTA, O. E. NARIVSKYI, and A. V. DZHUS*	985
Metallic Surfaces and Films	Fabrication and Characterization of CuO/Cu_2O Thin-Film Heterostructures on Si/ZnO Substrates *via* Magnetron Sputtering for Photovoltaic Applications *I. O. KOSIMOV, Sh. T. KHOZHIEV, K. T. DOVRANOV, M. A. DAVLATOV, F. F. ARZIKULOV, and U. Kh. KHOLIQOV*	999

Scientific Editors of Issue—*O. S. Gatsenko, V. A. Tatarenko*
Executive Managing Editor—*O. S. Gatsenko*
Editors—*L. I. Makarenko, M. V. Manilo, I. V. Zagorulko*
The artwork for direct reproduction is made by computer group of EPD of the G. V. Kurdyumov Institute for Metal Physics, N.A.S. of Ukraine

Editorial Office Address:
G. V. Kurdyumov Institute for Metal Physics, N.A.S. of Ukraine, EPD—'MNT',
36 Academician Vernadsky Boulevard, UA-03142 Kyiv, Ukraine
Telephone: +380 44 4249042. Fax: +380 44 4242561. E-mail: mfint@imp.kiev.ua
Media Identifier R30-03171

Approved for publication by the Academic Council of the G. V. Kurdyumov Institute for Metal Physics of the National Academy of Sciences of Ukraine
Published in English or Ukrainian languages according to resolution of Editorial Board of the journal

Printed by Publishing House 'Akademperiodyka', of the NAS of Ukraine
4 Tereshchenkivs'ka Str., UA-01024 Kyiv, Ukraine
Registration Certificate of Publishing Subject: ДК № 544 on 27.07.2001

Journal website: http://mfint.imp.kiev.ua
Journal DOI: https://doi.org/10.15407/mfint

Issue DOI: https://doi.org/10.15407/mfint.48.09

НАЦІОНАЛЬНА АКАДЕМІЯ НАУК УКРАЇНИ ● ІНСТИТУТ МЕТАЛОФІЗИКИ ім. Г. В. Курдюмова

МЕТАЛОФІЗИКА ТА НОВІТНІ ТЕХНОЛОГІЇ

ЩОМІСЯЧНИЙ НАУКОВИЙ ЖУРНАЛ
ЗАСНОВАНИЙ У ВЕРЕСНІ 1979 р.

Том 48, № 9; вересень, 2026

ЗМІСТ

Редакційні оголошення	Інформація для закордонних передплатників	V
	Інформація для авторів	VII
Аморфний і рідкий стани	Голлів ефект, питомий електричний опір і параметри спін-орбітальної взаємодії в аморфних стопах системи Fe–Cr–B *О. К. КУВАНДІКОВ, І. СУБХАНКУЛОВ, Н. С. ХАМРАЄВ, Р. М. РАЖАБОВ, Ш. А. ХОМІТОВ, О. З. ТУРГУНОВ*	919
Дефекти кристалічної ґратниці	Довжина критичного дислокаційного сеґмента під дією теплових флюктуацій *М. І. ЛУГОВИЙ, Д. Г. ВЕРБИЛО, М. П. БРОДНІКОВСЬКИЙ, Т. І. ВЕРБИЦЬКА, Д. С. ЛЕОНОВ, М. Ю. БАРАБАШ*	931
Фізика міцности та пластичности	Про вплив залишкових напружень на міцність оксидованих платівок за умов термомеханічного навантаження *І. П. ШАЦЬКИЙ, В. М. ПЕТРАЩУК, Л. Я. РОП'ЯК, О. О. ЛАЗАРЄВА*	949
Нові металеві матеріяли та синтетичні метали	Синтеза та характеризація композиту Ti_3SiC_2–TiC–$TiSi_2$ для високотемпературних застосувань *І. М. КІР'ЯН, А. М. ЛАХНІК, М. А. СКОРИК, С. О. КОТРЕЧКО, О. В. ЗАЦАРНА, Т. О. МОНАСТИРСЬКА, І. В. ГУРІН, О. Д. РУДЬ*	963
	Механізм утворення WC безпосередньо в матеріялі (*in situ*) під час механічного леґування середньоентропійного стопу $W_{1,5}$FeCoNi *С. Ю. ТЕСЛЯ, О. І. ЮРКОВА, Д. С. ЛЕОНОВ, П. І. ЛОБОДА*	973
Медичне металознавство	Характерні особливості селективного розчинення маґнійового стопу NZ30K у розчині Рінґера–Локка	

© G. V. Kurdyumov Institute for Metal Physics, N.A.S. of Ukraine, 2026
© Publisher Publishing House 'Akademperiodyka' of the N.A.S. of Ukraine, 2026

	В. Л. ГРЕШТА, О. Є. НАРІВСЬКИЙ, А. В. ДЖУС	985
Металічні поверхні та плівки	Виготовлення та дослідження характеристик тонкоплівкових гетероструктур CuO/Cu_2O на підкладинках Si/ZnO методом магнетронного розпорошення задля фотоелектричних застосувань *І. О. КОСІМОВ, Ш. Т. ХОЖІЄВ, К. Т. ДОВРАНОВ, М. А. ДАВЛАТОВ, Ф. Ф. АРЗІКУЛОВ, У. Х. ХОЛІКОВ*	999

Наукові редактори випуску: *О. С. Гаценко, В. А. Татаренко*
Відповідальний секретар редакційної колегії *О. С. Гаценко*
Редактор-коректор *О. С. Гаценко*
Технічні редактори: *І. В. Загорулько, Л. І. Макаренко, М. В. Маніло*
Художні редактори: *І. В. Загорулько, Л. І. Макаренко, М. В. Маніло*
Оригінал-макет для прямого репродукування виготовлено комп'ютерною групою РВВ Інституту металофізики ім. Г. В. Курдюмова НАН України

Адреса редакції:
Інститут металофізики ім. Г. В. Курдюмова НАН України, РВВ—Редакція «МНТ»
бульв. Акад. Вернадського, 36; 03142 Київ, Україна
Тел.: +380 44 4249042; факс: +380 44 4242561
Ел. пошта: mfint@imp.kiev.ua
Ідентифікатор медіа R30-03171

Затверджено до друку вченою радою Інституту металофізики ім. Г. В. Курдюмова НАН України
Друкується за постановою редакційної колегії журналу англійською або українською мовами

Підписано до друку 24.09.2026 р. Формат 70×100/16.
Ум. друк. арк. 8,13. Обл.-вид. арк. 7,48.
Тираж 55 пр. Зам. № 0000 від 30.09.2026 р.

Віддруковано ВД «Академперіодика» НАН України
вул. Терещенківська, 4; 01024 Київ, Україна
Свідоцтво суб'єкта видавничої справи ДК № 544 від 27.07.2001 р.

Сайт журналу: http://mfint.imp.kiev.ua
DOI (журналу): https://doi.org/10.15407/mfint
DOI (випуску): https://doi.org/10.15407/mfint.48.09

INFORMATION (GUIDELINES) FOR CONTRIBUTORS

Submission of Manuscripts: Manuscripts should be sent by e-mail (mfint@imp.kiev.ua). Additionally, they can be sent by regular mail to Executive Managing Editor, Editorial Office, G. V. Kurdyumov Institute for Metal Physics, N.A.S. of Ukraine, 36 Academician Vernadsky Boulevard, UA-03142 Kyiv, Ukraine. Manuscripts may also be submitted to a member of the Editorial Advisory Board or to the appropriate Regional Editor who is familiar with the research presented.
Submission of a paper to '*Metallophysics and Advanced Technologies*' (transliteration: '*Metallofizika i Noveishie Tekhnologii*', *i.e.*, '*MfNT*') will be taken to imply that it represents original work not previously published, that it is not being considered for publication elsewhere, and that, if accepted for publication, it will not be republished without the consent of the Editors and Publisher. It is a condition of acceptance by the Editor of a manuscript for publication that the Publishers acquire automatically the copyright in the manuscript throughout the world. Journal '*MfNT*' supports the generally accepted principles described in documents on publication ethics and unacceptable practices, which are presented on the journal website.
Scope of the Journal: *Electronic Structure and Properties, Crystal-Lattice Defects, Phase Transformations, Physics of Strength and Plasticity, Metallic Surfaces and Films, Structure and Properties of Nanoscale and Mesoscopic Materials, Amorphous and Liquid States, Interactions of Radiation and Particles with Condensed Matter, Materials in Extremal Conditions, Reactor and Aerospace Metals Science, Medical Metals Science, New Metallic Materials and Synthetic Metals, Metal-Containing Smart Materials, Physical and Technical Basis of Experiment and Diagnostics, Articles under Discussion*.
Language: The language of publication may be English (preferably) or Ukrainian.
Abstract: Each paper requires an abstract of 200–250 words summarizing the significant coverage and findings (the use of mathematical symbols and expressions in abstract is not recommended).
Keywords and PACS numbers: 5–7 keywords and PACS numbers reflecting the content of the contribution should be supplied (see 'Physics and Astronomy Classification Scheme 2010').
Manuscript Preparation: Papers should be formatted according to the template, which can be downloaded from the Journal's website. The length of **research papers** should not in general exceed 5000 words and 10 figures; **review articles** should not exceed 10000 words and 30 figures, including tables and diagrams. Authors are urged to arrange the subject matter clearly under headings such as: 1. Introduction, 2. Experimental/Theoretical Details, 3. Results, 4. Discussion, 5. Conclusion, References. Subsections should be identified with section and subsection numbers (such as 6.1. Second-Value Subheading).
References and Notes: Notes are indicated in the text by consecutive superior Arabic numbers (without parentheses). References should be numbered consecutively (in square brackets) throughout the text. The full list should be collected and typed at the end of the paper in numerical order. Listed references should be completed in all details including **DOI** (if available) but excluding article titles in journals. **All authors'** initials should precede their names. Examples of references preparation:

1. S. O. Firstov and T. G. Rogul, *Metallofiz. Noveishie Tekhnol.*, **44**, No. 1: 127 (2022) (in Ukrainian). https://doi.org/10.15407/mfint.44.01.0127
2. V. B. Tarelnyk, O. P. Gaponova, and Ye. V. Konoplianchenko, *Prog. Phys. Met.*, **23**, No. 1: 27 (2022). https://doi.org/10.15407/ufm.23.01.027
3. A. Meisel, G. Leonhardt, and R. Szargan, *Röntgenspektren und Chemische Bindung* [X-Ray Spectra and Chemical Bond] (Leipzig: Akademische Verlagsgesellschaft Geest & Portig K.-G.: 1977) (in German).
4. J. M. Ziman, *Printsipy Teorii Tverdogo Tela* [Principles of the Theory of Solids] (Moscow: Mir: 1974) (Russian translation).
5. M. A. Stucke, D. M. Dimiduk, and D. M. Hazzledine, *High Temperature Ordered Intermetallic Alloys. V* (Eds. I. Baker and R. Darolia) (Pittsburgh, PA, USA: MRS: 1993), p. 471.
6. *Handbook of Mathematical Functions with Formulas, Graphs and Mathematical Tables* (Eds. M. Abramowitz and I. A. Stegun), Nat'l Bureau of Standards. Appl. Math. Ser. Vol. **55** (Washington, D.C.: U.S. Govt. Printing Office: 1964).
7. B. B. Karpovych and O. B. Borovkoff, *Proc. of Symp. 'Micromaterials Engineering' (Dec. 25–31, 1999)* (Kyiv: RVV IMF: 2000), vol. **2**, p. 113 (in Russian).
8. A. E. Krug, *Abstr. Int. Conf. Phys. Phenomena (Dec. 25–31, 1991, Alushta)* (Kharkiv: 1991), p. 12.
9. T. M. Radchenko, *Vplyv Uporyadkuvannya Defektnoyi Struktury на Transportni Vlastyvosti Zmishanykh Krystaliv* [Influence of Ordering of the Defect Structure on Transport Properties of the Mixed Crystals] (Thesis of Disser. for the Degree of Dr. Phys.-Math. Sci.) (Kyiv: G. V. Kurdyumov Institute for Metal Physics, N.A.S.U.: 2015) (in Ukrainian). https://doi.org/10.13140/RG.2.2.35430.22089

10. E. M. Gololobov, V. B. Shipilo, N. I. Sedrenok, and A. I. Dudyak, *Sposob Polucheniya Karbonitridov Metallov* [Production Method of Metal Carbonitrides], Authors' Certificate 722341 SSSR (Publ. November 21, 1979) (in Russian).
11. V. G. Trubachev, K. V. Chuistov, V. N. Gorshkov, and A. E. Perekos, *Sposob Polucheniya Metallicheskikh Poroshkov* [The Technology of Metallic Powder Production]: Patent 1639892 SU. MKI, B22 F9/02, 9/14 (Otkrytiya i Izobreteniya, **34**, No. 13: 11) (1991) (in Russian).
12. Yu. M. Koval' and V. V. Nemoshkalenko, *O Prirode Martensitnykh Prevrashcheniy* [On the Nature of Martensitic Transformations] (Kyiv: 1998) (Prepr./N.A.S. of Ukraine. Inst. for Metal Physics. No. 1, 1998) (in Russian).

Journal title abbreviations should conform to generally accepted styles:
https://www.cas.org/support/documentation/references/corejournals;
https://cdn.journals.aps.org/files/rmpguapb.pdf;
https://images.webofknowledge.com/WOK46P9/help/WOS/A_abrvjt.html;
https://mathscinet.ams.org/msnhtml/serials.pdf.

Equations and Formulae: Formulas in the text should be inserted by **MathType**, fully compatible with MS Office. Vectors should be typed in bold without arrows above. Note that complicated formulae, mathematical expressions or (de)notations are not recommended in the title, abstract, and keywords.

Tables: Number tables consecutively with Arabic numerals and give a clear descriptive caption at the top.

Figures: All figures should be numbered with consecutive Arabic numbers, have descriptive captions and be mentioned in the text. Keep figures separate at the end of the text and clearly label each figure with author's name and figure number. The labels at axis should contain the designation (or notation) of quantities and their units.

Preparation: Figures submitted must be of a high enough standard for reproduction with 300–600 dpi resolution (including half-tone illustrations). Redrawing or retouching of unusable figures will be charged to the authors.

Colour Plates: Whenever, the use of colour is an integral part of the research, or where the work is generated in colour, the Journal will publish (in paper version) the colour illustrations with charge to the author. Reprints in colour will carry a surcharge. Please write to the Publisher for details.

Submission of Electronic Text: Authors should submit the electronic version of their paper by e-mail to the Editorial Office. The text file should be saved in the native formats of the MS Word with a name consisting the name of the first author, for example, Hotovchenko.docx. The electronic form of figures (in TIF, EPS, JPG, PNG formats preferably and with name consisting the name of the first author also, for example, Hotovchenko_fig2a.jpg) should be planned so that they reduce to 12.7 cm column width (or less), and keep them separated from the text file. It is desirable to submit additionally all the **figures** within the format of the program, in which they were created.

Proofs: Contributors will receive page proofs for correction by e-mail as a PDF document. These must be returned to Kyiv office (mfint@imp.kiev.ua with subject beginning by word 'mfint') within 5 days of receipt.

Page Charges: There are no page charges to individuals or institutions.

Reprints: Authors can freely download a PDF version of their published article from journal website: https://mfint.imp.kiev.ua. The printed issues may be ordered by completing the appropriate form sent with proofs and prepaid by authors under the terms as for subscription.

Further Information: All questions arising during the **peer review** or after acceptance of manuscripts, especially those relating to reprints, should be directed to G. V. Kurdyumov Institute for Metal Physics, N.A.S. of Ukraine, Executive Managing Editor, Editorial Office, 36 Academician Vernadsky Blvd., UA-03142 Kyiv, Ukraine;
Fax: +380 44 4242561, e-mail: mfint@imp.kiev.ua (with subject beginning by word 'mfint').

We ask the authors to apply with their manuscript Copyright Transfer Agreement form.

Copyright Transfer Agreement

We, the undersigned authors of the manuscript '_____', transfer to the Founders, Publisher, and Editorial Board of the Journal 'Metallophysics and Advanced Technologies' (according to agreements between them) the right to publish this manuscript in original language or in translation to the other languages. We confirm that publication of this manuscript **will not** infringe a copyright of other persons or organizations and publication ethics.

Author(s):_____
(Last Name, First Name, Affiliation)

Correspondence Address:_____

Phone and e-mail: _____

_____ _____
(Signature) *(Date)*

ІНФОРМАЦІЯ (ПРАВИЛА) ДЛЯ АВТОРІВ

Науковий журнал «Металофізика та новітні технології» (МфНТ) щомісяця публікує статті, які раніше ще не публікувалися та не перебувають на розгляді для опублікування в інших виданнях. Статті мають містити результати експериментальних і теоретичних досліджень в області фізики та технологій металів, стопів і сполук з металічними властивостями; рецензії на монографії; інформацію про конференції, семінари; відомості з історії металофізики; рекламу нових технологій, матеріялів, приладів. Журнал дотримується загальноприйнятих принципів, зазначених на його сайті в документах з публікаційної етики та щодо неприйнятних практик.

Тематика журналу: *Електронні структура та властивості, Дефекти кристалічної ґратниці, Фазові перетворення, Фізика міцности та пластичности, Металічні поверхні та плівки, Будова та властивості наномасштабних і мезоскопічних матеріялів, Аморфний і рідкий стани, Взаємодії випромінення та частинок із конденсованою речовиною, Матеріяли в екстремальних умовах, Реакторне й авіакосмічне металознавство, Медичне металознавство, Нові металеві матеріяли та синтетичні метали, Металовмісні смарт-матеріяли, Фізико-технічні основи експерименту та діягностики, Дискусійні повідомлення*.

Статті публікуються однією з двох мов: англійською (віддається перевага) або українською.

Статті, в оформленні яких не дотримано наступних правил для опублікування в МфНТ, повертаються авторам без розгляду по суті. (Датою надходження вважається день повторного надання статті після дотримання зазначених нижче правил.)

1. Стаття має бути підписаною всіма авторами (із зазначенням їхніх адрес електронної пошти); слід вказати прізвище, ім'я та по батькові автора, з яким редакція буде вести листування, його поштову адресу, номери телефону та факсу й адресу електронної пошти.

2. Виклад матеріялу має бути чітким, **структурованим** (розділами, наприклад, «1. Вступ», «2. Експериментальна/Теоретична методика», «3. Результати та їх обговорення», «4. Висновки», «Цитована література»), стислим, без довгих преамбул, відхилень і повторів, а також без дублювання в тексті даних таблиць, рисунків і підписів до них. Анотація та розділ «Висновки» мають не дублювати один одного. Числові дані слід наводити в загальноприйнятих одиницях.

3. Об'єм оригінальної (неоглядової) статті має бути не більше 5000 слів (з урахуванням основного тексту, таблиць, підписів до рисунків, списку використаних джерел) і 10 рисунків. **Об'єм оглядової статті** — до 10000 слів та 30 рисунків.

4. За потреби до редакції може надаватися друкований (А4, подвійний інтервал) примірник рукопису з ілюстраціями.

5. До редакції обов'язково надається (по **e-mail**) файл статті, набраний у текстовому редакторі Microsoft Word, з назвою, що складається з прізвища першого автора (латиницею), наприклад, Hotovchenko.docx.

6. Електронна версія рукопису та його друкований варіянт (в разі його надання) мають бути ідентичними. Вони мають оформлюватися за шаблоном, який можна завантажити з сайту журналу, і містити 5–7 **індексів PACS** в редакції 'Physics and Astronomy Classification Scheme 2010'. Тексти статей мають також містити **назву статті**, **список авторів**, **повні назви** та **поштові адреси установ**, в яких вони працюють, **анотацію статті** (200–250 слів), **5–7 ключових слів** двома мовами (**англійською** та **українською**), а заголовки таблиць і підписи до рисунків мають подаватися **як мовою рукопису, так і англійською мовою**; англомовна анотація може бути представленою в більш розгорнутому варіянті (до 500 слів). Назва статті, її анотація та ключові слова мають не містити складні формули, математичні вирази чи позначення.

7. Електронні версії рисунків мають бути представленими у вигляді окремих файлів (у форматах TIF, EPS, JPG, PNG з розріжненням у 300–600 dpi) з назвами, що складаються з прізвища першого автора (латиницею) та номера рисунка, наприклад, Hotovchenko_fig2a.jpg. Додатково рисунки надаються у форматі програми, в якій вони створювалися.

8. Написи на рисунках (особливо на півтонових) слід по можливості замінити літерними позначеннями (набраними на контрастному фоні), а криві позначити цифрами або різними типами ліній/маркерів, які мають бути роз'ясненими в підписах до рисунків або в тексті. На графіках усі лінії/маркери мають бути достатньої товщини/розміру для якісного відтворення їх у зменшеному в 2–3 рази вигляді (рекомендована початкова ширина рисунка — 12,7 см). Світлини мають бути чіткими та контрастними, а написи та позначення мають не закривати істотні деталі (для чого можна використовувати стрілки). Замість зазначення в підтекстовці збільшення під час зйомки бажано проставити масштаб (на контрастному фоні) на одній з ідентичних світлин. На графіках підписи до осей, **виконані мовою статті**, мають містити позначення (або найменування) величин, що відкладаються вздовж осей, і відділені комою їхні одиниці вимірювання.

9. Формули в текст треба вставляти за допомогою редактора формул **MathType**, сумісного з MS Office. **Вектори** слід набирати напівтовстим шрифтом без стрілок зверху.

10. Рисунки, таблиці, формули, а також підрядкові **примітки (виноски)** мають нумеруватися поспіль по всій статті.

11. Посилання на літературні джерела слід давати у вигляді порядкового номера, надрукованого в рядок у квадратних дужках. Список цитованої літератури складається почергово за першою згадкою джерела. Приклади оформлення посилань наведено нижче (просимо звернути увагу на порядок розташування ініціалів і прізвищ авторів, бібліографічних відомостей і на розділові знаки, а також на необхідність зазначення **всіх** співавторів цитованої роботи та її ідентифікатора **DOI**, якщо він є):

1. S. O. Firstov and T. G. Rogul, *Metallofiz. Noveishie Tekhnol.*, **44**, No. 1: 127 (2022) (in Ukrainian). https://doi.org/10.15407/mfint.44.01.0127
2. V. B. Tarelnyk, O. P. Gaponova, and Ye. V. Konoplianchenko, *Prog. Phys. Met.*, **23**, No. 1: 27 (2022). https://doi.org/10.15407/ufm.23.01.027
3. A. Meisel, G. Leonhardt, and R. Szargan, *Röntgenspektren und Chemische Bindung* [X-Ray Spectra and Chemical Bond] (Leipzig: Akademische Verlagsgesellschaft Geest & Portig K.-G.: 1977) (in German).
4. J. M. Ziman, *Printsipy Teorii Tverdogo Tela* [Principles of the Theory of Solids] (Moscow: Mir: 1974) (Russian translation).
5. M. A. Stucke, D. M. Dimiduk, and D. M. Hazzledine, *High Temperature Ordered Intermetallic Alloys. V* (Eds. I. Baker and R. Darolia) (Pittsburgh, PA, USA: MRS: 1993), p. 471.
6. *Handbook of Mathematical Functions with Formulas, Graphs and Mathematical Tables* (Eds. M. Abramowitz and I. A. Stegun), Nat'l Bureau of Standards. Appl. Math. Ser. Vol. **55** (Washington, D.C.: U.S. Govt. Printing Office: 1964).
7. B. B. Karpovych and O. B. Borovkoff, *Proc. of Symp. 'Micromaterials Engineering' (Dec. 25–31, 1999)* (Kyiv: RVV IMF: 2000), vol. **2**, p. 113 (in Russian).
8. A. Eh. Krug, *Abstr. Int. Conf. Phys. Phenomena (Dec. 25–31, 1991, Alushta)* (Kharkiv: 1991), p. 12.
9. T. M. Radchenko, *Vplyv Uporyadkuvannya Defektnoyi Struktury na Transportni Vlastyvosti Zmishanykh Krystaliv* [Influence of Ordering of the Defect Structure on Transport Properties of the Mixed Crystals] (Thesis of Disser. for the Degree of Dr. Phys.-Math. Sci.) (Kyiv: G. V. Kurdyumov Institute for Metal Physics, N.A.S.U.: 2015) (in Ukrainian). https://doi.org/10.13140/RG.2.2.35430.22089
10. E. M. Gololobov, V. B. Shipilo, N. I. Sedrenok, and A. I. Dudyak, *Sposob Polucheniya Karbonitridov Metallov* [Production Method of Metal Carbonitrides], Authors' Certificate 722341 SSSR (Publ. November 21, 1979) (in Russian).
11. V. G. Trubachev, K. V. Chuistov, V. N. Gorshkov, and A. E. Perekos, *Sposob Polucheniya Metallicheskikh Poroshkov* [The Technology of Metallic Powder Production]: Patent 1639892 SU. MKI, B22 F9/02, 9/14 (Otkrytiya i Izobreteniya, **34**, No. 13: 11) (1991) (in Russian).
12. Yu. M. Koval' and V. V. Nemoshkalenko, *O Prirode Martensitnykh Prevrashcheniy* [On the Nature of Martensitic Transformations] (Kyiv: 1998) (Prepr./N.A.S. of Ukraine. Inst. for Metal Physics. No. 1, 1998) (in Russian).

Слід використовувати загальноприйняті скорочення назв журналів:
https://www.cas.org/support/documentation/references/corejournals;
https://cdn.journals.aps.org/files/rmpguapb.pdf;
https://images.webofknowledge.com/WOK46P9/help/WOS/A_abrvjt.html;
https://mathscinet.ams.org/msnhtml/serials.pdf.

Необхідною вимогою є також надання авторами додаткового списку цитованої літератури (**References**) в **латинській транслітерації** (система **BGN/PCGN**; рекомендовані транслітератори: http://www.slovnyk.ua/services/translit.php; http://ru.translit.net/?account=bgn).

Після транслітерованих назв книг, дисертацій, патентів та ін. слід у квадратних дужках наводити їхній англомовний переклад (див. приклади вище). При транслітерації статей з МфНТ слід використовувати написання П.І.Б. авторів, наведені **лише** в англомовному змісті відповідного випуску, і **офіційну** транслітеровану назву журналу (див. також першу сторінку кожної статті та сайт).

12. Коректура авторам надсилається електронною поштою у вигляді pdf-файлу після завершення етапу **рецензування**. На перевірку коректури авторам відводяться 5 робочих днів. Після закінчення зазначеного терміну стаття автоматично направляється до друку. Виправлення слід відмітити та прокоментувати в самому pdf-файлі або оформити у вигляді переліку виправлень (підписаного уповноваженим представником колективу авторів) і переслати електронною поштою на адресу редакції.

Електронний варіянт статті надсилається на e-mail: mfint@imp.kiev.ua (з темою, що починається словом 'mfint'). Друкована версія рукопису (якщо у ній є потреба) надсилається за адресою: **Інститут металофізики ім. Г. В. Курдюмова НАН України, редакція МфНТ; бульвар Акад. Вернадського, 36; 03142 Київ, Україна** або відповідному реґіональному редактору (див. сайт).

Автори можуть вільно завантажити pdf-файли опублікованих статей з сайту журналу (https://mfint.imp.kiev.ua), а також замовити друковані примірники випуску журналу зі своєю статтею, надіславши до редакції журналу **разом з коректурою відповідну заявку та квитанцію про оплату** друку необхідної кількості примірників випуску на умовах, аналогічних передплатним.

Відповідно до угод між редакцією МфНТ, засновниками та видавцем журналу, редакція вважає, що автори, надсилаючи їй рукопис статті, передають засновникам, видавцю та редколеґії право опублікувати цей рукопис мовою ориґіналу та в перекладі іншими мовами, і просить авторів відразу прикладати до рукопису «Угоду про передачу авторського права».

Угода про передачу авторського права

Ми, що нижче підписалися, автори рукопису «_____», передаємо засновникам, видавцю та редколеґії журналу «Металофізика та новітні технології» (згідно з угодами між ними) право опублікувати цей рукопис мовою ориґіналу та в перекладі іншими мовами. Ми підтверджуємо, що ця публікація **не** порушує авторського права інших осіб або організацій і принципів наукової етики. При цьому за авторами зберігаються всі інші права як власників цього рукопису.

Підписи авторів: _____ (П.І.Б., дата, адреса, тел., e-mail)

Metallophysics and Advanced Technologies
Металофіз. новітні технол.
Metallofiz. Noveishie Tekhnol.
2026, vol. 48, No. 9, pp. 919–929
https://doi.org/10.15407/mfint.48.09.0919
Reprints available directly from the publisher

© 2026 G. V. Kurdyumov Institute for Metal Physics,
National Academy of Sciences of Ukraine
Published by license under
the G. V. Kurdyumov Institute for Metal Physics–
N.A.S. of Ukraine Publishers imprint.
Printed in Ukraine.

PACS numbers: 71.70.Ej, 72.15.Cz, 72.15.Gd, 73.50.Jt, 75.47.Np, 75.50.Kj, 85.75.Nn

The Hall Effect, Electrical Resistivity and Spin–Orbit Interaction Parameters in Amorphous Alloys of the Fe–Cr–B System

O. K. Kuvandikov, I. Subkhankulov, N. S. Hamraev, R. M. Razhabov, Sh. A. Khomitov, and O. Z. Turgunov*

Samarkand State University named after Sharof Rashidov,
15 University Blvd.,
UZ-140104 Samarkand, Uzbekistan
**Physical-Technical Institute*
of Uzbekistan Academy of Sciences named after S. A. Azimov,
2B Chingiz Aytmatov Str.,
UZ-100084 Tashkent, Uzbekistan

In this study, the temperature dependences of the electrical resistivity (ρ) and the Hall coefficient (R_H) of amorphous alloys of the $Fe_{85-x}Cr_xB_{15}$ ($x = 8$, 10, 12, 15) system based on 3*d* elements are experimentally investigated. The alloys are obtained from the liquid state by the melt-spinning (ultrarapid quenching) technique. Measurements are carried out in the temperature range 300–773 K using the Van der Pauw method. As established, the ferromagnetic–paramagnetic phase-transition temperature of the samples is fully correlated with the temperature dependences of both the Hall coefficient and the electrical resistivity, whereas the amorphous–crystalline phase-transition temperature varies depending on the iron content in the samples. The results of the mutual and temperature dependences of the electrical and galvanomagnetic properties of the samples are analysed. As a result of a comprehensive experimental study of the electrical and galvanomagnetic properties of amorphous Fe–Cr–B alloys, it becomes possible to estimate the

Corresponding author: Sherzod Asatillo Xomitov
E-mail: sherxomitov@gmail.com

Citation: O. K. Kuvandikov, I. Subkhankulov, N. S. Hamraev, R. M. Razhabov, Sh. A. Khomitov, and O. Z. Turgunov, The Hall Effect, Electrical Resistivity and Spin–Orbit Interaction Parameters in Amorphous Alloys of the Fe–Cr–B System, *Metallofiz. Noveishie Tekhnol.*, **48**, No. 9: 919–929 (2026). DOI: 10.15407/mfint.48.09.0919

© Publisher PH 'Akademperiodyka' of the NAS of Ukraine, 2026. This is an open access article under the CC BY-ND license (https://creativecommons.org/licenses/by-nd/4.0)

effective spin–orbit interaction parameter for these samples.
Key words: amorphous alloy, Curie temperature, crystallization temperature, Hall coefficient, electrical resistivity, effective spin–orbit interaction parameter.

У цьому дослідженні експериментально вивчено температурні залежності питомого електричного опору (ρ) та Голлового коефіцієнта (R_H) аморфних стопів системи $Fe_{85-x}Cr_xB_{15}$ ($x = 8, 10, 12, 15$) на основі 3*d*-елементів. Стопи було одержано з рідкого стану методом спінінґування (надшвидкого гартування) розтопу. Міряння проводилися в діяпазоні температур 300–773 K методою Ван дер Пау. Було встановлено, що температура фазового переходу феромагнетик–парамагнетик зразків повністю корелює з температурними залежностями як Голлового коефіцієнта, так і питомого електричного опору, тоді як температура фазового переходу аморф–кристал змінюється залежно від вмісту Феруму у зразках. Було проаналізовано результати взаємних і температурних залежностей електричних і ґальваномагнетних властивостей зразків. В результаті комплексного експериментального дослідження електричних і ґальваномагнетних властивостей аморфних стопів Fe–Cr–B стало можливим оцінити ефективний параметер спін-орбітальної взаємодії для цих зразків.

Ключові слова: аморфний стоп, температура Кюрі, температура кристалізації, Голлів коефіцієнт, питомий електричний опір, ефективний параметер спін-орбітальної взаємодії.

(Received 26 January, 2026; in final version, 12 May, 2026)

1. INTRODUCTION

At present, the research on the physical properties and internal structure of amorphous ferromagnetic alloys based on 3*d* transition metals remains an important scientific problem. The influence of temperature on the physical properties of metals and their alloys provides valuable information about their structural and volumetric changes, as well as about the melting process. This, in turn, has significant practical importance in mechanical engineering, in the heat treatment of metals, and in engineering calculations [1, 2].

Alloys based on transition metals and their mixtures with metalloid additions are promising subjects of modern materials science in terms of their applications. This is because amorphous alloys exhibit low coercive force, high magnetic absorption, and high electrical resistivity. In addition, when compared with crystalline materials, amorphous alloys demonstrate superior mechanical strength as well as improved resistance to corrosion [3, 4]. It should be emphasized that the aforementioned properties of iron-group-based alloys are mainly realized when these materials are in the amorphous or nanocrystalline state. These materials are promising for electronic applications as soft magnetic

materials, including cores for miniaturized transformers, field sensors, generators, and various energy conversion systems [5, 6].

In addition, amorphous alloys are used in magnetic recording and in electronic engineering as data storage devices [7, 8]. They also play an important role in industrial production [9, 10], in the aerospace sector [11], in medicine [12, 13], and in the military field, particularly, in defence equipment [14].

The study of the Hall coefficient as a function of temperature in amorphous ferromagnets makes it possible to determine the sign and concentration of charge carriers, as well as to establish the relationship between the anomalous Hall coefficient R_S, the electrical resistivity ρ, and the saturation magnetization I_S [15, 16]. This provides important information about the nature of galvanomagnetic phenomena in amorphous ferromagnetic alloys depending on their composition and structure, as well as allows the identification of regularities in the variation of key parameters related to electrical transport and the transition to the crystalline state [17].

2. EXPERIMENTAL DETAILS

The aim of this study is the experimental investigation of the temperature dependences of the Hall coefficient R_H and the electrical resistivity ρ in amorphous ferromagnetic alloys based on iron-group metals, the determination of the Curie temperature and the crystallization temperature, and the identification of the relationships between these parameters. Furthermore, based on the results of the temperature dependences of ρ and R_H, the study aims to estimate the effective spin–orbit interaction parameter λ_{SO} in ferromagnetic amorphous alloys.

The electrical resistivity ρ and Hall coefficient R_H of the samples were experimentally measured using the Van der Pauw method device (High Temp Hall effect Measurement System (HMS7000 + AHT55T5) –RT $\cong$ 773 K) [18]. Experiments using this device were conducted in the temperature range of 300–773 K.

The measurements were carried out on samples of amorphous ribbons 20 mm wide, 20 μm thick, and several meters long, obtained by quenching from the melt on a rapidly rotating disk [19, 20]. From these samples, specimens measuring 10×10 mm^2 were cut.

The Van der Pauw method is a common method for measuring the resistivity and Hall coefficient of a sample. It requires that the sample be isotropic, homogeneous, flat, of uniform thickness, and free of defects.

The convenience of this method is that four point (or line) contacts A, B, C, D are taken on the side surface of a flat sample and, when measuring the Hall voltage, a current is passed through contacts A and C, and the Hall potential difference between contacts B and D is also

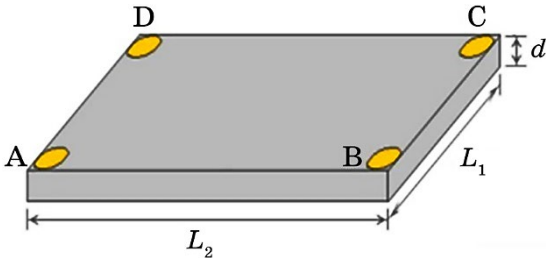


Fig. 1. General view of the sample.

measured. When calculating the resistance, a current is passed through contacts A and D. The voltage between contacts B and C is measured and the resistances are calculated [21, 22].

The specific electrical resistance is calculated knowing the resistances $R_{AB,CD}$ and $R_{BC,DA}$:

$$\rho = \frac{\pi d}{\ln 2} \frac{R_{AB,CD} + R_{BC,DA}}{2} f . \quad (1)$$

Here, d—sample thickness, $R_{AB,CD}$ and $R_{BC,DA}$ are the resistance values of the sample measured by the Van der Pauw method, f is the geometric correction factor, the value of which is calculated using the ratio $R_{AB,CD}/R_{BC,DA}$. The experiment requires that L_1 and L_2 be equal to each other ($L_1 = L_2$).

The theory of the Van der Pauw method is based on the theory of conformal reflection [23, 24]. The average Hall coefficient of the samples is calculated using the expression below:

$$R_H = \frac{R_{H(AC,BD)} + R_{H(BD,AC)}}{2} . \quad (2)$$

By comprehensively studying the electrical, magnetic, and galvanomagnetic properties, it is possible to evaluate the effective spin–orbit interaction parameter λ_{SO} [25, 26].

$$R_H = \frac{\rho_H}{B} = R_0 + \frac{2e^2}{\mu_0 \mu_B \hbar g} \rho^2 \lambda_{SO} \chi = R_0 + R_S \chi . \quad (3)$$

In this expression, the normal Hall coefficient, which is one of the components of the Hall effect, is significantly smaller than the anomalous Hall coefficient

$$R_S = \frac{2e^2}{\mu_0 \mu_B \hbar g} \rho^2 \lambda_{SO} \quad (4)$$

($R_0 << R_S$). Here, $e = 1.6 \cdot 10^{-19}$ C is the electron charge, $\mu_B = 0.927 \cdot 10^{-23}$

J/T is the Bohr magneton, $\mu_0 = 4\pi \cdot 10^{-7}$ H/m is the magnetic constant, $\hbar = 1.054 \cdot 10^{-34}$ J·s is the Planck constant, Lande coefficient $g \approx 2$ for transition metals, ρ—electrical resistivity, λ_{SO}—effective parameter of the spin–orbit interaction.

Using formula (4), the value of λ_{SO} is found:

$$\lambda_{SO} = \frac{R_S \mu_0 \mu_B \hbar g}{2e^2 \rho^2}. \quad (5)$$

3. RESULTS AND DISCUSSION

Recent scientific studies of amorphous alloys show that within the temperature range of 100–1000 K, the electrical resistivity ρ is higher in the amorphous state compared to the crystalline state, while the temperature coefficient of resistivity is lower in the amorphous state than in the crystalline form [27]. Similarly, in our studied samples, the absolute value of the electrical resistance in the amorphous state from room temperature to the phase transition temperature shows that increasing content of chromium in samples leads to the increasing of value of resistivity of them. In all studied samples, the electrical resistivity ρ decreases sharply during the transition from the amorphous to the crystalline state and increases with a subsequent increase in temperature. In the crystalline state, $\rho(T)$ decreases with decreasing temperature. After the phase transition, the temperature coefficient of resistance in the crystalline state in all samples is greater than that in the amorphous state. When the temperature reaches the Curie temperature T_C, a significant sharp decrease in the value of the Hall coefficient $R_H(T)$ was observed, which is associated with the transition of the sample from the ferromagnetic state to the paramagnetic state [28].

The temperature dependences of the Hall coefficient and the electrical resistivity of the investigated alloys of the $Fe_{85-x}Cr_xB_{15}$ system ($x = 8–15$) are shown in Figs. 2 and 3. In this study, the measurements were performed within the temperature range of 300–770 K.

Figure 2 indicates that the Hall coefficient decreases from room temperature to 400 K in the $Fe_{77}Cr_8B_{15}$ sample. For other samples, such a sharp decrease in the Hall coefficient is also observed at lower temperatures compared to the first sample with an iron concentration of 77%. It can be noted that with a decrease in the concentration of iron in the sample, the temperature of such a sharp decrease also decreases, and for the sample with the lowest concentration of iron, the decrease occurs below room temperature. This behaviour of the Hall coefficient can be associated with a phase transition of the ferromagnetism–paramagnetism type, *i.e.*, with the Curie temperature, and for the samples we studied, it is of 430, 380, 330, 295 K, respectively, as given in Table 1.

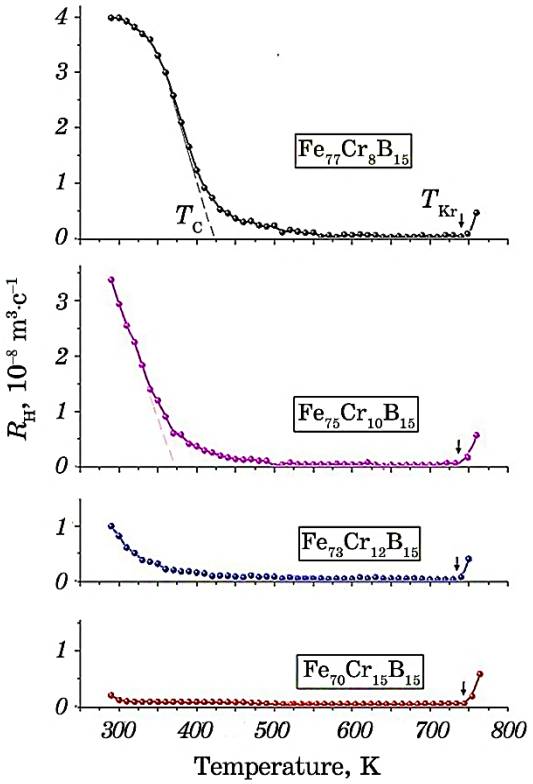


Fig. 2. Temperature dependence of the Hall coefficient of amorphous alloys of the Fe–Cr–B system.

For the studied alloys, a trend toward increasing R_H is observed in the temperature range of 720 K for the $Fe_{77}Cr_8B_{15}$ alloy and 750 K for the $Fe_{70}Cr_{15}B_{15}$ alloy. This experimental finding confirms that increasing Cr concentration and decreasing Fe concentration increase crystallization temperatures.

Based on the analysis of the obtained results, it can be concluded, that the iron concentration in the samples decreases and the metalloid concentration increases, the magnitude of the Hall coefficient and Curie temperature decreases, while the crystallization temperature increases.

The temperature dependence of the specific electrical resistance of amorphous alloys of the Fe–C–B system is shown in Fig. 3. It can be seen from this figure that for all samples the resistivity depends weakly on temperature. In almost all amorphous metal alloys based on iron-group elements, the specific electrical resistance ρ changes almost linearly from room temperature to the crystallization temperature, and the temperature coefficient of resistance TCR—$\partial\rho/\partial T$ takes the fol-

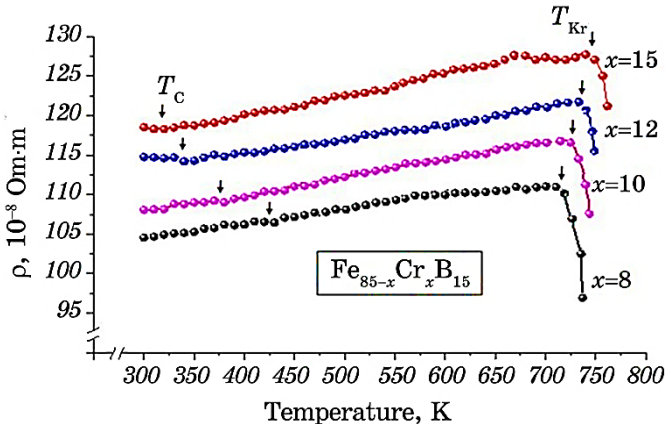


Fig. 3. Temperature dependence of the specific electrical resistance of the amorphous alloy of the Fe–Cr–B system.

lowing values: for the amorphous alloy $Fe_{70}Cr_{15}B_{15}$, $\partial\rho/\partial T = 2.62\cdot10^{-2}$ (μOm·cm)/K; for the alloy $Fe_{73}Cr_{12}B_{15}$, $\partial\rho/\partial T = 2.45\cdot10^{-2}$ (μOm·cm)/K; for the sample $Fe_{75}Cr_{10}B_{15}$, $\partial\rho/\partial T = 2.23\cdot10^{-2}$ (μOm·cm)/K; and for the sample $Fe_{77}Cr_8B_{15}$, $\partial\rho/\partial T = 1.89\cdot10^{-2}$ (μOm·cm)/K. The initial values of specific electrical resistance at room temperature for the samples $Fe_{70}Cr_{15}B_{15}$, $Fe_{73}Cr_{12}B_{15}$, $Fe_{75}Cr_{10}B_{15}$ and $Fe_{77}Cr_8B_{15}$ are as follow: $118.5\cdot10^{-8}$ Om·m, $114.8\cdot10^{-8}$ Om·m, $107\cdot10^{-8}$ Om·m and $104\cdot10^{-8}$ Om·m, respectively, that is, the absolute value of specific electrical resistance increases with the increase of chromium concentration.

Analysing the graphs of temperature dependence of specific electrical resistance $\rho(T)$ for the studied samples, we can come to the following conclusions.

The absolute value of resistivity increases with decreasing iron con-

TABLE 1. Hall coefficient and specific electrical resistance, Curie temperature and crystallization temperature for the studied amorphous alloys.

Parameter value depending on composition				
Amorphous alloys	Curie temperature T_C, K	Crystallization temperature T_K, K	Values of specific electrical resistance at room temperature $\rho_0\cdot10^{-8}$ [Om·m]	Hall coefficient values at room temperature $R_H\cdot10^{-8}$ [m³/C]
$Fe_{70}Cr_{15}B_{15}$	295	750	118.5	0.16
$Fe_{73}Cr_{12}B_{15}$	330	740	114.8	1
$Fe_{75}Cr_{10}B_{15}$	380	730	107	3.4
$Fe_{77}Cr_8B_{15}$	430	720	104	4

tent and increasing metalloid concentrations in samples, while the temperature coefficient of resistivity decreases.

Increasing metalloid concentrations, firstly, reduces the effective number of charge carriers and, secondly, increases the scattering potential, resulting in an increase in electrical resistivity ρ. At the same time, according to the Moodgi criterion, $\partial\rho/\partial T$ decreases with increasing electrical resistivity ρ [29, 30].

According to the literature [31, 32] that with increasing metalloid concentration, the electrical resistivity ρ increases, $\partial\rho/\partial T$ decreases, and there are cases in which the electrical resistivity does not vary with temperature, and such materials can serve as resistive components. It can be explained by the increase in the concentration of metalloid in the composition of the samples and the increase in the crystallization temperature of the samples, the increase in the stability of the amorphous state and the strengthening of the covalent bond between the alloy elements.

Based on the temperature dependences of the Hall coefficient and electrical resistivity, the Curie and crystallization temperatures for the investigated alloys were determined, as presented in Table 1.

The tables show that, with increasing chromium concentration, the Curie temperature T_C in the samples decreases and the crystallization onset temperature T_K increases. The observed behaviour is attributed to the antiferromagnetic properties of Cr [33].

Experimental findings demonstrate that lowering the iron concentration and increasing the metalloid content in the samples result in decreased Hall coefficient and Curie temperature, accompanied by an increase in crystallization temperature. The main analytical results are summarized in graphical form.

Figure 4 illustrates the dependence of the crystallization tempera-

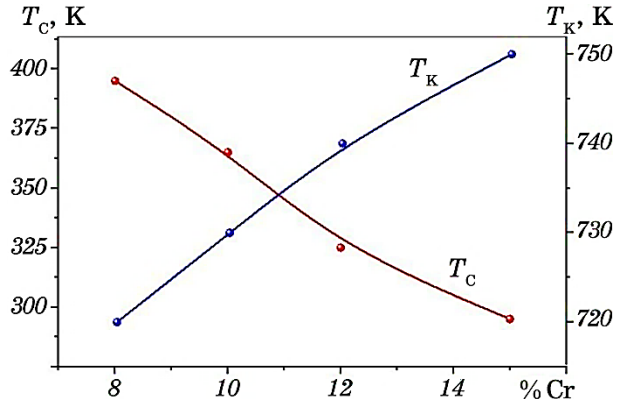


Fig. 4. Dependence of T_C and T_K for the amorphous alloys of Fe–Cr–B system on the concentration of Cr.

TABLE 2. λ_{SO} for the Fe–Cr–B-system amorphous alloys.

	$Fe_{77}Cr_8B_{15}$	$Fe_{75}Cr_{10}B_{15}$	$Fe_{73}Cr_{12}B_{15}$	$Fe_{70}Cr_{15}B_{15}$
T [K]	$\lambda_{SO}\cdot10^{-14}$ [J]	$\lambda_{SO}\cdot10^{-14}$ [J]	$\lambda_{SO}\cdot10^{-14}$ [J]	$\lambda_{SO}\cdot10^{-14}$ [J]
300	17.7	12.3	2.9	0.54
320	16.6	9	1.8	0.4
340	15.2	5.7	1.2	0.33
360	13	3.63	0.72	0.2
380	8.6	2	0.3	
400	5.1	1.1		
420	2.9	0.5		
440	1.6			

ture T_K and the Curie temperature T_C of amorphous Fe–Cr–B alloys on chromium concentration.

It has been calculated the effective spin–orbit interaction parameter λ_{SO} in ferromagnetic amorphous alloys of the Fe–Cr–B system using formula (5). The results of calculations are presented in Table 2.

As shown in Table 2, the effective spin–orbit interaction parameter in the ferromagnetic state depends only weakly on temperature and decreases with rising temperature. These results imply that, in the ferromagnetic state, the effective spin–orbit interaction parameter λ_{SO} is mainly associated with the reduction of spin scattering of charge carriers [34, 35].

4. CONCLUSION

Based on the obtained results, the following conclusions may be drawn.

Analysis of the temperature dependences of $\rho(T)$ and $R(T)$ reveals that increasing the metalloid concentration in the investigated amorphous alloys leads to an increase in the Hall coefficient and the crystallization temperature, while the Curie temperature decreases.

In the studied samples, increasing metalloid concentrations increases the absolute value of their electrical resistivity and crystallization temperature. The temperature of crystallization decreases.

A comprehensive experimental investigation of the electrical and galvanomagnetic properties of amorphous Fe–Cr–B alloys enables the estimation of the effective spin–orbit interaction parameter for these samples.

AUTHORS' CONTRIBUTIONS

O. Kuvandikov and I. Subkhankulov supervised the project, developed

the main conceptual ideas, checked the analytical approaches and provided critical feedback. N. S. Hamraev and R. M. Razhabov developed the project, reviewed the literature and collected data on electronic and mechanical properties, supervised the results of this work and provided feedback. Sh. A. Khomitov obtained the results of the experimental experiment, reviewed the literature and collected data on electronic and mechanical properties, and wrote the manuscript taking into account the contributions of all authors. O. Z. Turgunov obtained the results of the experimental experiment, reviewed the literature and compared the obtained experimental results with the literature. All authors approved the final version of the manuscript.

REFERENCES

1. K. Russew and L. Stojanova, *Production, Properties and Applications of Glassy Metals* (Berlin–Heidelberg: Springer: 2016).
2 V. K. Nosenko, *Visn. Nac. Acad. Nauk Ukr.*, **4**: 68 (2015) (in Ukrainian).
3. O. K. Kuvandikov, I. Subxankulov, D. H. Imamnazarov, and Sh. A. Khomitov, *Metallofiz. Noveishie Tekhnol.*, **44**, No. 7: 823 (2022).
4. O. M. Hertsyk, T. H. Hula, O. A. Yezerska, and M. O. Kovbuz, *Mater. Sci.*, **59**, No. 4: 546 (2024).
5. R. Hasegawa, *Applications of Amorphous Magnetic Alloys, Properties and Applications of Nanocrystalline Alloys from Amorphous Precursors (NATO Science Series, Vol. 184)* (Eds. B. Idzikowski, P. Švec, and M. Miglierini) (Dordrecht: Springer: 2005), pp. 189–198.
6. F. C. Li, T. Liu, J. Y. Zhang, S. Shuang, Q. Wang, A. D. Wang, J. G. Wang, and Y. Yang, *Mater. Today Adv.*, **4**: 100027 (2019).
7. R. Hasegawa, *J. Non-Cryst. Solids*, **287**, Nos. 1–3: 405 (2001).
8. O. Kuvandikov, N. S. Hamraev, R. M. Razhabov, I. Subkhankulov, S. A. Khomitov, and D. H. Imamnazarov, *Bull. Russ. Acad. Sci. Phys.*, **88**, No. 12: 2055 (2024).
9. A. Inoue and A. Takeuchi, *Acta Mater.*, **59**, No. 6: 273 (2010).
10. E. Axinte, *Mater. Des.*, **35**: 518 (2012).
11. F. R. Ismagilov, L. Papini, V. E. Vavilov, and D. V. Gusakov, *IEEE Trans. Ind. Electron.*, **67**, No. 3: 1750 (2020).
12. M. M. Khan, K. M. Deen, and W. Haider, *J. Non-Cryst. Solids*, **523**: 119544 (2019).
13. A. Jabed, M. M. Khan, J. Camiller, M. Greenlee-Wacker, W. Haider, and I. Shabib, *Surf. Coat. Technol.*, **372**: 278 (2019).
14. Jinn P. Chu, J. S. C. Jang, J. C. Huang, H. S. Chou, and Y. Yang, *Thin Solid Films*, **520**, No. 16: 5097 (2012).
15. M. Yu. Barabash, L. Yu. Kunyts'ka, L. G. Khomenko, and Yu. A. Kunyts'ky, *J. Nano- Electron. Phys.*, **2**, No. 1: 42 (2010).
16. A. P. Shpak, Yu. A. Kunits'kii, M. I. Zakharenko, and A. S. Voloshchenko, *Magnetyzm Amorfnykh ta Nanokrystalichnykh System* [Magnetism of Amorphous and Nanocrystalline Systems] (Kyiv: Akademperiodika: 2003) (in Ukrainian).

17. Q. J. Chen, *A Method for Crystallizing Fe-Based Amorphous Alloy, Fe-Based Amorphous Alloys with High Glass Forming Ability* (Singapore: Springer: 2025), p. 517.
18. L. J. van der Pauw, *A Method of Measuring Specific Resistivity and Hall Effect of Discs of Arbitrary Shape, Semiconductor Devices: Pioneering Papers* (Ed. S. M. Sze) (Singapore: World Scientific: 1991), pp. 174–182.
19. I. V. Zolotukhin, *Sorovsk. Obraz. Zh. Fiz.*, **4**: 73 (1997) (in Russian).
20. P. N. V'yugov and A. E. Dmitrenko, *Vopr. At. Nauki Tekh., Ser.: Vak., Chist. Mater., Sverkhprovodn.*, **6**: 185 (2004) (in Russian).
21. L. J. van der Pauw, *Philips Res. Repts*, **13**, No. 1: 1 (1958).
22. Y. Geng, *J. Phys.: Conf. Ser.*, **2321**: 012027 (2022).
23. J. D. Weiss, R. J. Kaplar, and K. E. Kambour, *Solid-State Electron.*, **52**, No. 1: 91 (2008).
24. U. Ausserlechner, *Solid-State Electron.*, **133**: 53 (2017).
25. M. Trudeau, R. W. Cochrane, D. V. Baxter, J. O. Strom-Olsen, and W. B. Muir, *Positive Phys. Rev.*, **37**, No. 9: 4499 (1988).
26. O. Kuvandikov, I. Subkhankulov, R. M. Razhabov, and S. A. Khomitov, *Bull. Russ. Acad. Sci. Phys.*, **88**, No. 11: 1836 (2024).
27. O. Kuvandikov, I. Subkhankulov, R. M. Razhabov, N. Hamraev, S. Khomitov, and D. Imamnazarov, *AIP Conf. Proc.*, **3377**, No. 1: 050006 (2025).
28. O. K. Kuvandikov, I. Subxankulov, B. U. Amonov, and D. H. Imamnazarov, *Metallofiz. Noveishie Tekhnol.*, **43**, No. 12: 1601 (2021).
29. J. H. Mooij, *Phys. Status Solidi A*, **17**, No. 2: 521 (1973).
30. N. F. Mott and E. A. Davis, *Electronic Processes in Non-Crystalline Materials* (Oxford: Clarendon Press: 1979).
31. O. Kuvandikov, I. Subkhankulov, N. S. Hamraev, R. M. Razhabov, Sh. A. Khomitov, and O. Z. Turgunov, *The Third International Forum 'PHYSICS–2024'* (Samarkand: 2024), p. 109.
32. D. M. Minić and A. Maričić, *Mater. Sci. Eng. B*, **172**, No. 2: 127 (2010).
33. O. K. Kuvandikov, Z. M. Shodiev, Kh. B. Khasanov, B. A. Khairullaev, and J. Sh. Akhtamov, *Metallofiz. Noveishie Tekhnol.*, **47**, No. 6: 595 (2025).
34. P. Ogrodnik, K. Grochot, Ł. Karwacki, J. Kanak, M. Prokop, J. Chęciński, W. Skowroński, S. Ziętek, and T. Stobiecki, *ACS Appl. Mater. Interfaces*, **13**, No. 39: 47019 (2021).
35. C. M. Hurd, *The Hall Effect in Metals and Alloys* (New York: Plenum Press: 1972).

Metallophysics and Advanced Technologies
Металофіз. новітні технол.
Metallofiz. Noveishie Tekhnol.
2026, vol. 48, No. 9, pp. 931–947
https://doi.org/10.15407/mfint.48.09.0931
Reprints available directly from the publisher

© 2026 G. V. Kurdyumov Institute for Metal Physics,
National Academy of Sciences of Ukraine
Published by license under
the G. V. Kurdyumov Institute for Metal Physics–
N.A.S. of Ukraine Publishers imprint.
Printed in Ukraine.

PACS numbers: 05.40.-a, 61.72.Bb, 61.72.Lk, 62.20.F-, 62.25.Fg, 83.50.-v, 83.60.-a

Length of a Critical Dislocation Segment under the Influence of Thermal Fluctuations

M. I. Lugovy, D. G. Verbylo, M. P. Brodnikovskyy, T. I. Verbytska*, D. S. Leonov**, and M. Yu. Barabash*,**,***,****

I. M. Frantsevich Institute for Problems in Materials Science, N.A.S. of Ukraine,
3 Omeljan Pritsak Str.,
UA-03142 Kyiv, Ukraine
**National Technical University of Ukraine*
'Igor Sikorsky Kyiv Polytechnic Institute',
37 Beresteiskyi Ave.,
UA-03056 Kyiv, Ukraine
***Technical Centre, N.A.S. of Ukraine,*
13 Pokrovs'ka Str.,
UA-04070 Kyiv, Ukraine
****Institute for Applied Control Systems, N.A.S. of Ukraine,*
42 Academician Hlushkov Ave.,
UA-03187 Kyiv, Ukraine
*****Gas Institute, N.A.S. of Ukraine,*
39 Dehtyarivs'ka Str.,
UA-03113 Kyiv, Ukraine

The thermal motion of atoms and, in other words, thermal fluctuations or distortions of crystal lattice caused by this motion lead to a wavy shape of the dislocation line both in alloys, where there are dissolved atoms, and in pure metals, where there are no such atoms. The wavy shape of the dislocation line, in turn, indicates that there are obstacles to the movement of the dislocation in the material. This means the threshold stress to initiate the disloca-

Corresponding author: Tetyana Ivanivna Verbytska
E-mail: verbutska@gmail.com

Citation: M. I. Lugovy, D. G. Verbylo, M. P. Brodnikovskyy, T. I. Verbytska, D. S. Leonov, and M. Yu. Barabash, Length of a Critical Dislocation Segment under the Influence of Thermal Fluctuations, *Metallofiz. Noveishie Tekhnol.*, **48**, No. 9: 931–947 (2026). DOI: 10.15407/mfint.48.09.0931

© Publisher PH 'Akademperiodyka' of the NAS of Ukraine, 2026. This is an open access article under the CC BY-ND license (https://creativecommons.org/licenses/by-nd/4.0)

tion movement could be very probable. In such a way, the dislocation line shape can affect the yield strength of the metal or alloy. The interaction of thermal fluctuation with a dislocation is considered as kind of 'push' into the dislocation of an atom in thermal motion. The dislocation-line shape under thermal-fluctuations' action is determined by the discrete dislocation dynamics method and in the form of an analytical solution of the differential equation for an elastic string with fixed ends. The standard deviation of dislocation-line points from the straight line and the averaged bulge length under thermal fluctuations action, determined by discrete dislocation dynamics and the analytical method, correlate well with each other, confirming the reliability of the modelling results. The standard deviation increases in proportion to the square root of the dislocation-line length at constant temperature and is also proportional to the square root of the temperature at constant dislocation-line length. The averaged bulge length, which determines the critical dislocation-segment length, is directly proportional to the dislocation-line length at constant temperature and does not depend on temperature at constant dislocation-line length.

Key words: dislocation, shear stress, standard deviation, length of the critical dislocation segment, thermal fluctuations.

Розглянуто вплив термічних флюктуацій на форму лінії дислокації. Взаємодія термічної флюктуації з дислокацією розглядається як своєрідний «поштовх» у неї атому, який перебуває в тепловому русі. Форму лінії дислокації під дією термічних флюктуацій визначено, з одного боку, за допомогою дискретної дислокаційної динаміки та, з іншого боку, у вигляді аналітичного рішення загального диференційного рівняння для пружньої струни з закріпленими кінцями. Запропоновано спосіб розрахунку характеристик «хвилястости» лінії дислокації, яку викликано термічними флюктуаціями. Цей спосіб уможливлює розраховувати стандартний відхил точок лінії дислокації від прямої та довжину усередненої випуклости на ній. Довжина усередненої випуклости визначає довжину критичного сеґмента дислокації. Показано, що характеристики, розраховані аналітичною методою та за допомогою комп'ютерного моделювання методою дискретної дислокаційної динаміки, добре корелюють між собою. Визначено також температурні залежності цих характеристик. Стандартний відхил пропорційний кореню квадратному з температури, а довжина критичного сеґмента від температури не залежить.

Ключові слова: дислокація, зсувне напруження, стандартний відхил, довжина критичного сеґмента, термічні флюктуації.

(Received 12 August, 2026; in final version, 17 August, 2026)

1. INTRODUCTION

Thermal fluctuations, thermal motions of atoms are present in all materials. They affect the shape of the dislocation line. This line cannot maintain a straight shape under such conditions and becomes wavy [1].

The shape of the dislocation line, in turn, can affect the formation of the yield point of a metal or alloy. The yield point is an important mechanical characteristic of metal alloys from the point of view of their engineering applications. Among various alloys, multicomponent alloys can be distinguished as particularly promising [2, 3]. The study of solid solution strengthening—the basic mechanism for increasing the yield point of such alloys—has been the subject of many works in the past [4–12]. In addition, attention has been paid to the temperature dependence of the yield point of alloys both theoretically [13–23] and experimentally [24–26]. Various aspects of the thermal activation motion of dislocations and the temperature dependence of the yield point were also studied in [27–30]. The calculation of solid solution strengthening of multicomponent heat-resistant alloys [31, 32] and the determination of crystal lattice distortion [33] are also important. Modelling the shear stress field in the glide plane in a substitutional solid solution and the movement of dislocations in this field provides new opportunities in such studies [34–37]. The temperature dependence of the yield point in an alloy can also be determined in terms of two components of the shear stress field in the glide plane [38]. Important issues in this regard remain the method of determining the parameters of the shear stress field and the correct description of the dependence of lattice distortion on temperature in a multicomponent alloy [39, 40].

The shape of an elastic line, which is fixed at both ends, under the action of thermal fluctuations at thermal equilibrium was modelled by the method of discrete dislocation dynamics in [1]. In order to investigate the dynamics of the shape change, an initially straight elastic line was considered, which then moved under the action of random thermal forces in the overdamped regime. The coefficient of resistance to the movement of the dislocation was considered directly proportional to the temperature, and the time step was equal to 50 fs. The shapes of the dislocation line were modelled for temperatures of 300, 600, 900 and 1200 K. After a sufficient modelling time, the system reached thermal equilibrium and the average kinetic energy per each degree of freedom became equal to the standard thermodynamic quantity for a given temperature, and the velocities of the discrete elements of the dislocation line had a Maxwell distribution.

In Ref. [1], the transient dynamics of the dislocation line shape before reaching thermal equilibrium was also studied. The initial shape was a straight line, which gradually transformed under the action of thermal fluctuations into a self-similar ‘wavy’ shape. This process was characterized by a structure factor, which was defined as the average absolute value of the difference in coordinates in the direction perpendicular to the initial line of two discrete dislocation elements located at a given distance from each other along this initial line. It is obvious

that, for the initial line, this parameter is zero for all distances between discrete elements along this line. Further, as thermal equilibrium approaches, the dependence of this factor on the distance along the initial line has two characteristic regions. For small distances, this dependence is approximately a straight line on a double logarithmic graph, which corresponds to a self-similar shape. For large distances, this parameter reaches a certain value that does not depend on the distance and essentially determines the width of the 'wavy' line in the direction perpendicular to the initial line. This width gradually increases with time in the transition period until complete thermal equilibrium is achieved. The distance along the initial line along which the transition between the two characteristic regions occurs also increases under these conditions. However, the characteristics of the 'wavy' dislocation line under the action of thermal fluctuations in the state of thermal equilibrium, when these characteristics become independent of time, were not considered in Ref. [1].

The movement of a dislocation occurs by gradually moving its individual critical segments due to the formation and transformation of bulges on them [38]. Therefore, the average length and height of the bulge on the dislocation as parameters of the critical segment are very important for describing the dislocation motion and, mostly, the yield strength of the alloy. In an alloy, in a solid solution, these parameters determine the effective dimensions of the obstacle created by dissolved atoms for such motion [38]. Thermal fluctuations and the distortions associated with them also lead to the 'waviness' of the dislocation line even in the absence of dissolved atoms. Bulges on the dislocation line, which are formed due to the thermal motion of atoms, in contrast to bulges formed under the action of dissolved atoms, are dynamic, not stationary and change with time, but their average length will also determine the length of certain critical segments. It is important that this length be determined in a state of thermal equilibrium, when these characteristics become independent of time.

The goal of this work is to calculate, by analytical method and using computer modelling by the method of discrete dislocation dynamics, the standard deviation of the points of the dislocation line from the straight line and the length of the averaged bulge on it, *i.e.*, the length of the critical dislocation segment, in the case of thermal fluctuations, and to determine the temperature dependences of these characteristics.

2. CALCULATION ALGORITHMS

Consider a dislocation with length l, which is fixed at the ends. We will assume that in the glide plane a coordinate system is given, where the axis x is directed in the direction of dislocation movement, perpendicu-

lar to the dislocation line, and the axis z is in the direction of the dislocation line, *i.e.*, parallel to it. We can discretize the dislocation line, *i.e.*, represent it as a chain of separate segments with the length of each Δz ($\Delta z << 1$), which are parallel to the axis z. We will also assume that each segment interacts with neighbouring segments due to the linear tension force. The equation of motion of such a separate dislocation segment along the axis x under the action of thermal fluctuations can be proposed in a certain approximation in a form similar to the works [1, 34, 37]:

$$m_0 \frac{\partial^2 u_i}{\partial t^2} + B \frac{\partial u_i}{\partial t} - \Gamma \frac{u_{i-1} - 2u_i + u_{i+1}}{\Delta z^2} = f_T(z_i, t), \quad (1)$$

where $u_i = u_i(z_i, t)$ is the displacement from the zero position along the coordinate x of the dislocation segment, which has the coordinate of its centre $z_i = \Delta z i$ at the time instant t ($u_i(z_i, t)$ essentially determines the shape of the dislocation line at the time instant t, $i = 1, 2, \ldots, l/\Delta z$), x is the coordinate in the direction of dislocation movement, z is the coordinate in the direction of the dislocation line, xOz is the dislocation glide plane, m_0 is the effective mass of the dislocation per unit length ($m_0 \approx \rho b^2/2$) [1], $m_0 \Delta z$ is the mass of the dislocation segment, ρ is the density of the material, b is the length of the Burgers vector, B is the coefficient of resistance to movement (it can be assumed that this coefficient is directly proportional to the temperature T [1], *i.e.*, $B = qT$, where q is the proportionality coefficient, such an assumption simplifies further consideration and gives a good approximation for temperatures that are not too close to zero), Γ is the linear tension of the dislocation line ($\Gamma = \alpha G b^2$, where α is the coefficient ($0 < \alpha \le 0.5$), G is the shear modulus), $f_T(z_i, t)$ is the force per unit length acting on the dislocation segment from the side of atoms that are in thermal motion, in the direction of the axis x. This force for each segment at each time step Δt in numerical simulation can be given as [1]:

$$f_T(z_i, t) = s_T Z_i, \quad (2)$$

where $s_T = \sqrt{2Bk_BT/(\Delta z \Delta t)}$ is the standard deviation of the force that ensures the existence of thermal equilibrium in the system, when the energy transferred from the atoms to the dislocation segment is returned back to the atoms due to the viscous resistance of the dislocation motion, Z_i is a random variable with a normal probability distribution and a mean value equal to 0 and a variance equal to 1 (a standard normal random variable for each i), k_B is the Boltzmann constant. It should be noted that $(u_{i-1} - 2u_i + u_{i+1})/\Delta z^2$ is the numerical representation of the second partial derivative $\partial^2 u(z, t)/\partial z^2$, which determines the curvature of the dislocation line, the shape of which at a certain time is

given by the function $u(z, t)$. We also note that we can set $\Delta t = 0.5b/c$, where $c = \sqrt{G/\rho}$ is the velocity of transverse sound vibrations in the material. It can be found $u_i(z_i, t)$ for all segments at a given time if we numerically, step by step in time, solve the system of equations (1) for the initial conditions $u_i(z_i, 0) = 0$ and $\dot{u}_i(z_i, 0) = 0$ (*i.e.*, at the beginning the dislocation is straight and stationary) and the boundary conditions $u(0, t) = u(l, t) = 0$ (*i.e.*, the ends of the dislocation are fixed). This method of determining the shape of a dislocation line is called the method of discrete dislocation dynamics.

It is also possible to solve analytically the general differential equation for the same initial and boundary conditions. The general equation will be similar to Eq. (1) for a separate segment,

$$m_0 \frac{\partial^2 u(z,t)}{\partial t^2} + B \frac{\partial u(z,t)}{\partial t} - \Gamma \frac{\partial^2 u(z,t)}{\partial z^2} = f_T(z,t)\,, \tag{3}$$

and it is very easy to reduce to a standard form:

$$\ddot{u}(z,t) + 2\delta \dot{u}(z,t) - c^2 \frac{\partial^2 u(z,t)}{\partial z^2} = \frac{f_T(z,t)}{m_0}\,, \tag{4}$$

where $\delta = B/2m_0$, and $c = \sqrt{\Gamma/m_0}$ is the second definition of the velocity of transverse sound vibrations in the material. The solution of equation (4) is sought in the form of

$$u(z,t) = \sum_{n=1}^{\infty} u_n(z,t) = \sum_{n=1}^{\infty} u_n(t) \sin(\pi n z/l)\,, \tag{5}$$

where $u_n(z, t)$ is called the n-th fundamental mode of oscillations of the elastic line (in our case, the dislocation), $n = 1, 2, \ldots$ and $u_n(t)$ is a solution of the equation:

$$\ddot{u}_n(t) + 2\delta \dot{u}_n(t) + \omega_n^2 u_n(t) = f_n(t)\,, \tag{6}$$

where $\omega_n = \pi n c/l$ and

$$f_n(t) = \frac{2}{l} \int_0^l \frac{f_T(z,t)}{m_0} \sin\left(\frac{\pi n}{l} z\right) dz = \frac{2T}{m_0} \sqrt{\frac{q k_B}{l \Delta t}} Z_j\,, \tag{7}$$

where Z_j is the standard normal random variable at each time step. Further,

$$u_n(t) = \int_0^t U(t-\tau) f_n(\tau) d\tau\,, \tag{8}$$

where $U(t)$ the function satisfies the equation

$$\ddot{U}(t) + 2\delta\dot{U}(t) + \omega_n^2 U(t) = 0 \tag{9}$$

with initial conditions $U(0) = 0$ and $\dot{U}(0) = 1$. Thus,

$$U(t) = \exp(-\delta t)\frac{\exp(t\sqrt{\delta^2 - \omega_n^2}) - \exp(-t\sqrt{\delta^2 - \omega_n^2})}{2\sqrt{\delta^2 - \omega_n^2}}. \tag{10}$$

If we substitute Eqs. (7) and (10) into Eq. (8), we obtain

$$u_n(t) = \sqrt{\frac{2lk_BT}{\pi^2 n^2 \Gamma}} Z_n \left\{1 - \frac{\exp(-\delta t)}{4(\delta^2 - \omega_n^2)} \times \right.$$
$$[\omega_n^2[\exp(t\sqrt{\delta^2 - \omega_n^2}) - \exp(-t\sqrt{\delta^2 - \omega_n^2})]^2 + \tag{11}$$
$$+[\lambda_1 \exp(t\sqrt{\delta^2 - \omega_n^2}) - \lambda_2 \exp(-t\sqrt{\delta^2 - \omega_n^2})]^{1/2},$$

where $\lambda_1 = \delta + \sqrt{\delta^2 - \omega_n^2}$ and $\lambda_2 = \delta - \sqrt{\delta^2 - \omega_n^2}$, Z_n are standard normal random variables for each n. It can be seen that for a sufficiently large time t due to $\exp(-\delta t)$ formula (11) simplifies to

$$u_n(t) = \sqrt{\frac{2lk_BT}{\pi^2 n^2 \Gamma}} Z_n. \tag{12}$$

The quantity $u_n(t)$ is the amplitude of the n-th fundamental mode $u_n(z, t)$, which is a sinusoid with wavelength $2l/n$. In fact, for a sufficiently large time t, there is no explicit dependence $u_n(t)$ on t. In this case, the amplitude of the sinusoid will simply be a random variable with a normal distribution. Negative amplitude means a change in the phase of the sinusoid by π radian. It is easy to prove the correctness of formula (12), if we take into account the fact that, under thermal equilibrium conditions, the average energy of the fundamental mode of the elastic line must be equal to $k_BT/2$. The energy of the fundamental mode in our case [1] is

$$E_n = \frac{\Gamma}{2}\int_0^l \left(\frac{\partial u_n(z,t)}{\partial z}\right)^2 dz = \frac{k_BT}{l} Z_n^2 \left.\frac{2\pi nz/l + \sin(2\pi nz/l)}{4\pi n/l}\right|_0^l = \frac{k_BTZ_n^2}{2}. \tag{13}$$

The average energy will accordingly be

$$< E_n >= \left\langle \frac{k_BT}{2} Z_n^2 \right\rangle = \frac{k_BT}{2} < Z_n^2 >= \frac{k_BT}{2} \times 1 = \frac{k_BT}{2}. \tag{14}$$

Thus, the function $u(z, t)$ that determines the shape of the dislocation line under the action of random forces from the atoms in thermal motion will be a superposition of fundamental modes—sinusoids with

corresponding wavelengths and random amplitudes. If we take into account Eqs. (5) and (12), we obtain

$$u(z,t) = \sqrt{\frac{2lk_BT}{\pi^2\Gamma}} \sum_{n=1}^{\infty} \frac{Z_n}{n} \sin(\pi n z / l) . \tag{15}$$

It is important to add that, if the shape of the dislocation line is determined by the method of discrete dislocation dynamics, when the dislocation is considered as a chain $N = l/\Delta z$ of segments, then, we have $u_i(z_i, t)$ for $N+1$ points, because the left end of the dislocation corresponds to $i = 0$. We also note that, under the boundary conditions, $u_0(0, t) = u_N(l, t) = 0$. In this case, we can expand $u_i(z_i, t)$ in a series in sines:

$$u_i(z_i, t) = \sum_{n=1}^{N} A_n \sin \frac{\pi n i}{N+1} , \tag{16}$$

where

$$A_n = \frac{2}{N+1} \sum_{i=1}^{N} u_i(z_i, t) \sin \frac{\pi n i}{N+1} . \tag{17}$$

If we compare Eqs. (15) and (16), then, from their similarity, it obviously follows that

$$A_n = \sqrt{\frac{2lk_BT}{\pi^2\Gamma}} \frac{Z_n}{n} , \tag{18}$$

and variable

$$\sqrt{\frac{\pi^2\Gamma}{2lk_BT}} n A_n = Z_n \tag{19}$$

has a normal distribution with a mean value of 0 and a variance of 1. In this way, it is possible to check the correspondence of the results obtained by the method of discrete dislocation dynamics to the analytical solution of the general differential equation.

If $u_i(z_i, t)$ are calculated, then, it is possible to find the characteristics of the thermal fluctuation 'waviness' of the dislocation line, namely the standard deviation of the magnitude s_u and the average length of the section L along the axis Oz, on which $u_i(z_i, t)$ has the same sign. That is, to find the parameters, which characterize the height and length of the average convexity on the dislocation line and, thus, its critical segment. It is enough to determine simply the intersection points of the dislocation line and the axis Oz. Then, it is easy to determine the length L, which will be equal to the length of the dislocation

line l divided by the number of intersection points [34]. A feature of the definition of s_u and L are the averaging of these characteristics also over different moments of time t, *i.e.*, $u_i(z_i, t)$ should take part in the consideration not for one moment t, but for many moments.

Taking into account Eqs. (15) and (16), we can represent has a normal distribution with a mean value of 0 and a variance of 1. In this way, it is possible to check the correspondence of the results obtained by the method of discrete dislocation dynamics to the analytical solution of the general differential equation.

Taking into account Eqs. (15) and (16), we can represent

$$s_u = \sqrt{\frac{2lk_BT}{\pi^2\Gamma}}\sqrt{D\left[\sum_{n=1}^{N}\frac{Z_n}{n}\sin\left(\frac{\pi ni}{N+1}\right)\right]} = \sqrt{\frac{2lk_BT}{\pi^2\Gamma}}\bar{s}_u\,, \tag{20}$$

where $(2lk_BT/\pi^2\Gamma)^{1/2}$ contains physical quantities, $D[\ldots]$ means the variance of the random variable, which is in brackets, and in our case this quantity does not depend on any physical parameter and takes different values for different i. Numerical calculations show that $\bar{s}_u = 0.47 \pm 0.08$ for $N = 1000$. For analytical evaluation of L, a model similar to the model given in Ref. [39] can be applied. To do this, consider the distribution of positive values inside the corresponding averaged section $u(z, t)$ along the axis Oz. The length of such a section will be equal to L, by definition. If $u_i(z_i, t)$ have a normal distribution with zero mathematical expectation and standard deviation s_u, then, the sample of only positive values from them has a mean value $s_u(2/\pi)^{1/2}$. At the endpoints of such a section, $u(z, t)$ will be equal to zero, and further from each endpoint of $u(z, t)$ should increase towards the middle of the section, since the mean value of $u(z, t)$ is greater than zero. This increase will be symmetrical about the midpoint of the plot because the parts of the averaged plot on both sides of the midpoint are absolutely equal and have no advantages over each other due to the uniformity of the statistical distribution $u(z, t)$. Thus, the averaged distribution of $u(z, t)$ will be a smooth curve symmetric about the maximum at the midpoint of the plot. If we average only the positive values of the gradient $\partial u(z, t)/\partial z$ from the end point of the averaged plot to its middle, then, similarly to $u(z, t)$, we will have the average value of the gradient $s_{gu}(2/\pi)^{1/2}$, where s_{gu} is the standard deviation of the gradient. The averaged distribution $u(z, t)$ can be approximated by a suitable function, for example $A_u\cos(\pi z/L)$, where $A_u = s_u(\pi/2)^{1/2}$. Then, the average value of the gradient $\partial u(z, t)/\partial z$ on the plot, where it is positive, is $2A_u/L$, from which it is easy to obtain

$$L = \pi s_u / s_{gu}\,. \tag{21}$$

On the other hand, taking into account Eq. (15), the gradient is

equal to

$$\frac{\partial u(z,t)}{\partial z} = \sqrt{\frac{2k_BT}{\Gamma l}} \sum_{n=1}^{N} Z_n \cos\frac{\pi n i}{N+1}, \tag{22}$$

and

$$s_{gu} = \sqrt{\frac{2k_BT}{\Gamma l}} \sqrt{D\left[\sum_{n=1}^{N} Z_n \cos\left(\frac{\pi n i}{N+1}\right)\right]} = \sqrt{\frac{2k_BT}{\Gamma l}} \bar{s}_{gu}, \tag{23}$$

where numerical calculations show that $\bar{s}_{gu} = 22.36$ for $N = 1000$, that is, according to Eq. (21) for $N = 1000$,

$$L = l s_u / s_{gu} \approx l / 55. \tag{24}$$

Thus, the length L turns out to be proportional to the length of the dislocation line fixed at the ends l.

3. RESULTS AND DISCUSSION

The initial parameters for modelling the effect of thermal fluctuations on the characteristics of the average bulge on the dislocation line by the discrete dislocation dynamics method and calculating these characteristics by the analytical method are given in Table 1 [37]. The time step Δt was defined as $3.93 \cdot 10^{-14}$ s. The modelling by the discrete dislo-

TABLE 1. Initial parameters for modelling the influence of thermal fluctuations on the characteristics of the average convexity on the dislocation line [37].

G, GPa	81	m_0, kg/m	$2.5 \cdot 10^{-16}$
ν	0.3	ρ, kg/m^3	8000
α	0.123	c, m/s	3182
b, nm	0.25	Γ, N	$6.23 \cdot 10^{-10}$

TABLE 2. Temperature dependence of the drag coefficient [1].

Temperature T, K	Coefficient of motion resistance B, MPa·s
300	$3 \cdot 10^{-11}$
600	$6 \cdot 10^{-11}$
900	$9 \cdot 10^{-11}$
1200	$1.2 \cdot 10^{-10}$

cation dynamics method was carried out separately for $\Delta z = 2b$, $5b$, $10b$, $20b$ and $40b$ at a temperature of 300 K, as well as separately for temperatures of 300, 600, 900 and 1200 K at $\Delta z = 10b$. The dislocation was represented as a chain of $N = 1000$ segments. It should be noted that, under these conditions, $\Delta z = 2b$, $5b$, $10b$, $20b$ and $40b$ corresponded to the lengths of the fixed dislocation line $l = 500$ nm, 1250 nm, 2500 nm, 5000 nm and 10000 nm. The temperature dependence of the drag coefficient B is given in Table 2 [1]. During each simulation, 125000 time steps were taken, corresponding to 4.91 ns of model time. Thermal equilibrium was considered to be reliably reached after 50000 time steps, *i.e.*, after 1.96 ns of model time. The characteristics of the average bulge on the dislocation line, which were determined from the simulation results using the discrete dislocation dynamics method, were averaged for all time steps from the 50000th step to the 125000th step, *i.e.*, from 1.96 ns to 4.91 ns of model time.

An example of the dislocation line shape under the influence of thermal fluctuations, simulated by the method of discrete dislocation dynamics, at the 125000th time step ($\Delta z = 10b$, $T = 300$ K, $t = 4.91$ ns) is shown in Fig. 1. The dashed line shows the initial line shape for $t = 0$. It is seen that the dislocation line becomes randomly 'wavy' under the influence of thermal fluctuations.

The average energy of the fundamental mode (average kinetic energy of dislocation segments) from the 50000th step to the 125000th step in time, *i.e.*, in the thermal equilibrium region, is shown in Fig. 2. The discrete dislocation dynamics simulation was performed for $\Delta z = 10b$ and $T = 300$ K. The dashed line shows for comparison the standard thermodynamic value of the average kinetic energy per degree of freedom for a given temperature of 300 K $<E_n> = k_B T/2 = 0.0129$ eV.

The dependence of the standard deviation of the dislocation line points from the initial straight-line s_u on the length of this line l under the action of thermal fluctuations is shown in Fig. 3. Note that, for the simulation, $\Delta z = 2b$, $5b$, $10b$, $20b$ and $40b$ were used, *i.e.*, the lengths of the fixed dislocation line were $l = 500$ nm, 1250 nm, 2500 nm, 5000 nm and 10000 nm, respectively. The simulation was performed for a temperature of $T = 300$ K. The circles show the results of the simulation using the discrete dislocation dynamics method. The line is a calculation using formula (20), *i.e.*, an analytical method. We note a good correlation between the results of calculations using both methods. The standard deviation increases in proportion to the square root of the length of the dislocation line.

The dependence of the length L of the average bulge (critical segment) on the length of this line l under the action of thermal fluctuations is shown in Fig. 4. The simulation conditions are indicated above. The circles also show the results of the simulation using the discrete dislocation dynamics method, and the line shows the results of the cal-

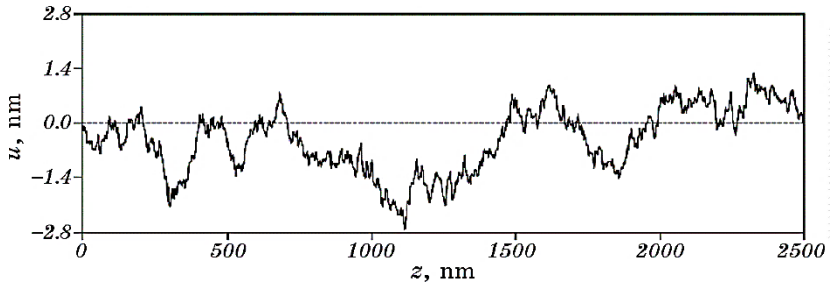


Fig. 1. Dislocation line under the influence of thermal fluctuations, simulated by the method of discrete dislocation dynamics, at the 125000th time step ($\Delta z = 10b$, $T = 300$ K, $t = 4.91$ ns); the dashed line shows the initial dislocation line for $t = 0$.

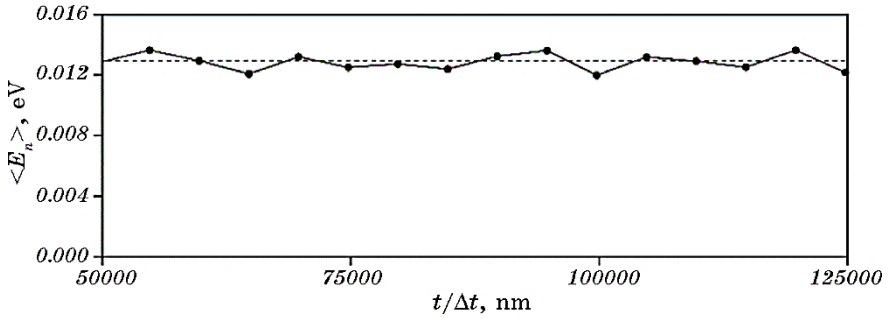


Fig. 2. The average energy of the fundamental mode (average kinetic energy of dislocation segments) from the 50000th step to the 125000th step in time ($\Delta z = 10b$, $T = 300$ K); the dashed line shows the standard thermodynamic value of the average kinetic energy per degree of freedom for a given temperature of 300 K ($k_B T/2 = 0.0129$ eV).

culation using formula (24). The results of the calculations using both methods also correlate well with each other. The length of the critical segment is directly proportional to the length of the dislocation line under these conditions.

The dependence of the standard deviation of the dislocation line points from the initial straight-line s_u on temperature at a constant dislocation line length of 2500 nm under the action of thermal fluctuations is shown in Fig. 5. Note that the simulation was performed for $\Delta z = 10b$ and temperature 300, 600, 900 and 1200 K. The circles again show the Δz results of the simulation using the discrete dislocation dynamics method, and the line is the calculation using the analytical method according to formula (20). The correlation between the results of the calculations using both methods in this case is excellent. The standard deviation turns out to be proportional to the square root of

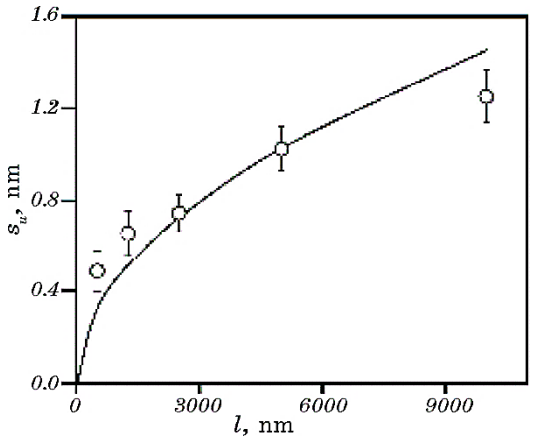


Fig. 3. Dependence of the standard deviation of the points of the dislocation line from the initial straight line on the length of this line ($\Delta z = 2b$, $5b$, $10b$, $20b$, $40b$, $T = 300$ K). Circles are calculations using the method of discrete dislocation dynamics. Lines are calculations using formula (20).

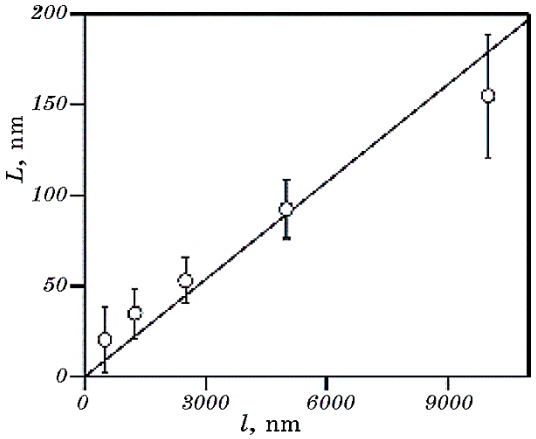


Fig. 4. Dependence of the length of the average convexity (critical segment) on the length of the dislocation line ($\Delta z = 2b$, $5b$, $10b$, $20b$, $40b$, $T = 300$ K). Circles are calculations using the method of discrete dislocation dynamics. Lines are calculations using formula (24).

the temperature.

The dependence of the length of the average bulge (critical segment) L on temperature at a constant dislocation line length of 2500 nm under the action of thermal fluctuations is shown in Fig. 6.

The simulation was performed using $\Delta z = 10b$ for temperature of 300, 600, 900 and 1200 K. The results of the simulation using the dis-

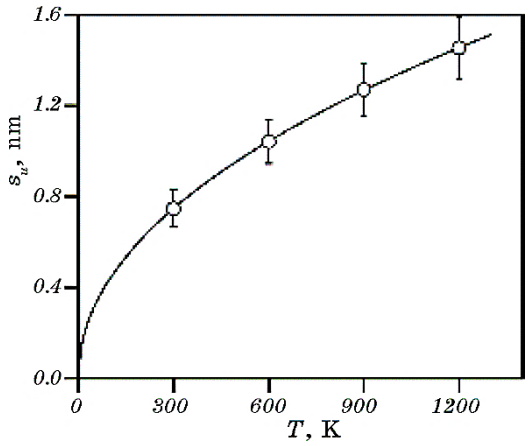


Fig. 5. Dependence of the standard deviation of the dislocation line points from the initial straight line on temperature at a constant dislocation line length of 2500 nm ($\Delta z = 10b$, $T = 300$, 600, 900, 1200 K). Circles are calculations using the method of discrete dislocation dynamics. Lines are calculations using formula (20).

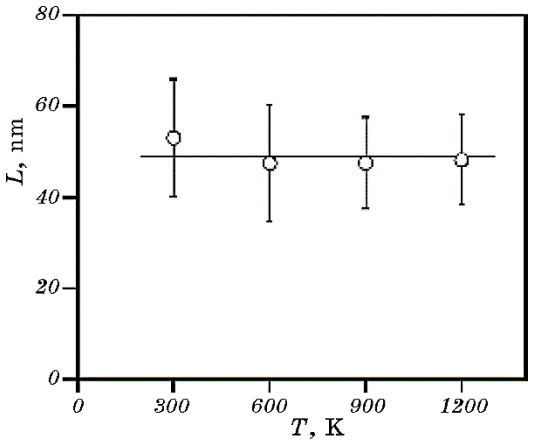


Fig. 6. Dependence of the length of the average convexity (critical segment) on temperature for a constant dislocation line length of 2500 nm ($\Delta z = 10b$, $T = 300$, 600, 900, 1200 K). Circles are calculations using the method of discrete dislocation dynamics. Line is calculations using formula (24).

crete dislocation dynamics method are shown by circles, and the results of the calculations using the analytical method (formula (24)) are shown by a solid line. The results of the calculations using both methods also confirm each other well. The length of the critical segment turns out to be independent of temperature under these conditions.

4. CONCLUSION

Thermal motion of atoms, or, in other words, thermal fluctuations or distortions of crystal lattices caused by this motion, lead to a wavy shape of the dislocation line both in alloys where there are dissolved atoms and in pure metals where there are no dissolved atoms.

The wavy shape of the dislocation line, in turn, indicates that there are obstacles to the movement of the dislocation in the material, that is, we can expect the existence of a limiting value of external mechanical stress that can initiate the movement of the dislocation, that is, the shape of the dislocation line can affect the yield point of the metal or alloy.

Thus, the characteristics of the 'waviness' of the dislocation line, namely the standard deviation of the points of the dislocation line from the straight line and the length of the averaged bulge on it under the action of thermal fluctuations, are important parameters for understanding the formation of the yield point of the material.

These characteristics, which are determined on the one hand by means of discrete dislocation dynamics and on the other hand by analytical methods, correlate well with each other, which confirms the reliability of the modelling results.

The standard deviation increases proportionally to the square root of the dislocation line length at constant temperature, and is also proportional to the square root of the temperature at constant dislocation line length.

The length of the averaged bulge, which determines the length of the critical dislocation segment, is directly proportional to the dislocation line length at constant temperature, and does not depend on the temperature at constant dislocation line length.

The determined temperature dependencies of the standard deviation of the dislocation line points from the straight line and the length of the critical dislocation segment help to understand better the effect of thermal fluctuations on the dislocation line shape.

AUTHORS' CONTRIBUTIONS

M. I. Lugovy performed numerical calculations of shear stress field in the glide plane and wrote the manuscript with input from all authors. D. G. Verbylo reviewed the literature and wrote the manuscript with input from all authors. M. P. Brodnikovskyy verified analytical approaches and provided critical feedback. T. I. Verbytska interpreted results and curated data. D. S. Leonov visualized and verified results and prepared figures/tables. M. Yu. Barabash supervised the work and devised the main conceptual ideas. All authors approved the final version of the manuscript.

REFERENCES

1. J.-H. Zhai and M. Zaiser, *Mater. Sci. Eng. A*, **740–741**: 285 (2019).
2. D. B. Miracle and O. N. Senkov, *Acta Mater.*, **122**: 448 (2017).
3. E. P. George, W. A. Curtin, and C. C. Tasan, *Acta Mater.*, **188**: 435 (2020).
4. J. D. Eshelby, *Solid State Physics*, **3**: 79 (1956).
5. R. L. Fleischer, *Acta Metallurgica*, **11**: 203 (1963).
6. R. Labusch, *Czech J. Phys.*, **31**: 165 (1981).
7. L. A. Gypen and A. Deruyttere, *J. Mater. Sci.*, **12**: 1028 (1977).
8. A. S. Argon, *Strengthening Mechanisms in Crystal Plasticity* (Oxford: Oxford University Press: 2008).
9. U. F. Kocks, A. S. Argon, and M. F. Ashby, *Prog. Mater. Sci.*, **19**: 110 (1975).
10. F. R. N. Nabarro and P. B. Hirsch, *The Physics of Metals* (Cambridge: Cambridge University Press: 1976), p. 152.
11. M. Zaiser, *Phil. Mag. A*, **82**, Iss. 15: 2869 (2002).
12. I. Toda-Caraballo, *Scripta Mater.*, **127**: 113 (2017).
13. G. P. M. Leyson, W. A. Curtin, L. G. Hector Jr., and C. F. Woodward, *Nature Mater.*, **9**: 750 (2010).
14. G. P. M. Leyson, L. G. Hector, and W. A. Curtin, *Acta Mater.*, **60**: 3873 (2012).
15. G. P. M. Leyson and W. A. Curtin, Modelling Simul. Mater. Sci. Eng., **24**: 065005 (2016).
16. C. Varvenne, A. Luque, and W. A. Curtin, *Acta Mater.*, **118**: 164 (2016).
17. C. Varvenne, G. P. M. Leyson, M. Ghazisaeidi, and W. A. Curtin, *Acta Mater.*, **124**: 660 (2017).
18. G. Laplanche, J. Bonneville, C. Varvenne, W. A. Curtin, and E. P. George, *Acta Mater.*, **143**: 257 (2018).
19. W. G. Nöhring and W. A. Curtin, *Scripta Mater.*, **168**: 119 (2019).
20. G. Bracq, M. Laurent-Brocq, C. Varvenne, L. Perrière, W. A. Curtin, J.-M. Joubert, and I. Guillot, *Acta Mater.*, **177**: 266 (2019).
21. Y. Hu, B. A. Szajewski, D. Rodney, and W. A. Curtin, *Modelling Simul. Mater. Sci. Eng.*, **28**: 015005 (2020).
22. G. Péterffy, P. D. Ispánovity, M. E. Foster, X. Zhou, and R. B. Sills, *Mater. Theory*, **4**: 6 (2020).
23. R. Pasianot and D. Farkas, *Computational Mater. Sci.*, **173**: 109366 (2020).
24. F. Otto, A. Dlouhy, C. Somsen, H. Bei, G. Eggeler, and E. P. George, *Acta Mater.*, **61**: 5743 (2013).
25. A. Gali and E. P. George, *Intermetallics*, **39**: 74 (2013).
26. S. J. Sun, Y. Z. Tian, H. R. Lin, X. G. Dong, Y. H. Wang, Z. J. Wang, and Z. F. Zhang, *J. Alloys Compd.*, **806**: 992 (2019).
27. A. V. Podolskiy, E. D. Tabachnikova, V. V. Voloschuk, V. F. Gorban, N. A. Krapivka, and S. A. Firstov, *Mater. Sci. Eng. A*, **710**: 136 (2018).
28. S. O. Firstov, T. G. Rogul, N. A. Krapivka, and S. I. Chugunova, *Metallofiz. Noveishie Tekhnol.*, **40**: 219 (2018) (in Russian).
29. S. O. Firstov and T. G. Rogul, *Metallofiz. Noveishie Tekhnol.*, **39**: 33 (2017) (in Russian).
30. S. O. Firstov and T. G. Rogul, *Metallofiz. Noveishie Tekhnol.*, **44**: 127 (2022) (in Ukrainian).
31. M. Lugovy, V. Slyunyayev, M. Brodnikovskyy, and S. O. Firstov, *Ehlektronnaya Mikroskopiya i Prochnost' Materialov*, **23**: 3 (2017) (in Ukrainian).

32. M. Lugovy, V. Slyunyayev, and M. Brodnikovskyy, *Ehlektronnaya Mikroskopiya i Prochnost' Materialov*, **25**: 26 (2019) (in Russian).
33. M. Lugovy, V. Slyunyayev, and M. Brodnikovskyy, *Prog. Natural Sci. Mater. Int.*, **31**: 95 (2021).
34. M. Lugovy, D. Verbylo, and M. Brodnikovskyy, *Uspikhy Materialoznavstva*, **2**: 19 (2021) (in Ukrainian).
35. M. Lugovy, D. Verbylo, and M. Brodnikovskyy, *Uspikhy Materialoznavstva*, **3**: 24 (2021) (in Ukrainian).
36. M. Lugovy, D. Verbylo, and M. Brodnikovskyy, *Uspikhy Materialoznavstva*, **4/5**: 12 (2022) (in Ukrainian).
37. M. Lugovy, D. Verbylo, and M. Brodnikovskyy, *Uspikhy Materialoznavstva*, **4/5**: 36 (2022) (in Ukrainian).
38. M. Lugovy, D. Verbylo, and M. Brodnikovskyy, *Uspikhy Materialoznavstva*, **6**: 15 (2023) (in Ukrainian).
39. M. Lugovy, D. Verbylo, and M. Brodnikovskyy, *Uspikhy Materialoznavstva*, **7**: 3 (2023) (in Ukrainian).
40. M. Lugovy, D. Verbylo, and M. Brodnikovskyy, *Uspikhy Materialoznavstva*, **8/9**: 13 (2024) (in Ukrainian).

Metallophysics and Advanced Technologies
Металофіз. новітні технол.
Metallofiz. Noveishie Tekhnol.
2026, vol. 48, No. 9, pp. 949–962
https://doi.org/10.15407/mfint.48.09.0949
Reprints available directly from the publisher

© 2026 G. V. Kurdyumov Institute for Metal Physics,
National Academy of Sciences of Ukraine
Published by license under
the G. V. Kurdyumov Institute for Metal Physics–
N.A.S. of Ukraine Publishers imprint.
Printed in Ukraine.

PACS numbers: 46.25.-y, 46.50.+a, 46.70.De, 62.20.mj, 68.60.Bs, 81.40.Jj, 81.65.Mq

On the Effect of Residual Stresses on the Strength of Oxidized Plates under Thermomechanical Loading

I. P. Shatskyi, V. M. Petrashchuk, L. Ya. Ropyak*, and O. O. Lazarieva**

Pidstryhach Institute for Applied Problems of Mechanics and Mathematics,
N.A.S. of Ukraine,
3-b Naukova Str.,
UA-79060 Lviv, Ukraine
**Ivano-Frankivsk National Technical University of Oil and Gas,*
15 Karpatska Str.,
UA-76019 Ivano-Frankivsk, Ukraine
***Zaporizhzhia Polytechnic National University,*
64 Zhukovsky Str.,
UA-69063 Zaporizhzhya, Ukraine

This paper develops a methodology for investigating the stress–strain state and evaluating the load-bearing capacity of metal plates strengthened by plasma electrolytic oxidation of the surface layer. The object of analysis is a plate of symmetric structure with a double-side oxide coating subjected to biaxial tensile loading under uniform heating and in the presence of a self-equilibrated field of residual stresses. Within the framework of the plane-sections' and elastic-deformation hypothesis, the closed-form analytical expressions are obtained for the residual stresses in the substrate and in the oxide layers in terms of the incompatible strain of the surface layers, as well as for the total stress state under combined thermomechanical loading. Two strength criteria are formulated and analysed: a global (integral) criterion, which is insensitive to self-equilibrated residual and thermal components, and a local criterion, which reduces to a set of linear inequalities for the admissible load and temperature at a given level of residual stresses. The capa-

Corresponding author: Ivan Petrovych Shatskyi
E-mail: ipshatsky@gmail.com

Citation: I. P. Shatskyi, V. M. Petrashchuk, L. Ya. Ropyak, and O. O. Lazarieva, On the Effect of Residual Stresses on the Strength of Oxidized Plates under Thermomechanical Loading, *Metallofiz. Noveishie Tekhnol.*, **48**, No. 9: 949–962 (2026). DOI: 10.15407/mfint.48.09.0949

© Publisher PH 'Akademperiodyka' of the NAS of Ukraine, 2026. This is an open access article under the CC BY-ND license (https://creativecommons.org/licenses/by-nd/4.0)

bilities of the methodology are illustrated by computational examples for the Al/Al_2O_3 (6061-T6 alloy/aluminium oxide) and Ti/TiO_2 (Grade 2 titanium/titanium dioxide) compositions, with account of the Pilling–Bedworth ratio and the mismatch of linear thermal-expansion coefficients of the metal and its oxide. As shown, in the absence of thermal effects and residual stresses, the load-bearing capacity of an oxidized plate in tension is about three times lower than that of the uncoated plate, owing to high stress concentration in the thin stiff coating. The combinations of residual-stresses' level and temperatures are identified, at which an oxidized plate operates as an equal-strength structure with maximum load-bearing capacity; explicit analytical relations are obtained for both the Al/Al_2O_3 and Ti/TiO_2 systems.

Key words: plasma electrolytic oxidation, oxidized plate, residual stresses, thermomechanical loading, strength.

У статті розроблено методику дослідження напружено-деформованого стану й оцінювання утримувальної здатности металевих платівок, зміцнених плазмовим електролітичним оксидуванням поверхневого шару. Об'єктом аналізи є платівка симетричної будови з двостороннім оксидним покриттям, яка зазнає двовісного розтягувального навантаження за умов рівномірного нагрівання та наявности самозрівноважного поля залишкових напружень. У рамках гіпотези стосовно пласких перерізів і пружнього деформування одержано замкнуті аналітичні залежності для залишкових напружень у підкладинці й оксидних шарах через несумісну деформацію поверхневих шарів, а також для повного напруженого стану за комбінованого термомеханічного навантаження. Сформульовано та проаналізовано два критерії міцности: глобальний (інтеґральний) критерій, нечутливий до самозрівноважних залишкових і теплових компонент, та локальний критерій, який зводиться до системи лінійних нерівностей щодо допустимого навантаження та температури за заданого рівня залишкових напружень. Можливості методики проілюстровано на прикладах композицій Al/Al_2O_3 (стоп 6061-T6/оксид Алюмінію) та Ti/TiO_2 (титан ґатунку 2/діоксид Титану) з урахуванням коефіцієнта Піллінґа–Бедворта та ріжниці коефіцієнтів лінійного теплового розширення металу та його оксиду. Показано, що за відсутности температурного впливу та залишкових напружень несна здатність оксидованої платівки за розтягу приблизно втричі менша порівняно з неоксидованою через високу концентрацію напружень у тонкому цупкому покритті. Визначено співвідношення рівнів залишкових напружень і температур, за яких оксидована платівка працює як рівноміцна конструкція з максимальною утримувальною здатністю; одержано явні аналітичні залежності для обох систем — Al/Al_2O_3 й Ti/TiO_2.

Ключові слова: плазмове електролітичне оксидування, оксидована платівка, залишкові напруження, термомеханічне навантаження, міцність.

(Received 20 May, 2026; in final version, 27 May, 2026)

1. INTRODUCTION

Modern engineering design relies increasingly on the comprehensive

assessment of the strength and reliability of structural components under realistic service scenarios, as illustrated by the approaches presented in Refs. [1, 2]. The interaction between a structure and its environment, together with severe operating conditions, places stringent demands on researchers regarding corrosion protection, wear resistance, and the thermal insulation of component surfaces. Among the variety of methods available for surface strengthening of machine and mechanism parts [3–6], the method of plasma electrolytic oxidation (PEO) of valve metals occupies a special place [7–12]. Among the key advantages of PEO, there is the formation of ceramic-like layers with a developed structure, which are firmly bonded to the metallic substrate and provide a substantial enhancement of surface hardness, wear and corrosion resistance, as well as the thermal insulation characteristics of the component. At the same time, the process is environmentally safer than conventional anodizing, requires no complex preliminary surface preparation, and is readily scalable to articles of complex geometry.

However, the significant increase in the stiffness of oxidized surface layers is not always accompanied by a corresponding increase in their strength. Consequently, the transition from a ductile metal to a brittle ceramic may give rise to durability problems for coated parts. A high level of compressive residual stresses in the oxide coating frequently allows an appropriate balance between stiffness and strength to be maintained.

In general, theoretical methods for studying residual phenomena are well developed at present for plastic deformation processes [13–16] and for hysteretic energy dissipation in frictional contact [17–21]. Recent publications [22–29] cover measurement methods, the understanding of evolution, and experimental data on residual stresses in Al/Al_2O_3 and Ti/TiO_2 systems, in particular mentioning the curvature method, XRD, and the $\sin^2\psi$ method as experimental techniques. It should be noted that these publications exhibit a considerable scatter in experimental data on residual stresses in oxide coatings: from 20 to 1500 MPa, depending on the parameters of the oxidation process and the measurement techniques.

Analytical models of thermal stresses providing closed-form solutions for the stress distribution in layered structures under thermomechanical loading are described in Refs. [30–36]. The influence of nonstationary temperature variations is taken into account in Refs. [37–39]. Singular problems concerning the behaviour of layered and functionally graded coatings under localized contact loading have been the subject of investigations [40–44].

Issues of fracture mechanics and damage propagation criteria for structures with coatings are usually treated without accounting for residual phenomena [45–51]. An exception is paper [52], which de-

scribes models for the failure modes of PEO coatings under the influence of tensile and compressive residual stresses. Problems concerning the limit equilibrium of cracked thin-walled structures under combined loading were considered in Refs. [53–55].

The literature review presented above motivates the investigation of the strength of oxidized plates of symmetric structure under two-parameter loading over a wide range of variation of residual stresses.

The aim of the present paper is to develop an engineering methodology for the analytical estimation of the influence of residual stresses on the strength of double-side oxidized plates subjected to thermomechanical loading.

2. MATERIALS AND METHODS

2.1. Geometry of the Oxidized Plate

Consider a metal plate of initial thickness h_s^0. After oxidation of its surfaces, a symmetric composite structure is formed, consisting of a substrate of thickness h_s and two surface layers (films) of thickness h_f (Fig. 1). Hereinafter, all quantities pertaining to the substrate and the coating will be denoted by the indices 's' and 'f', respectively.

The following relations hold: $h_s = h_s^0 - 2(1-\alpha)h_f$, $h_s + 2h_f = h_s^0 + \alpha h_f$, where $\alpha = R_{PB} - 1$, and R_{PB} is the Pilling–Bedworth ratio [56, 57].

Let z be the transverse coordinate measured from the midsurface of the plate. Then, $H_s = \{z: |z| < h_s/2\}$ is the region occupied by the substrate, $H_f = \{z: h_s/2 < |z| < h_s/2 + h_f\}$ is the coating zone, $H = H_s + H_f = \{z: 0 \le |z| \le h_s/2 + h_f\}$ is the full cross-section.

2.2. Determination of Residual Stresses

We represent the total in-plane strain of the plate, which is nonhomogeneous through the thickness, as a superposition of the elastic strain $(1-\nu)\sigma/E$ and the generally incompatible strain ε^0 induced by fields of

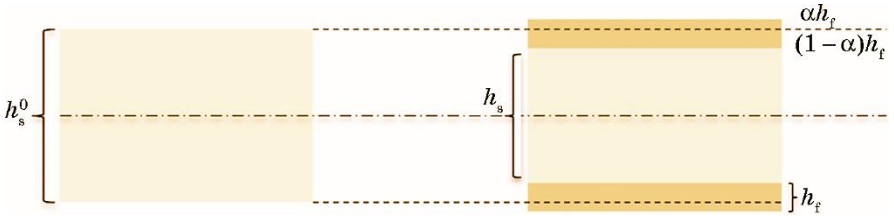


Fig. 1. Sketch of the cross-section of an oxidized plate.

nonmechanical nature: $\varepsilon = \dfrac{1-\nu}{E}\sigma + \varepsilon^0$.

For the stresses, we then obtain the expression

$$\sigma(z) = \frac{E(z)}{1-\nu(z)}(\varepsilon - \varepsilon^0(z)); \tag{1}$$

$E(z) = \begin{cases} E_f, z \in H_f, \\ E_s, z \in H_s \end{cases}$ is the Young's modulus and $\nu(z) = \begin{cases} \nu_f, z \in H_f, \\ \nu_s, z \in H_s \end{cases}$ is the Poisson's ratio of the material.

We require that the stresses have the status of residual stresses ($\sigma = \sigma_{res}$), that is, they must be self-equilibrated.

Then, taking into account formula (1) and the plane-sections' hypothesis, we obtain:

$$\varepsilon_{res}\int_H \frac{E(z)}{1-\nu(z)}dz - \int_H \frac{E(z)}{1-\nu(z)}\varepsilon^0(z)dz = 0, \tag{2}$$

and the residual stresses are expressed in terms of the incompatible strain:

$$\sigma_{res}(z) = \frac{E(z)}{1-\nu(z)}\left(\frac{\displaystyle\int_H \frac{E(z)}{1-\nu(z)}\varepsilon^0(z)dz}{\displaystyle\int_H \frac{E(z)}{1-\nu(z)}dz} - \varepsilon^0(z)\right). \tag{3}$$

In the case of oxidation of both surfaces, we have an even function

$$\varepsilon^0(z) = \begin{cases} \varepsilon_f^0, z \in H_f, \\ 0, z \in H_s. \end{cases} \tag{4}$$

By evaluating the integrals in formula (2), we find expressions for the residual stresses in terms of the incompatible strain of the oxidized surface layers:

$$\sigma_{res,f} = -\frac{\dfrac{E_s h_s}{1-\nu_s}}{\dfrac{E_s h_s}{1-\nu_s} + \dfrac{2E_f h_f}{1-\nu_f}}\frac{E_f}{1-\nu_f}\varepsilon_f^0, \quad \sigma_{res,s} = \frac{\dfrac{2E_f h_f}{1-\nu_f}}{\dfrac{E_s h_s}{1-\nu_s} + \dfrac{2E_f h_f}{1-\nu_f}}\frac{E_s}{1-\nu_s}\varepsilon_f^0. \tag{5}$$

Of course, these stresses are self-equilibrated:

$$\sigma_{res,s}h_s + 2\sigma_{res,f}h_f = 0. \tag{6}$$

In addition, the residual stresses in the plate may also be expressed

in terms of the residual strain. Specifically, using relations (2)–(4) and (6), we find:

$$\sigma_{\text{res, f}} = -\frac{E_{\text{s}}}{1-\nu_{\text{s}}}\frac{h_{\text{s}}}{2h_{\text{f}}}\varepsilon_{\text{res}},\ \sigma_{\text{res, s}} = \frac{E_{\text{s}}}{1-\nu_{\text{s}}}\varepsilon_{\text{res}}. \tag{7}$$

These formulas serve to determine the residual stresses from the experimentally measured ε_{res}.

2.3. Stress State under Thermomechanical Loading

Let an oxidized plate undergo biaxial tension by uniformly distributed line forces $N = \text{const}$, be heated to a constant temperature, $\Delta T = \text{const}$, and be in the field of residual stresses (5) (the same as Eq. (7)).

We determine the stress distribution in this piecewise-homogeneous plate. Integrating expression (1) and recalling the plane-sections' hypothesis, we obtain: $N = \varepsilon\int\limits_H \frac{E(z)}{1-\nu(z)}dz - \int\limits_H \frac{E(z)}{1-\nu(z)}\varepsilon^0(z)dz$. Hence,

$\varepsilon = \dfrac{N + \int\limits_H \frac{E(z)}{1-\nu(z)}\varepsilon^0(z)dz}{\int\limits_H \frac{E(z)}{1-\nu(z)})dz}$, and finally,

$$\sigma(z) = \frac{E(z)}{1-\nu(z)}\left(\frac{N + \int\limits_H \frac{E(z)}{1-\nu(z)}\varepsilon^0(z)dz}{\int\limits_H \frac{E(z)}{1-\nu(z)}dz} - \varepsilon^0(z)\right). \tag{8}$$

We take into account that now $\varepsilon^0(z) = \begin{cases}\varepsilon_{\text{f}}^0 + \alpha_{\text{f}}\Delta T,\ z \in H_{\text{f}},\\ \alpha_{\text{s}}\Delta T,\ z \in H_{\text{s}},\end{cases}$ where α_{s}, α_{f} are the coefficients of linear thermal expansion of the metal and its oxide. After evaluating all the integrals in formula (8), we find the stresses in the coatings and in the substrate:

$$\begin{aligned}\sigma_{\text{f}} &= \frac{E_{\text{f}}/(1-\nu_f)}{E_{\text{s}}h_{\text{s}}/(1-\nu_{\text{s}}) + 2E_{\text{f}}h_{\text{f}}/(1-\nu_{\text{f}})}\left(N + \frac{E_{\text{s}}h_{\text{s}}}{1-\nu_{\text{s}}}(\alpha_{\text{s}} - \alpha_{\text{f}})\Delta T\right) + \sigma_{\text{res, f}},\\ \sigma_{\text{s}} &= \frac{E_{\text{s}}/(1-\nu_{\text{s}})}{E_{\text{s}}h_{\text{s}}/(1-\nu_{\text{s}}) + 2E_{\text{f}}h_f/(1-\nu_{\text{f}})}\left(N - \frac{2E_{\text{f}}h_{\text{f}}}{1-\nu_{\text{f}}}(\alpha_{\text{s}} - \alpha_{\text{f}})\Delta T\right) + \sigma_{\text{res, s}}.\end{aligned} \tag{9}$$

This result demonstrates the influence of the mechanical load, heating, and residual stresses on the stress state of an oxidized plate of

symmetric structure.

2.4. Effect of Residual Stresses on Strength

We begin with an analysis for the uncoated plate ($h_f = 0$, $h_s = h_s^0$). In this case,

$$\sigma_s = N / h_s^0, \tag{10}$$

while thermal and residual stresses are absent.

From the strength condition

$$\sigma_s \le [\sigma]_s,$$

we find the allowable load for the unoxidized plate:

$$N \le N_c^0 = [\sigma]_s h_s^0. \tag{11}$$

This is the baseline result, with which all subsequent results will be compared.

We write the strength conditions for the inhomogeneous plate in terms of the allowable stresses for its components:

$$\sigma(z) \le [\sigma](z) = \begin{cases} [\sigma]_f, & z \in H_f, \\ [\sigma]_s, & z \in H_s. \end{cases} \tag{12}$$

Integrating inequality (12) through the thickness, we obtain the integral (global) limit equilibrium criterion:

$$N \le N_c^{\text{global}} = [\sigma]_s h_s + 2[\sigma]_f h_f, \tag{13}$$

which is independent of the self-equilibrated thermal components and residual phenomena.

We now consider the local situation.

The strength condition (12) requires the simultaneous fulfilment of the inequalities:

$$\begin{cases} \sigma_f \le [\sigma]_f, \\ \sigma_s \le [\sigma]_s. \end{cases} \tag{14}$$

Since the stresses σ_s, σ_f depend linearly on N, ΔT and on the residual stresses, set (14) is nothing other than a set of linear inequalities for the allowable loads and temperatures at a given level of residual stresses. Indeed, on the basis of result (9), conditions (14) can be rewritten in nondimensional form as follow:

$$\begin{cases} \dfrac{E_f/(1-\nu_f)}{E_s h_s/(1-\nu_s)+2E_f h_f/(1-\nu_f)}\,\dfrac{(N+E_s h_s(\alpha_s-\alpha_f)\Delta T/(1-\nu_s))}{[\sigma]_f-\sigma_{res,f}} \le 1, \\ \dfrac{E_s/(1-\nu_s)}{E_s h_s/(1-\nu_s)+2E_f h_f/(1-\nu_f)}\,\dfrac{(N-2E_f h_f(\alpha_s-\alpha_f)\Delta T/(1-\nu_f))}{[\sigma]_s-\sigma_{res,s}} \le 1. \end{cases} \tag{15}$$

For prescribed residual stresses, set (15) defines a region of safe thermomechanical loading on the plane $(N, \Delta T)$. In the general case, the simplex method must be employed to construct the solution of these inequalities. In analytical form, this is a cumbersome procedure. Therefore, we shall proceed differently. Taking into account that $\sigma_{res,\,s} = -2\sigma_{res,\,f} h_f/h_s$ (see Eq. (6)), we shall assume that $N = N(\Delta T, \sigma_{res,\,f})$. Then, from inequalities (15), we obtain the allowable load according to the local criterion in the form

$$N \le N_c^{local} = \min\left\{ \frac{-E_s h_s(\alpha_s-\alpha_f)\Delta T}{1-\nu_s} + \frac{\dfrac{E_s h_s}{1-\nu_s}+\dfrac{2E_f h_f}{1-\nu_f}}{\dfrac{E_f}{1-\nu_f}}([\sigma]_f-\sigma_{res,f}), \right.$$
$$\left. \frac{2E_f h_f}{1-\nu_f}(\alpha_s-\alpha_f)\Delta T + \frac{\dfrac{E_s h_s}{1-\nu_s}+\dfrac{2E_f h_f}{1-\nu_f}}{\dfrac{E_s}{1-\nu_s}}\left([\sigma]_s+\frac{2h_f}{h_s}\sigma_{res,f}\right) \right\}. \tag{16}$$

3. RESULTS AND DISCUSSION

3.1. Computational Examples

Detailed calculations using formulas (11), (13), and (16) were performed

TABLE 1. Physical and mechanical properties of the materials.

	Aluminium (6061-T6)	Aluminium oxide Al_2O_3	Titanium (Grade 2)	Titanium oxide TiO_2
h_s, h_f, mm	6	0.3	6	0.03
RPB	–	1.28	–	1.73
E_s, E_f, GPa	68.9	370	103	230
ν_s, ν_f	0.33	0.22	0.34	0.27
α_s, α_f, 10^{-6}, deg^{-1}	23.6	8.1	8.6	8.8
$[\sigma]_s$, $[\sigma]_f$, MPa	276	350	275	140

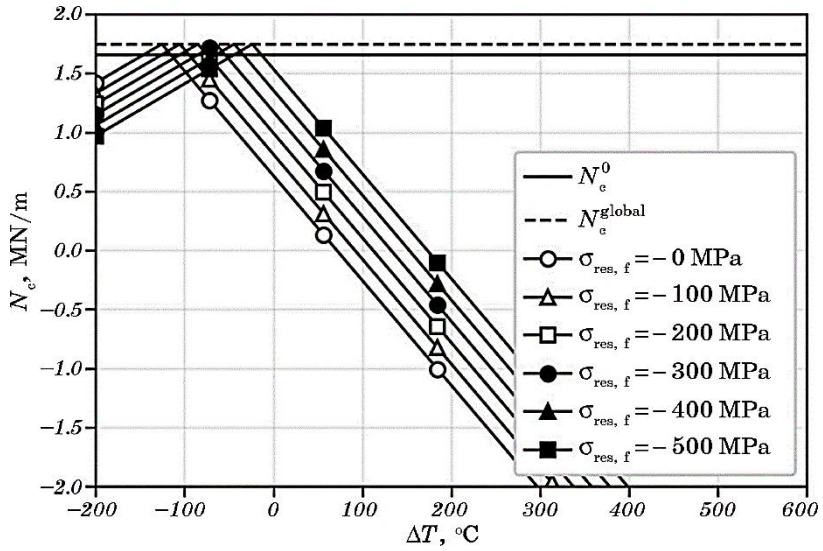


Fig. 2. Dependence of the allowable load on temperature at fixed levels of residual stress in the oxidized aluminium plate.

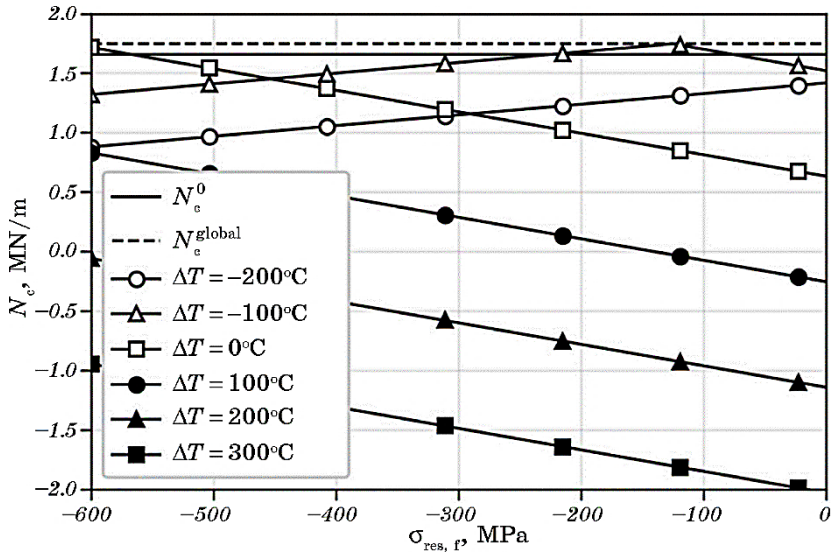


Fig. 3. Dependence of the allowable load on residual stress at fixed values of temperature in the oxidized aluminium plate.

for two materials, whose characteristics are listed in Table 1 [7, 58].

In Figs. 2, 3 and in Figs. 4, 5, the results of the computations of allowable loads for the oxidized aluminium-alloy plate and those for the

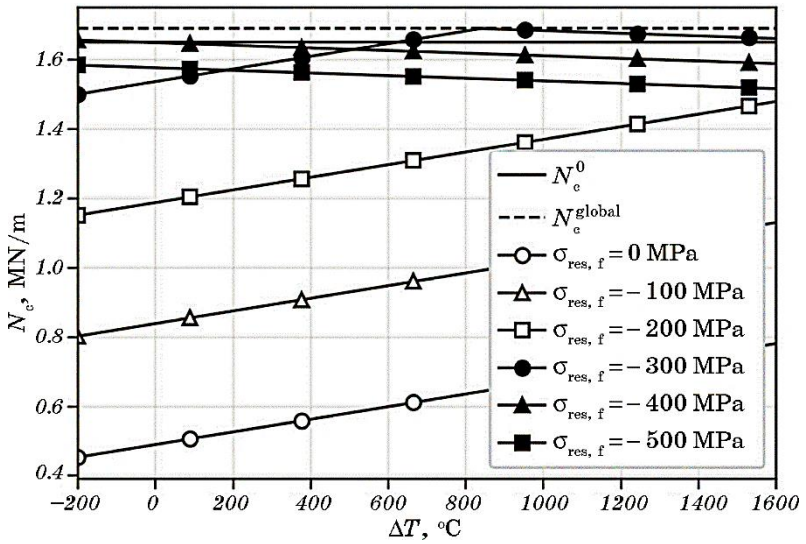


Fig. 4. Dependence of the allowable load on temperature at fixed levels of residual stress in the oxidized titanium plate.

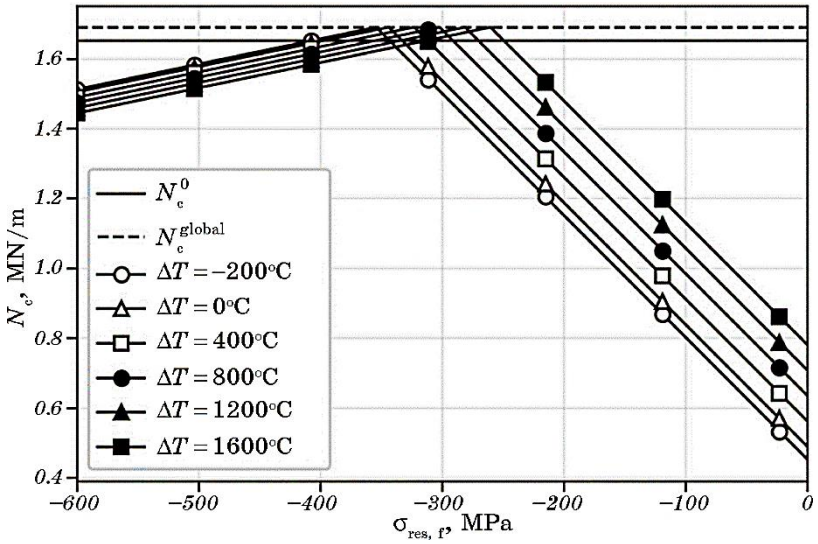


Fig. 5. Dependence of the allowable load on residual stress at fixed values of temperature in the oxidized titanium plate.

oxidized titanium plate are shown, respectively. All plots are compared with the horizontal line $N_c = N_c^0$ representing the allowable load for the uncoated plates.

3.2. Analysis of the Results

As is evident from the results presented, in the absence of thermal effects and residual stresses, the load-bearing capacity of the oxidized plates in tension is approximately three times lower than that of the uncoated plates: $N_c^{local} \approx N_c^0 / 3$. This occurs because of the high stress concentration in the thin, stiff coatings, which, owing to their limited strength, fail first.

In the presence of an additional temperature field and residual phenomena, the oxidized aluminium and titanium plates behave under loading in different ways.

Because the thermal expansion of the aluminium alloy is significantly greater than that of corundum, when the oxidized plate is heated, the coating cracks even in the absence of mechanical loading. In this case, an increase in the magnitude of the compressive residual stresses raises the allowable load at $\Delta T > -50$°C (Fig. 2). In the cryogenic temperature range, excessive compressive residual stresses in the coating are undesirable (Figs. 2 and 3), since, together with the mechanical load, they may cause additional tension and failure of the substrate.

The maximum allowable load is $N_c^{local} \approx N_c^{global}$ observed at a sub-zero temperature linked to the residual stress by the relation:

$$\Delta T = -\frac{1}{\alpha_s - \alpha_f}\left(\frac{[\sigma]_s + 2h_f\sigma_{res,f} / h_s}{E_s / (1-\nu_s)} - \frac{[\sigma]_f - \sigma_{res,f}}{E_f / (1-\nu_f)}\right).$$

In this case, the oxidized aluminium plate operates as an equal-strength structure.

By contrast, in the Ti–TiO_2 composition, the thermal strains of the coating and the substrate are practically compatible; therefore, the system responds well to high-temperature heating and, in the presence of substantial compressive residual stresses, can sustain external tensile loads not significantly lower than those tolerated by the unoxidized titanium plate (Figs. 4 and 5). The highest load-bearing capacity according to the local criterion is achieved at an optimal level of residual stress that depends on temperature:

$$\sigma_{res,f} = -\frac{\dfrac{1-\nu_s}{E_s}[\sigma]_s - \dfrac{1-\nu_f}{E_f}[\sigma]_f + (\alpha_s - \alpha_f)\Delta T}{\dfrac{1-\nu_s}{E_s}\dfrac{2h_f}{E_s h_s} + \dfrac{1-\nu_f}{E_f}}.$$

Finally, it should be noted that the proposed analysis does not aim to describe the mechanisms of delamination of composite structures along the interface.

4. CONCLUSION

Thus, a methodology has been developed for investigating the stress–strain state of metal plates strengthened by plasma electrolytic oxidation of the surface layer. The methodology makes it possible to construct analytical estimates of the load-bearing capacity of oxidized plates under tensile loading, accounting for the influence of the temperature field and self-equilibrated residual stresses. The capabilities of the methodology have been illustrated by computational examples for aluminium- and titanium-based compositions. Levels of residual stresses and temperatures have been identified, at which an oxidized plate operates as an equal-strength structure, providing the highest load-bearing capacity.

This contribution was created under the support of the National Research Foundation of Ukraine (project number NRFU 2023.04/0160, 0124U003748 'Development of technology for the formation of heat-resistant coatings by plasma electrolytic oxidation on parts of aviation and rocket and space technics').

AUTHORS' CONTRIBUTIONS

I.P.S. devised the principal conceptual framework, supervised the project, and verified the analytical approach. V.M.P. performed the analytical derivations, prepared the numerical computations, and drafted the manuscript with input from all authors. L.Ya.R. contributed to the methodology of evaluating residual stresses in oxide coatings produced by plasma electrolytic oxidation and reviewed the engineering applications. O.O.L. carried out the parametric calculations for the aluminium- and titanium-based compositions, prepared the figures, and assisted with the literature review. All authors discussed the results and approved the final version of the manuscript.

REFERENCES

1. O. Kozak, A. Velychkovych, and A. Andrusyak, *Eng.*, **6**, Iss. 10: 269 (2025).
2. E. I. Kryzhanivs'kyi, V. P. Rudko, and I. P. Shats'kyi, *Mater. Sci.*, **40**: 547 (2004).
3. L. Jeremić, B. Đorđević, S. Sedmak, A. Sedmak, M. Rakin, and M. Aranđelović, *Struct. Integr. Life*, **18**, No. 2: 99 (2018).
4. V. V. Kukhar, E. S. Klimov, and S. M. Chernenko, *Solid State Phenomena*, **316**: 873 (2021).
5. V. B. Tarelnyk, O. P. Gaponova, O. M. Myslyvchenko, and B. O. Sarzhanov, *Powder Metall. Met. Ceram.*, **59**: 76 (2020).
6. P. Prysyazhnyuk, M. Bembenek, I. Drach, A. Korzhov, L. Romanyshyn, and L. Ropyak, *Management Systems Production Eng.*, **32**, Iss. 2: 294 (2024).

7. A. L. Yerokhin, X. Nie, A. Leyland, A. Matthews, and S. J. Dowey, *Surf. Coat. Technol.*, **122**, Iss. 2–3: 73 (1999).
8. M. M. Student, I. B. Ivasenko, V. M. Posuvailo, H. H. Veselivs'ka, A. Y. Pokhmurs'kyi, Y. Y. Sirak, and V. M. Yus'kiv, *Mater. Sci.*, **54**: 899 (2019).
9. F. Simchen, M. Sieber, A. Kopp, and T. Lampke, *Coatings*, **10**, Iss. 7: 628 (2020).
10. L. Ropyak, T. Shihab, A. Velychkovych, V. Bilinskyi, V. Malinin, and M. Romaniv, *Ceramics*, **6**, Iss. 1: 146 (2023).
11. L. Ropyak, T. Shihab, A. Velychkovych, O. Dubei, T. Tutko, and V. Bilinskyi, *Progress in Physics of Metals*, **24**, No. 2: 319 (2023).
12. V. Korzhyk, V. Kopei, P. Stukhliak, O. Berdnikova, O. Kushnarova, O. Kolisnichenko, O. Totosko, D. Stukhliak, and L. Ropyak, *Materials*, **18**, Iss. 15: 3620 (2025).
13. M. M. Kundrat, *Int. Applied Mechanics*, **33**: 394 (1997).
14. Y. Y. Hu and W. M. Huang, *J. Appl. Phys.*, **96**: 4154 (2004).
15. O. S. Anishchenko, V. V. Kukhar, A. V. Grushko, I. V. Vishtak, A. H. Prysiazhnyi, and E. Y. Balalayeva, *Mater. Sci. Forum*, **945**: 531 (2019).
16. V. B. Kopei, O. R. Onysko, V. G. Panchuk, Z. M. Odosii, and Y. M. Kusyi, *J. Phys.: Conf. Ser.*, **2540**: 012033 (2023).
17. A. A. Bedzir, I. P. Shatskii, and V. M. Shopa, *Int. Applied Mechanics*, **31**: 351 (1995).
18. I. P. Shats'kyi, O. M. Lyskanych, and V. A. Kornuta, *Strength Mater.*, **48**: 469 (2016).
19. I. Shatskyi, I. Popadyuk, and A. Velychkovych, *Dynamical Systems in Applications* (Ed. J. Awrejcewicz) (Łódź–Cham: Springer: 2018), p. 343.
20. I. Shatskyi and V. Perepichka, *Dynamical Systems in Applications* (Ed. J. Awrejcewicz) (Łódź–Cham: Springer: 2018), p. 335.
21. R. V. Bondarenko, I. P. Shatskyi, Ya. V. Doroshenko, and A. S. Velychkovych, *J. Achiev. Mater. Manuf. Eng.*, **132**, Nos. 1–2: 13 (2025).
22. J. Dean, T. Gu, and T. W. Clyne, *Surf. Coat. Technol.*, **269**: 47 (2015).
23. D. Shen, J. Cai, C. Guo, G. Li, D. He, and Q. Yang, *Chin. J. Mech. Eng.*, **26**: 1149 (2013).
24. R. H. U. Khan, A. L. Yerokhin, T. Pilkington, A. Leyland, and A. Matthews, *Surf. Coat. Technol.*, **200**, Iss. 5–6: 1580 (2005).
25. M. Aliofkhazraei, D. D. Macdonald, E. Matykina, E. V. Parfenov, V. S. Egorkin, J. A. Curran, S. C. Troughton, S. L. Sinebryukhov, S. V. Gnedenkov, T. Lampke, F. Simchen, and H. F. Nabavi, *Appl. Surf. Sci. Adv.*, **5**: 100121 (2021).
26. J. A. Curran and T. W. Clyne, *Surf. Coat. Technol.*, **199**, Iss. 2–3: 168 (2005).
27. D. Wojtas, M. Marciszko-Wiąckowska, and Ł. Maj, *Prog. Surf. Sci.*, **100**, Iss. 3: 100780 (2025).
28. J. Zhang, W. Dai, X. Wang, Y. Wang, H. Yue, Q. Li, X. Yang, and C. Guo, *J. Mater. Res. Technol.*, **25**: 4554 (2023).
29. A. Maytorena-Sánchez, J. Hernández-Torres, F. López-Huerta, M. A. Hernández-Campos, L. Zamora-Peredo, M. Pacio-Castillo, L. E. Serrano-De la Rosa, and L. García-González, *Mater. Lett.*, **282**: 128679 (2021).
30. C. H. Hsueh, *Thin Solid Films*, **418**, Iss. 2: 182 (2002).
31. C. H. Hsueh, *J. Appl. Phys.*, **91**, Iss. 12: 9652 (2002).

32. C. H. Hsueh and A. G. Evans, *J. Am. Ceram. Soc.*, **68**, Iss. 5: 241 (1985).
33. G. C. A. M. Janssen, M. M. Abdalla, F. van Keulen, B. R. Pul, and J. G. C. de Ree, *Thin Solid Films*, **517**, Iss. 6: 1858 (2009).
34. L. B. Freund and S. Suresh, *Thin Film Materials: Stress, Defect Formation and Surface Evolution* (Cambridge: Cambridge University Press: 2003).
35. Y. C. Tsui and T. W. Clyne, *Thin Solid Films*, **306**, Iss. 1: 23 (1997).
36. N. Dolgov, L. Vinogradov, I. Blumbergs, and R. Chatys, *Fatigue and Fracture of Materials and Structures* (Eds. G. Lesiuk, S. Duda, J. A. F. O. Correia, and A. M. P. De Jesus) (Cham: Springer: 2022), p. 9.
37. R. Kulchytsky-Zhyhailo, S. J. Matysiak, and A. S. Bajkowski, *J. Therm. Stresses*, **41**, Iss. 9: 1169 (2018).
38. V. A. Shevchuk, *J. Math. Sci.*, **278**: 780 (2024).
39. B. M. Kalynyak and V. A. Shevchuk, *Mater. Sci.*, **61**: 110 (2025).
40. S. A. G. Oliveira and A. F. Bower, *Wear*, **198**, Iss. 1–2: 15 (1996).
41. I. Shatskyi, M. Makoviichuk, L. Ropyak, and A. Velychkovych, *Ceramics*, **6**, Iss. 3: 1879 (2023).
42. I. Shatskyi, M. Makoviichuk, and L. Ropyak, *Proc. Struct. Integr.*, **59**: 407 (2024).
43. L. Ropyak, I. Shatskyi, M. Makoviichuk, and I. Lazariev, *Proc. Struct. Integr.*, **72**: 20 (2025).
44. I. Shatskyi, M. Makoviichuk, I. Lazariev, and L. Ropyak, *Struct. Integr. Life*, **25**, No. 3: 399 (2025).
45. J. W. Hutchinson and Z. Suo, *Adv. Appl. Mech.*, **29**: 63 (1992).
46. Z. C. Xia and J. W. Hutchinson, *J. Mech. Phys. Solids*, **48**, Iss. 6–7: 1107 (2000).
47. H. H. Yu and J. W. Hutchinson, *Int. J. Fracture*, **113**: 39 (2002).
48. A. G. Evans, D. R. Mumm, J. W. Hutchinson, G. H. Meier, and F. S. Pettit, *Prog. Mater. Sci.*, **46**, Iss. 5: 505 (2001).
49. I. P. Shatskyi, M. V. Makoviichuk, and A. B. Shcherbii, *Mater. Sci.*, **55**: 484 (2020).
50. I. Shatskyi and V. Petrashchuk, *Proc. Struct. Integr.*, **81**: 129 (2026).
51. I. Shatskyi, M. Makoviichuk, R. Bondarenko, and Ya. Doroshenko, *Proc. Struct. Integr.*, **81**: 240 (2026).
52. M. D. Thouless, *J. Vac. Sci. Technol. A*, **9**, Iss. 4: 2510 (1991).
53. I. P. Shatskii, *Sov. Mater. Sci.*, **25**: 160 (1989).
54. I. P. Shats'kyi and V. V. Perepichka, *Mater. Sci.*, **40**: 240 (2004).
55. I. P. Shats'kyi and M. V. Makoviichuk, *Mater. Sci.*, **41**: 486 (2005).
56. N. B. Pilling and R. E. Bedworth, *J. Inst. Met.*, **29**: 529 (1923).
57. C. Xu and W. Gao, *Mater. Res. Innov.*, **3**: 231 (2000).
58. M. Shokouhfar, C. Dehghanian, and A. Baradaran, *Appl. Surf. Sci.*, **257**, Iss. 7: 2617 (2011).

Metallophysics and Advanced Technologies
Металофіз. новітні технол.
Metallofiz. Noveishie Tekhnol.
2026, vol. 48, No. 9, pp. 963–972
https://doi.org/10.15407/mfint.48.09.0963
Reprints available directly from the publisher

© 2026 G. V. Kurdyumov Institute for Metal Physics,
National Academy of Sciences of Ukraine
Published by license under
the G. V. Kurdyumov Institute for Metal Physics–
N.A.S. of Ukraine Publishers imprint.
Printed in Ukraine.

PACS numbers: 61.72.Ff, 62.20.Qp, 62.23.Pq, 68.37.Hk, 81.20.Ev, 81.40.Jj, 81.70.Bt

Synthesis and Characterization of a Ti_3SiC_2–TiC–$TiSi_2$ Composite for High-Temperature Applications

I. M. Kirian[*], A. M. Lakhnik[*], M. A. Skoryk[*], S. O. Kotrechko[*], O. V. Zatsarna[*], T. O. Monastyrska[*], I. V. Gurin[**], and O. D. Rud[*]

[*]*G. V. Kurdyumov Institute for Metal Physics, N.A.S. of Ukraine, 36 Academician Vernadsky Blvd., UA-03142 Kyiv, Ukraine*
[**]*Institute of Solid State Physics, Materials Science and Technologies, NSC 'KIPT', 1 Akademichna Str., UA-61108 Kharkiv, Ukraine*

The influence of sintering conditions (pressure and holding time) on the structure and mechanical properties of Ti–Si–C-system composites is investigated. A formation of the Ti_3SiC_2, TiC, and $TiSi_2$ phases in the composite is confirmed by XRD analysis. Structural parameters of individual phases and mechanical characteristics of the obtained composites are determined. As found, samples S2 and S3 have superior compressive strength (σ_u) of 1445 MPa and 1460 MPa, respectively. At the same time, sample S3 demonstrates the highest hardness of ≅ 10.5 GPa (1072 *HV*), significantly outperforming the values obtained for S1 (≅ 6.7 GPa, 689 *HV*) and S2 (≅ 6.5 GPa, 677 *HV*).

Key words: Ti_3SiC_2, MAX phase, composite, XRD.

Досліджено вплив умов спікання (тиску та часу витримки) на структуру та механічні властивості композитів системи Ti–Si–C. Утворення фаз Ti_3SiC_2, TiC і $TiSi_2$ у композиті підтверджено за допомогою рентґеноструктурної аналізи. Визначено структурні параметри окремих фаз і механічні характеристики одержаних композитів. Виявлено, що зразки S2 і S3 ма-

Corresponding author: Oleksandr Rud
E-mail: rud@imp.kiev.ua

Citation: I. M. Kirian, A. M. Lakhnik, M. A. Skoryk, S. O. Kotrechko, O. V. Zatsarna, T. O. Monastyrska, I. V. Gurin, and O. D. Rud, Synthesis and Characterization of a Ti_3SiC_2–TiC–$TiSi_2$ Composite for High-Temperature Applications, *Metallofiz. Noveishie Tekhnol.*, **48**, No. 9: 963–972 (2026), DOI: 10.15407/mfint.48.09.0963

© Publisher PH 'Akademperiodyka' of the NAS of Ukraine, 2026. This is an open access article under the CC BY-ND license (https://creativecommons.org/licenses/by-nd/4.0)

ють вищу міцність на стиснення (σ_u) у 1445 МПа і 1460 МПа відповідно. Водночас, зразок S3 демонструє найвищу твердість у ≅ 10,5 ГПа (1072 *HV*), що значно перевершує значення, одержані для S1 (≅ 6,7 ГПа, 689 *HV*) і S2 (≅ 6,5 ГПа, 677 *HV*).

Ключові слова: Ti_3SiC_2, MAX-фаза, композит, рентґеноструктурна аналіза.

(Received 23 January, 2026; in final version, 23 July, 2026)

1. INTRODUCTION

Modern industry requires the creation of materials that are highly resistant to extreme conditions, such as high temperatures, aggressive environments, and significant mechanical loads. Therefore, researchers have recently focused on creating composite materials that will satisfy these conditions. Composites containing MAX phases open up new possibilities in the development of such materials. Ternary compounds with a layered hexagonal structure, known as MAX phases can meet these requirements and become excellent substitutes for high-temperature metals and ceramics. These materials are described by the generally accepted formula $M_{n+1}AX_n$ ($n = 1, 2, 3$), where M is a transition metal, A is the elements of the A-subgroup of the Mendeleev table and X = C or N [1–4]. The MAX phase of Ti_3SiC_2 has attracted practical interest for industrial applications. This phase has good physical and mechanical properties that meet the requirements of modern materials science. The Ti_3SiC_2 phase is characterized by high electrical ($4.5 \cdot 10^6$ $\Omega^{-1} \cdot m^{-1}$) and thermal conductivities (40–43 W/mK), low density ($\rho = 4.52$ g/cm^3), high Young's modulus ($E = 320$–343 GPa), flexural strength ≅ 260 MPa and compressive strength ≅ 580 MPa [5–8]. The melting point is ≅ 3000°C [4]. Further, the Ti_3SiC_2 MAX phase is characterized by a relatively insignificant coefficient of thermal expansion ≅ $9.1 \cdot 10^{-6}$ K^{-1} [9]. In addition, the Ti_3SiC_2 MAX phase is easily machinable and resistant to high-temperature oxidation. In works [10, 11], it is reported that the oxidation resistance of the MAX phase of Ti_3SiC_2 is maintained up to a temperature of ≅ 1000 °C. During the oxidation process of the MAX phase of Ti_3SiC_2, the formation of two oxide layers is observed. The outer layer contains anatase-type TiO_2. Increasing the oxidation duration leads to forming an inner layer containing two oxides, TiO_2 and SiO_2. One of the significant disadvantages among the mechanical properties of the MAX phase of Ti_3SiC_2 is its relatively low hardness, which is of ≅ 4 GPa (*HV*) [4]. This relatively modest hardness restricts its applicability in industry fields requiring high resistance to surface deformation or wear.

One of the promising approaches to solving this problem is the creation of composite materials based on MAX phases or with their content. Adding hard binary compounds (TiC or SiC) to the MAX phase

increases the hardness of the material. At the same time, the layered structure of MAX phases can provide composite materials with a high modulus of elasticity. All this makes MAX phases promising for many applications. An additional factor that positively affects the properties of composites is the introduction of $TiSi_2$ compounds into their composition. This additive helps increase the oxidation stability of the MAX phase of Ti_3SiC_2, which is important for applications in high temperatures and aggressive environments. Combining different phases in composites allows achieving an optimal balance between hardness, ductility, oxidation resistance, and other performance characteristics. Such composites are extremely promising for use in modern technologies that require materials with high mechanical and chemical properties.

The main purpose of this work was to study the influence of the phase composition and microstructure features on the mechanical properties of Ti_3SiC_2–TiC–$TiSi_2$ composites obtained by sintering the initial powder mixtures Ti–Si–C system. Special attention was paid to the relationship between the parameters of the sintering process and the evolution of the microstructure of composite materials.

2. MATERIALS AND METHODS

To synthesize Ti_3SiC_2–TiC–$TiSi_2$ composites, Ti (99.7%, $\cong$ 70 μm), Si (99.8%, $\cong$ 100 μm), and crystalline spectrally pure graphite (99.99% C, $\cong$ 50 μm) were used as starting materials. The powders were purchased from the commercial company 'GrandLada' (Kyiv, Ukraine). The initial powders of Ti, Si, and graphite were mixed in an atomic ratio of 3:1.1:2, respectively. Then, the mixture was homogenized on a laboratory planetary mill (Retsch PM100) at room temperature for 1 hour in a steel container. For mixing, 15 steel balls with a diameter of 10 mm were used. The rotational speed of the grinding container was of 200 rpm, and the balls-to-powder mass ratio was 20:1.

The homogenized powder mixtures were placed in a graphite mould with an internal diameter of 14 mm. The inner part of the mould and punch were separated from the sample with graphite foil. This prevented the sample from sintering with the mould parts at high temperatures. The all composite were sintered in an inert Ar atmosphere in a high-temperature furnace with an automated heating system developed at the G. V. Kurdyumov Institute for Metal Physics of the N.A.S. of Ukraine. Three types of samples were synthesized. The conditions for obtaining them are given in Table 1.

The x-ray diffraction (XRD) patterns were recorded using a powder diffractometer (DRON-4) in the Bragg–Brentano geometry with monochromatized MoK_α radiation (wavelength $\lambda = 0.71069$ Å). The x-ray diffraction patterns were processed by the Rietveld refinement tech-

TABLE 1. The sintering modes of the studied samples.

Sample	Sintering temperature, °C	Heating/cooling rate, K/min	Pressure, MPa	Holding time, min
S1	1385	50/150	60	30
S2*	1385	50/150	60	30 + 60
S3	1385	40/150	90	60

* The sample was synthesized by a two-stage sintering technique: holding at a temperature of 1385°C for 30 minutes and then cooling. Then, it was heated again and held at the same temperature for 60 minutes.

nique using the MAUD software [12]. Scanning electron microscopy (SEM) studies of the sintered composite were performed on a VEGA3 TESCAN microscope. Uniaxial compression tests were performed on an Instron 8802 universal servohydraulic testing machine. The hardness measurement was done using a Vickers indentation device on the polished surface of the composite sample with a load of 5000 g.

3. RESULTS AND DISCUSSION

Three samples were obtained for the study according to the conditions specified in Table 1. The synthesis of all samples took place at a temperature of 1385°C, with only the pressure and holding time at a given temperature change. Before the study, the samples were polished. The XRD phase identification of the sintered samples is shown in Fig. 1.

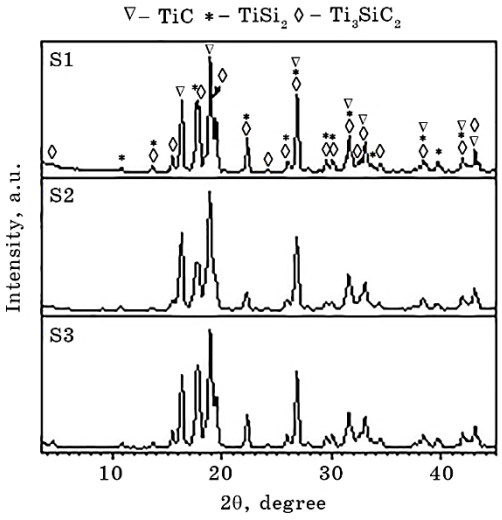


Fig. 1. Typical XRD patterns of the synthesized samples.

It is established that all synthesized samples mainly consist of three phases. The identified peaks are attributed for h.c.p. Ti_3SiC_2 (MAX phase), f.c.c. TiC, and orthorhombic $TiSi_2$ phases. The proportion of each phase in the sample was determined using Rietveld refinement. The result of the full-profile analysis is presented in Table 2. The sample S1 sintered at a pressure of 60 MPa with a holding time of 30 min contains approximately 25 wt.% Ti_3SiC_2 MAX phase, 41 wt.% TiC, and 34 wt.% $TiSi_2$.

The process of obtaining the sample S2 consisted of two stages of heat treatment. At the first stage, the sample was heated to a temperature of 1385°C and subjected to sintering under a pressure of 60 MPa for 30 minutes, which contributed to the initial formation of the phase composition. After completing this stage, the sample was quickly cooled to room temperature, which allowed it to reduce residual thermal stresses and stabilize its phase composition typical of sample S1. The first stage of obtaining S3 corresponds to the conditions for the synthesis of sample S1. In the second stage, the material was re-sintered at a similar pressure (60 MPa), but with an extension of the holding time to 60 minutes, which provided additional diffusion activity between the components and improved structural density. X-ray diffraction analysis revealed that the phase composition of sample S2 is similar to that of sample S1 (see Table 2). The absence of newly formed phases indicates the thermodynamic stability of the initial components under given conditions.

An increase in the sintering load to 90 MPa and the holding time to 60 min did not result in any changes to the phase composition of the sample (S3). X-ray phase analysis confirmed the preservation of the same crystalline phases as at lower sintering parameters. The content of each phase in S3 is comparable to samples S1 and S2. This indicates that with a further increase in load or holding time, the probability of

TABLE 2. Crystallographic parameters, phase percentage, and crystallite sizes acquired by Rietveld fitting from the XRD patterns of sintered samples.

Sample	Phase	Lattice parameters (Å)			Crystallite sizes (Å)	Abundance (wt.%)
		a	*b*	*c*		
S1	Ti_3SiC_2	3.065	–	17.677	570	25
	TiC	4.318	–	–	640	41
	$TiSi_2$	8.281	4.803	8.557	730	34
S2	Ti_3SiC_2	3.065	–	17.673	540	27
	TiC	4.317	–	–	730	40
	$TiSi_2$	8.279	4.803	8.557	820	33
S3	Ti_3SiC_2	3.064	–	17.664	480	24
	TiC	4.315	–	–	650	42
	$TiSi_2$	8.284	4.802	8.557	620	34

phase transformations remains minimal.

For all studied samples, the lattice parameters and crystallite size for each phase were calculated (Table 2). The results showed that the values of the lattice parameters for all samples remain practically identical, indicating the stability of the crystal structure when the synthesis conditions change. However, slight differences were found in the crystallite sizes, which may indicate some influence of different sintering parameters on the microstructure of the material. This may indicate an inhomogeneous phase distribution or the presence of defects in the material. The results obtained suggest that, although the lattice parameters are similar, the sintering conditions have an impact on the crystallite size, which, in turn, may influence the mechanical properties of the samples.

Figure 2 illustrates the SEM electron images in back-scattering electrons (BSE) mode taken from polished surface cross-section composites sintering at different conditions. SEM images demonstrate the heterogeneous structure of the material, consisting of dark and light areas. This indicates the presence of several phases with different chemical compositions in the composite.

A detailed microstructural analysis of the composites is shown in (Fig. 3). The MAX phase of Ti_3SiC_2 is represented by individual grains with a lamellar morphology, which can positively affect the mechanical plasticity of the material. The TiS_{i2} phase forms light gray intermetallic inclusions of rounded (sample S1, S2) or dendritic (sample S3) shape. According to the results of x-ray diffraction analysis, about 40 wt.% of the composite consists of titanium carbide (TiC). Thus, based on XRD data and microstructural studies, it was established that the composites formed by titanium carbide matrix with uniformly distributed inclusions of Ti_3SiC_2 and $TiSi_2$.

Energy dispersive x-ray spectral analysis (EDS) was used to perform a detailed analysis of the microstructure of the Ti_3SiC_2–TiC–$TiSi_2$

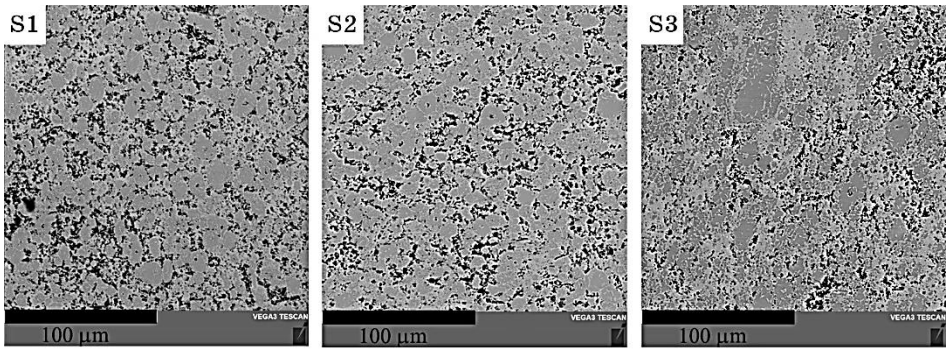


Fig. 2. Microstructure of bulk composite materials obtained after sintering.

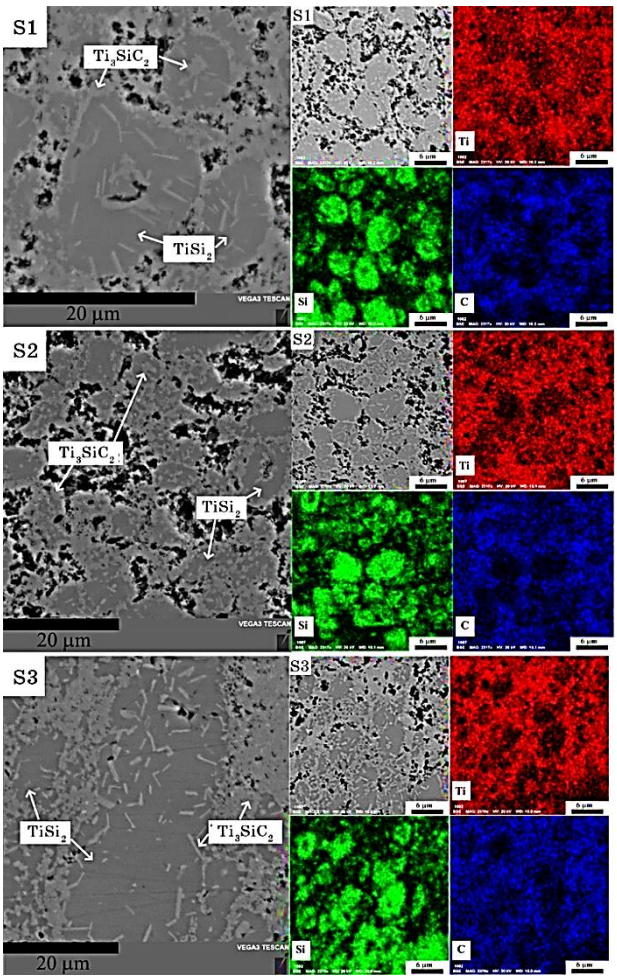


Fig. 3. Typical SEM micrographs of composite and element distribution maps.

composite and determine the distribution of its elemental composition. The use of EDS helps to identify possible inhomogeneities in the distribution of elements that may affect the performance characteristics of the composite. It is clear, the titanium and carbon are uniformly distributed over cross section of the sample.

The distribution of titanium on the elemental maps correlates with all three phases, while silicon is concentrated in the regions of the Ti_3SiC_2 and $TiSi_2$ phases. Carbon, as can be seen from its map, is mainly localized in TiC and in small amounts in areas typical of the Ti_3SiC_2 MAX phase. In the region responsible for the $TiSi_2$ phase, carbon is not observed. The overlap of the map areas with the most pronounced carbon and titanium concentrations indicates the dominant role of TiC in

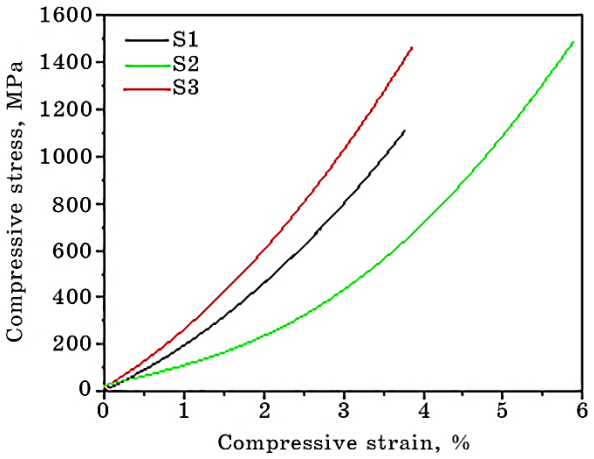


Fig. 4. Compressive stress–strain curves of synthesized composites.

the material structure. It is correlates well with the results of x-ray structure analysis. This microstructure provides an optimal combination of mechanical and thermal properties, which makes the material promising for applications in extreme operating conditions.

The effect of sample synthesis conditions on their mechanical properties was determined based on the results of uniaxial compression tests. The samples were brittle fractured without signs of macroplastic plastic deformation (Fig. 4). The values of compressive strength (σ_u) were determined and are given in Table 3. All samples contain a three-phase structure of Ti_3SiC_2, $TiSi_2$, and TiC significantly affecting their mechanical characteristics.

Sample S1 synthesized at a pressure of 60 MPa for 30 minutes demonstrate a compressive strength (σ_u) of 1096 MPa. Compared to other samples, this material has the lowest strength value. Relatively low strength values may be due to the insufficient duration of the sintering process, which did not ensure the full formation of interfacial bonds and led to residual porosity. In the case of sample S2, a two-stage sintering process, including initial heating at 60 MPa for 30 minutes, subsequent cooling, and repeated heating with a holding time of 60 minutes, contributes to the improvement of the mechanical properties of the material. For sample S2, the value σ_u is of 1460 MPa. The in-

TABLE 3. The mechanical properties of the studied samples.

Sample	Compressive strength (σ_u), MPa	Hardness, *HV*/GPa
S1	1096	689/6.7
S2	1460	677/6.5
S3	1445	1072/10.5

crease in the value σ_u may be because rapid cooling after the first heating stage contributed to the relaxation of residual stresses that arose during sintering. Reheating ensured improved diffusion processes, reduced the concentration of structural defects, and the formation of a more homogeneous microstructure, which together led to improved performance characteristics of the material. Sample S3 sintered at an elevated pressure of 90 MPa for 60 minutes demonstrated value of compressive strength $\sigma_u = 1445$ MPa.

Vickers hardness values measured on the sintered samples are presented in Table 3. The obtained data for compressive strength demonstrate increased mechanical properties for samples S2 and S3. However, in contrast, sample S3 exhibits a higher hardness value of $\cong 10.5$ GPa (1072 *HV*) compared to S1 and S2 manifesting $\cong 6.7$ GPa (689 *HV*) and 6.5 GPa (677 *HV*), respectively.

4. CONCLUSIONS

The composites of the Ti_3SiC_2–TiC–$TiSi_2$ were synthesized by sintering the initial powder mixtures Ti–Si–C system. The relationship between the parameters of the sintering process and the mechanical properties of composite materials was studied. Relatively low strength values of sample S1 ($\sigma_u = 1096$ MPa) may be due to the insufficient duration of the sintering process, which did not ensure the full formation of interfacial bonds and led to residual porosity. As a result, this led to relatively low mechanical-property values. In contrast, sample S2 demonstrated the best combination of strength and hardness ($\sigma_u = 1460$ MPa, hardness $\cong 6.5$ GPa). This improvement is attributed to the two-stage sintering process, where initial heating and cooling helped relax residual stresses, while re-sintering enhanced diffusion processes, reduced structural defects, and promoted a more homogeneous microstructure. It was found that sample S3 has a higher hardness ($\cong 10.5$ GPa) compared to S1 and S2 due to the increased sintering pressure (90 MPa). These factors contributed to increased densification of the composite and enhanced interaction between the matrix and the constituent phases.

ACKNOWLEDGEMENT

This work was partially supported by the project No. 056/26 of the G. V. Kurdyumov Institute for Metal Physics of the N.A.S. of Ukraine.

AUTHORS' CONTRIBUTIONS

I.M.K.: conceptualization, x-ray investigation, writing review and

editing; A.M.L.: SPS sintering, writing review and editing; M.A.S.: electron-microscopy studies, formal analysis; S.O.K.: mechanical testing, formal analysis; O.V.Z.: mechanical testing, formal analysis; T.O.M.: electron-microscopy studies, formal analysis; I.V.G.: preparation of samples for mechanical tests; O.D.R.: conceptualization, supervision, writing review and editing.

REFERENCES

1. I. M. Low, *Advances in Science and Technology of $M_{n+1}AX_n$ Phases* (Woodhead Publishing: 2012).
2. M. Naguib, M. Kurtoglu, V. Presser, J. Lu, J. Niu, M. Heon, L. Hultman, Y. Gogotsi, and M. W. Barsoum, *Adv. Mater.*, **23**: 4248 (2011).
3. M. Sokol, V. Natu, S. Kota, and M. W. Barsoum, *Trends. Chem.*, **1**: 210 (2019).
4. S. Haji Amiri, and N. Pourmohammadie Vafa, *Synthesis and Sintering*, **1**, No. 4: 216 (2021).
5. T. Chen, P. M. Green, J. L. Jordan, J. M. Hampikian, and N. N. Thadhani, *Metall. Mater. Trans. A.*, **33**: 1737 (2002).
6. M. W. Barsoum and T. El-Raghy, *Adv. Mater. Proc.*, **7**: 51 (1997).
7. E. Tabares, A. Jiménez-Morales, and S. A. Tsipas, *Bol. Soc. Esp. Ceram. Vidr.*, **60**, Iss. 1: 41 (2021).
8. L. Silvestroni, C. Melandri, and J. Gonzalez-Julian, *J. Eur. Ceram. Soc.*, **41**, Iss. 12: 6064 (2021).
9. S.-B. Li, L.-T. Zhang, and L.-F. Cheng, *Mater. Sci. Technol.*, **18**, Iss. 12: 1494 (2002).
10. S. Li, L. Cheng, and L. Zhang, *Mater. Sci. Eng. A.*, **341**, Iss. 1–2: 112 (2003).
11. S. L. Yang, Z. M, Sun, H. Hashimoto, Y. H. Park, and T. Abe, *Oxid. Met.*, **59**: 155 (2003).
12. L. Luterotti and S. Gialanella, *Acta Mater.*, **46**, Iss. 1: 101 (1998).

Metallophysics and Advanced Technologies
Металофіз. новітні технол.
Metallofiz. Noveishie Tekhnol.
2026, vol. 48, No. 9, pp. 973–983
https://doi.org/10.15407/mfint.48.09.0973
Reprints available directly from the publisher

© 2026 G. V. Kurdyumov Institute for Metal Physics,
National Academy of Sciences of Ukraine
Published by license under
the G. V. Kurdyumov Institute for Metal Physics–
N.A.S. of Ukraine Publishers imprint.
Printed in Ukraine.

PACS numbers: 61.66.Dk, 68.37.Hk, 81.05.Bx, 81.20.Ev, 81.30.Hd, 81.40.Cd, 81.70.Pg

Mechanism of *in situ* WC Formation during Mechanical Alloying of the Medium-Entropy $W_{1.5}$FeCoNi Alloy

S. Yu. Teslia[*], O. I. Yurkova[*], D. S. Leonov[**], and P. I. Loboda[*]

[*]*National Technical University of Ukraine*
'Igor Sikorsky Kyiv Polytechnic Institute',
37, Beresteiskyi Ave., UA-03056 Kyiv, Ukraine
[**]*Technical Center, N.A.S. of Ukraine,*
13, Pokrovs'ka Str., UA-04070 Kyiv, Ukraine [1]

Mechanical alloying in a high-carbon medium (petroleum) is used to fabricate a $W_{1.5}$FeCoNi medium-entropy alloy (MEA) *in situ* reinforced by tungsten carbide (WC). During high-energy ball milling of a mixture of elemental metal powders (W, Fe, Co and Ni) for 20 hours, a b.c.c. solid solution and dispersed WC particles with a grain size from 0.5 μm to 1 μm are formed. The carbide-phase formation involves the decomposition of petrol, the generation of carbon radicals, and a subsequent reaction with tungsten that leads to the formation of WC by both direct reaction with W particles and diffusion into the b.c.c. lattice. XRD and SEM analyses reveal gradual alloying, crystallite refinement, and homogenization of a b.c.c. solid-solution matrix. DSC measurements show two endothermic peaks at 885°C and 1040°C, corresponding to short-range ordering, sintering of the powder, secondary WC precipitation, and randomization of a solid solution with possible b.c.c.–f.c.c. transformations. The *in situ* carbide reinforcement and uniform microstructure are expected to enhance significantly the mechanical properties and thermal stability of the MEA, demonstrating the feasibility of this approach for high-performance carbide-strengthened alloys.

Key words: high-entropy materials, mechanical alloying, tungsten carbide.

Corresponding authors: Serhii Yuriyovych Teslia
E-mail: teslia.serhii@lll.kpi.ua

Citation: S. Yu. Teslia, O. I. Yurkova, D. S. Leonov, and P. I. Loboda, Mechanism of *in situ* WC Formation during Mechanical Alloying of the Medium-Entropy $W_{1.5}$FeCoNi Alloy, *Metallofiz. Noveishie Tekhnol.*, 48, No. 9: 973–983 (2026), DOI: 10.15407/mfint.48.09.0973

© Publisher PH 'Akademperiodyka' of the NAS of Ukraine, 2026. This is an open access article under the CC BY-ND license (https://creativecommons.org/licenses/by-nd/4.0)

Методу механічного леґування у висококарбоновому середовищі (бензині) було використано для одержання стопу середньої ентропії (MEA) складу $W_{1.5}FeCoNi$, зміцненого карбідом Вольфраму (WC) безпосередньо в процесі синтези (*in situ*). Під час високоенергетичного кульового помелу суміші елементних металевих порошків (W, Fe, Co і Ni) упродовж 20 годин утворилися твердий розчин із ОЦК-структурою та дисперсні частинки WC із розміром зерен від 0,5 до 1 мкм. Процес утворення карбідної фази включає розкладання бензину, ґенерацію вуглецевих радикалів і подальшу реакцію з вольфрамом, що приводить до формування WC, як шляхом безпосередньої взаємодії з частинками W, так і внаслідок дифузії в ОЦК-ґратницю. Методи рентґенофазової аналізи (XRD) та сканувальної електронної мікроскопії (SEM) виявили поступове леґування, подрібнення кристалітів і гомогенізацію матриці твердого розчину з ОЦК-структурою. Результати диференційної сканувальної калориметрії (DSC) показали наявність двох ендотермічних піків при 885°C і 1040°C, що відповідають процесам близького впорядкування, спікання порошку, вторинного виділення WC і розупорядкування твердого розчину з можливими фазовими перетвореннями типу ОЦК–ГЦК. Очікується, що зміцнення карбідами (*in situ*) та формування однорідної мікроструктури значно поліпшать механічні властивості та термічну стабільність цього стопу, що підтверджує доцільність застосування такого підходу для створення високоефективних стопів, зміцнених карбідами.

Ключові слова: високоентропійні матеріяли, механічне леґування, карбід Вольфраму.

(Received 14 September, 2026; in final version, 18 September, 2026)

1. INTRODUCTION

High-entropy alloys (HEAs) represent a novel class of metallic materials that exhibit an exceptional balance of high hardness and strength, along with sufficient ductility and outstanding resistance to wear, corrosion, and oxidation [1–3]. Due to their high configurational entropy, HEAs typically form single, two-phase, or multiphase solid solutions rather than intermetallic compounds. This distinctive characteristic opens new opportunities for the application of these alloys in many fields, particularly in environments with high temperatures [4, 5]. The extraordinary properties of HEAs are provided for their application as a binder in metal–ceramic composites strengthened with refractory compounds [6–9]. The concept of strengthening high-entropy alloys through the formation of composite structures can be realized either *ex situ*, by adding ceramic reinforcements (oxides, borides, carbides) [7, 8, 10], or *in situ*, during thermal ageing [11] or through chemical reactions with non-metallic doping such as B [12, 13], [14], C [15, 16], N [17, 18], and O [19, 20]. Bharat Gwalani *et al.* [21] found that *ex situ* adding of 3 vol.% Y_2O_3 to $Al_{0.3}CoCrFeMnNi$ resulted in a

significant increase in compressive yield strength from 979 MPa to 1759 MPa. In the study [22], the effect of the amount of SiC) on phase composition and mechanical properties of f.c.c. CoCrFeNi was shown. Incorporation of SiC particles led not only to a substantial increase in the yield strength but also to the preservation of considerable ductility. The HEA composite with 6 wt.% SiC reached yield strength of ≅ 1200 MPa, over eight times which of the base alloy (200 MPa), while maintaining an elongation of 37%. Compared to *ex situ* methods, the *in situ* formation of reinforcing phases is preferable because it ensures a cleaner interface and stronger bonding between the matrix and the formed phase, leading to improved mechanical and thermal properties. It is well known that the appropriate addition of interstitial elements with small atomic radii in traditional alloys, such as steels and superalloys, is beneficial to their structure and properties. The interstitial atoms cause evident lattice distortion in HEAs, which affects significantly the interaction between dislocations and other crystal defects and in addition, if the solubility of non-metal atoms in the HEA matrix is exceeded, carbides, nitrides, borides can form, which will lead to greater microstructure refinement (and dispersion strengthening of alloys [23–26]. Among known refractory compounds, tungsten carbide is one of the most promising strengthening phases, because it combines high hardness and thermal stability with good chemical resistance, providing effective strengthened of the matrix even at high temperatures and in aggressive environments [27].

In this study, we proposed a new method to fabricate *in situ* carbide-strengthened $W_{1.5}$FeCoNi medium-entropy alloy (MEA) by mechanical alloying in a high-carbon medium (petrol). The use of iron-group metals for MEA preparation is due to the low solubility of carbon, low price, and solid-solution stabilization.

2. MATERIALS AND METHODS

The initial powders were commercially available, which was W (2–6 μm, > 99.95% purity, Vimaterial), Fe (ASC100.29, 20–45 μm, > 99.91% purity, Höganäs), Co (2–4 μm, > 99.8% purity, ChemPur), Ni (2–4 μm, > 99.7% purity ChemPur). A portion of powder was placed in the cemented carbide jar and mechanically alloyed (MA) at a speed of 400 rpm/min for duration of 20 h. To prevent the oxidation of powders during high-energy milling, high-purity argon was introduced into the ball mill jar. The ball-to-powder mass ratio was 10:1. Petrol was used as a carbon source to form *in situ* WC-carbide particles and as a processing controlling agent to avoid excessive cold welding. The evolution of phase composition and powder microstructure was investigated after 1, 2, 10, 15 and 20 h of MA. The structure and phase transformations were investigated by x-ray diffractometer Ultima IV (Rigaku

Corp., Tokyo, Japan) at 30 kV and 15/20 mA in the range $2\theta = 20–90°$. Structural parameters were refined by the Rietveld method using the PDXL software. A scanning electron microscope (SEM) Axia ChemiSEM LoVac was used to obtain basic information concerning microstructure of the powder particles. The chemical composition of the alloy was determined, using energy dispersive x-ray (EDX) microanalysis in a SEM equipped with an energy-dispersive detector TrueSight X. Differential scanning calorimeter (DSC, DSC PT 1600 — Linseis, Germany) was used to analyse the thermal stability of $W_{1.5}FeCoNi$ alloy under flowing argon atmosphere. The scanning ranges were 25–1250°C at a heating rate of 10°C/min in the Al_2O_3 crucible.

3. RESULTS AND DISCUSSION

The XRD results (Fig. 1, *a*) indicate that the b.c.c. solid solution and WC phase and were formed after 20 h of MA. At the initial stage of MA, after 1–2 h, a clear broadening and a significant decrease in the

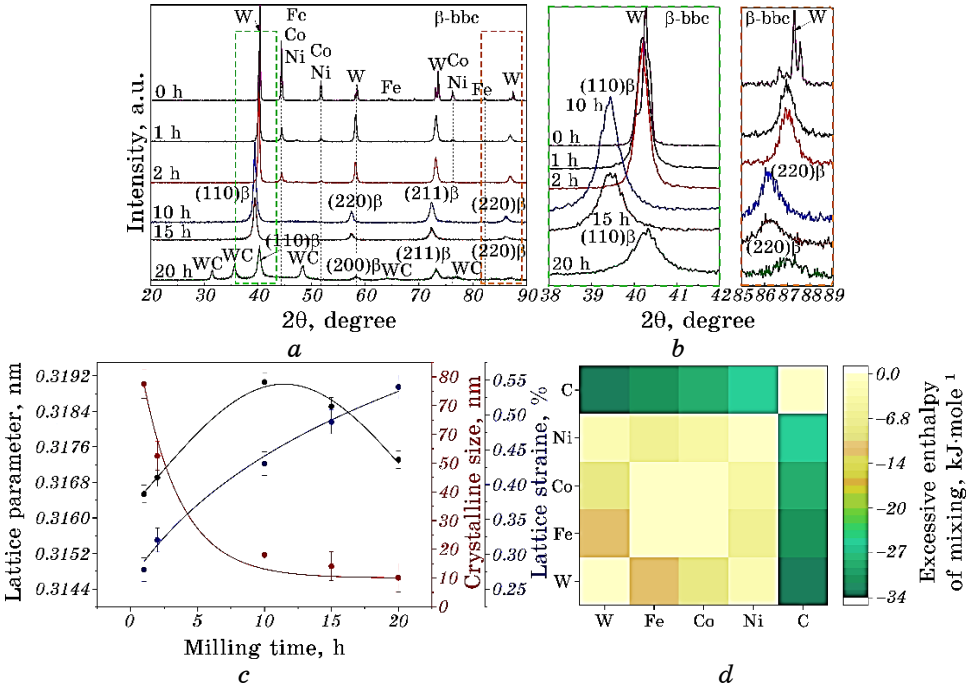


Fig. 1. XRD patterns of $W_{1.5}FeCoNi$ ball-milled powder *vs.* milling time (*a*), (*b*). (*c*) Lattice parameter, crystallite size and lattice strain of W-based b.c.c. solid solution of milled $W_{1.5}FeCoNi$ powders. (*d*) Excessive binary enthalpies of mixing estimated using Miedema's model [28–30].

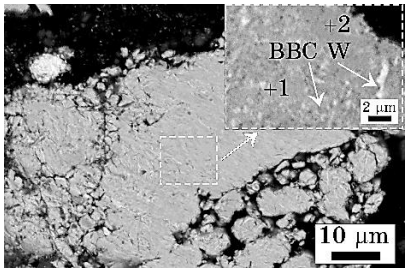
intensity of the diffraction peaks, can be observed (Fig. 1, *b*), which is associated with an increase in microstress level and refinement of the structure of powder particles (Fig. 1, *c*). The decrease in diffraction intensity and the disappearance of some diffraction peaks of Co, Ni, and Fe with the simultaneous slight shift of W peaks towards smaller 2θ angles due to the increase in lattice parameters (Fig. 1, *c*) can be considered as the beginning of alloying, dissolution of components, and the formation of solid solution. It should be noted that the dissolution of Fe, Co, and Ni atoms, which radii are smaller than that of W atom, should cause a decrease in the lattice parameter and a shift of peaks to larger angles. Yet, since the opposite is observed, it can be assumed that the dissolution of carbon atoms occurs and causes a slight increase in the lattice parameter of W.

Increasing the MA time to 10 h promotes the obtaining of b.c.c. solid solution. The positions of the β-phase peaks are close to those of W (Fig. 1, *a*, *b*), which suggests that the b.c.c. solid solution is formed, apparently, based on W crystal lattice. A significant shift of the β-phase peaks towards smaller 2θ angles and an increase in the lattice parameter due to the dissolution of carbon atoms are observed.

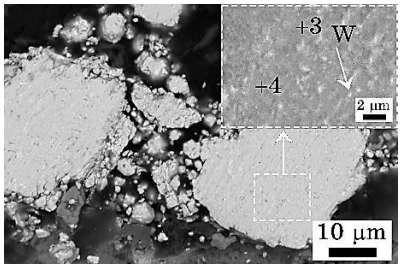
Further increase in MA time to 15 h does not change the phase composition of the alloy, but change the lattice parameter of b.c.c. solid solution. Compared to the previous MA stage, the lattice parameter decreased from 0.319 nm to 0.3184 nm (Fig. 1, *c*), which may be due to the beginning of the interaction of carbon atoms with tungsten. The significant decrement of diffraction intensity and peak broadening are observed (Fig. 1, *a*, *b*).

After 20 h of MA, significant changes are observed in the x-ray diffraction spectrum (Fig. 1, *a*). In addition to the reflections of the b.c.c. solid solution (β-phase), the diffraction lines corresponding to tungsten carbide are observed. This indicates that the MA process results in the *in situ* formation of WC phase which content in the alloy is 28.7 wt.%. The lattice parameter of b.c.c. solid solution decreases to 0.3169 nm, which is related to its depletion on W and C atoms owing to *in situ* formation of WC (Fig. 1, *c*). According to the binary enthalpy of mixing [28–30], W exhibits the most negative ΔH_{mix} values (Fig. 1, *d*) with carbon (–34 kJ·mol^{-1}), indicating the strongest chemical affinity and the highest tendency to form carbides. In contrast, the Fe–Co–Ni subsystem shows relatively small negative enthalpies of mixing, suggesting good mutual solubility and the formation of a homogeneous solid solution.

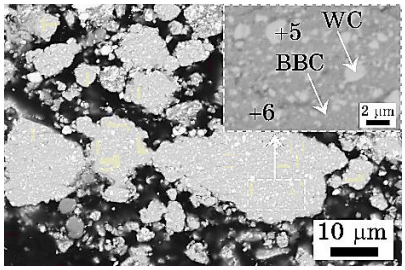
The SEM image of the ground and polisher powder surface is shown in Fig. 2. After 10 h of MA, the $W_{1.5}$FeCoNi alloy consists of a b.c.c. solid solution and the W particles (Fig. 2, *a*, *e*, points 1–2). Tungsten has one of the largest atomic radii in the W–Fe–Co–Ni system (139 pm) and the highest melting point; due to this, its dissolution can take



a



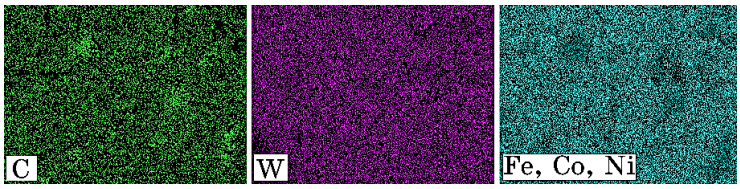
b



c

Points	Atomic, %					
	Fe	Co	Ni	W	C	O
1	1.1	3.2	2.5	77.7	5.4	10.1
2	20.0	20.5	20.1	35.5	1.5	2.4
3	18.5	22.4	22.1	36.1	0.2	0.7
4	3.4	6.0	5.4	73.6	3.2	8.4
5	0.5	0.8	0.2	48.4	50.0	0.1
6	16.7	22.2	21.8	38.0	0.5	0.8

e



d

Fig. 2. SEM image of cross-section of $W_{1.5}FeCoNi$ powder after mechanical allying at: (*a*) 10 h, (*b*) 15 h, (*c*) 20 h with (*d*) elemental mapping analysis for the *in situ* reacted $W_{1.5}FeCoNi$ + C and local point analysis for different alloying time (*e*).

the longest time. Increasing MA time to 15 h promotes homogenization of the microstructure and a decrease of quantity the amount and size of W particles. At final stage of MA (20 h), the powder microstructure consists of b.c.c. solid solution and WC particles (Fig. 2, *c*–*e*) with an average size of 0.75 μm.

During MA process, carbon atoms contained in the petrol were dissolved in the metal powder mixture, which resulting in a high carbon concentration in $W_{1.5}FeCoNi$ alloy. The carbides were formed by W interacting with the carbon in the petrol after long-time high-energy ball milling. A similar observation of carbide formation was reported, when fabricating the AlFeMgTiZn [31] and MoNbTaW [25] alloys by ball milling, and the carbides were formed due to the presence of stearic acid as processing controlling agent.

Based on the XRD patterns (Fig. 1) and SEM images (Fig. 2) of MA powder, the mechanism of WC formation was suggested (Fig. 3). The initial portion of powder on Stage 1 (near 1–2 hours of MA) undergoes dynamic solid-state interaction processes under high local deformation and heating. At this stage, in addition to grinding and reducing the average size of crystallites (Fig. 1, *c*), the processes of cold welding and overlapping of powder particles occur [32]. During MA, the organic components of petrol undergo gradual decomposition due to the intense mechanical energy input. In the initial 1–5 hours of milling, gasoline largely retains its molecular structure, with minimal bond breakage. At Stage 2 (MA, 10 h), the powder alloy, in addition to b.c.c. phase, contains non-reacted W particles. The organic component can homolytically cleave C–C and C–H bonds, generating free radicals and small-unsaturated hydrocarbons such as alkenes [33]. The transformation in petrol associated with the intensive mechanical impact during MA, especially by the high-energy collisions between milling media and powder particles, creates localized extreme conditions (high pressure, shear stress, and transient temperature spikes), which are sufficient to break chemical bonds [34]. Under these conditions, some part of carbon can be dissolved in the b.c.c. lattice. At Stage 3 (MA, 15 h), the final phase of breaking the C–C bonds and the formation of graphite nanolayers in the form of coke may occur.

Since during mechanical alloying W particles can remain in a dispersed state in the matrix of the b.c.c. solid solution, the *in situ* formation of WC at Stage 4 can have two paths. First way, it is a reaction of carbon with a W-based b.c.c. solid solution. The C diffuses into the b.c.c. lattice and reacts with W, forming dispersed WC particles (less

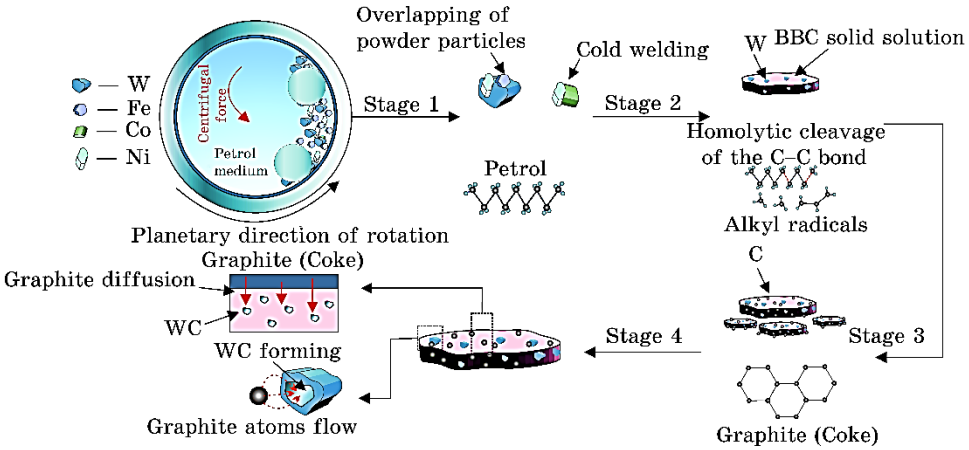


Fig. 3. The mechanism of WC *in situ* formation during mechanical alloying of $W_{1.5}$FeCoNi in the petrol medium.

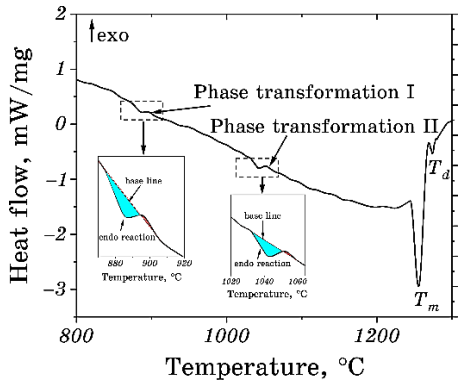


Fig. 4. DSC curves of 20 h mechanically alloyed $W_{1.5}$FeCoNi alloy.

than 0.5 μm in size). Second, it is the direct reaction between carbon and the residual W. In this way, the particle size of WC is of around 1 μm.

In order to investigate the phase transformations and melting point of $W_{1.5}$FeCoNi alloy, DSC analysis was carried out, and the results are presented in Fig. 4. During heating, two pairs of endothermic (885°C and 1040°C) peaks were indicated. At 885°C, the endothermic reaction is associated with a short-range ordering effect [35], sintering of alloy powder during heating, and secondary WC precipitation by carbon dissolution from the b.c.c. lattice. The next endothermic effect started at 1028°C indicates the randomization of the solid solution, segregation and particular b.c.c.–f.c.c. transformation. The b.c.c. lattice has more open structure; the elements, especially with small atomic radii diffused more easily as compared to f.c.c. structure [36]. The melting point of the $W_{1.5}$FeCoNi alloy is of 1250°C. Increasing the temperature promotes the thermal degradation of MEH (T_d point, Fig. 4), because the melt reacts with the crucible and the moisture in argon.

4. CONCLUSIONS

In summary, an *in situ* WC-reinforced $W_{1.5}$FeCoNi medium-entropy alloy was successfully fabricated by mechanical alloying in a high-carbon (petrol) medium. The process led to the formation of a b.c.c. solid solution matrix and dispersed WC particles, with particle sizes ranging from 0.5 to 1 μm. The WC formation occurs *via* two mechanisms: diffusion of carbon into the b.c.c. lattice and reaction with residual W atoms. XRD and SEM analyses confirmed progressive alloying, crystallite refinement and homogenization of the structure over 20 h of milling. DSC analysis revealed two endothermic peaks at 885°C and 1040°C, attributed to short-range atomic ordering, powder sinter-

ing, secondary WC precipitation, and randomization of the solid solution including partial b.c.c.–f.c.c. transformations. The study demonstrates that high-energy mechanical alloying in a carbon-rich environment is an effective strategy to produce MEAs multicomponent alloys with *in situ* carbide reinforcement, offering potential for improved mechanical properties and high-temperature performance.

ACKNOWLEDGMENTS

This work was supported by the National Research Foundation of Ukraine (project No. 2023.03/0053, Agreement No. 197.03/0053).

AUTHOR CONTRIBUTIONS

Teslia S. Yu.: conceptualization of the study, development of the methodology, conducting the research, analysis and interpretation of the results, preparation of the initial manuscript draft, and data visualization; Yurkova O. I.: conducting the research, data processing and systematization, validation of the results, preparation of the initial manuscript draft, editing and revision of the text; Leonov D. S.: preparation of the manuscript, editing of the manuscript; Loboda P. I.: conducting the research, organization of the study, and scientific supervision of the research. All authors approved the final version of the manuscript.

REFERENCES

1. Jien-Wei Yeh, S.-K. Chen, Su-Jien Lin, Jon-Yiew Gan, Tsung-Shune Chin, Tian Shun, C.-H. Tsau, and S. Y. Chang, *Adv Eng Mater*, **6**, No. 5: 299 (2004).
2. Modupeola Dada, Patricia Popoola, and Ntombi Mathe, *World Journal of Engineering*, **20**, Iss. 1: 43 (2023).
3. Daniel B. Miracle, Ming-Hung Tsai, Oleg N. Senkov, Vishal Soni, and Rajarshi Banerjee, *Scr Mater*, **187**: 445 (2020).
4. Yiping Lu, Yong Dong, Sheng Guo, Li Jiang, Huijun Kang, Tongmin Wang, Bin Wen, Zhijun Wang, Jinchuan Jie, Zhiqiang Cao, Haihui Ruan, and Tingju Li, *Scientific Reports*, 4, Article No. 6200 (2014).
5. George J. Wise, Nicole L. Church, Hon Tong Pang, Robert P. Thompson, Howard J. Stone, and Nicholas G. Jones, *Adv. Eng. Mater*, **27**, Iss. 9: 2402330 (2025).
6. Ping'an Zang, Zhaoqiang Chen, Mingdong Yi, Hui Chen, Kun Dong, Jingjie Zhang, Guangchun Xiao, Xianglong Meng, and Chonghai Xu, *Ceramics International*, **51**, Iss. 12, Part A: 16234 (2025).
7. Zijian Wang, Fei Xing, Guojian Xu, Weijun Liu, and Hongyou Bian, *Mater Today Commun*, **49**: 113991 (2025).
8. Yunfei Cheng, Chaohui Wang, Meiling Dong, Yuan You, Weidong Cheng,

Wanjun Xie, Zhenwei Wang, Liang Wang, Xiaodong Zhang, and You Wang, *Intermetallics (Barking)*, **187**: 109003 (2025).
9. Muhammed Muneer S, Arun B. S, Renjish Vijay, Aju Kumar V. N, Anand Sekhar R, *Results in Surfaces and Interfaces*, **20**: 100622 (2025).
10. J. G. Lopes, A. Candeias, P. Agrawal, J. Shen, N. Schell, R. S. Mishra, and J. P. Oliveira, *J. Alloys Compd.*, **995**: 174694 (2024).
11. Yu Yin, Yitian Zhao, Kai En Koey, Qiyang Tan, Ming-Xing Zhang, and Han Huang, *Composites Part B: Engineering*, **235**: 109795 (2022).
12. Hui Liang, Jingzhuo Zhang, Jinxin Hou, Jingchang Sun, Jianhong Liu, Jiawen Liu, Xu Han, Jiani Tan, Li Jiang, Xiaocong Li, and Zhiqiang Cao, *Journal of Materials Research and Technology*, **38**: 1014 (2025).
13. Lijun Wang, Lulu Guo, Huicong Chen, Chenwei Shao, Zhaoying Ding, Hyun Suk Choi, Maxx Yao, and Yu Zou, *Intermetallics (Barking)*, **186**: 108964 (2025).
14. Xinggang Wang, Meng Sun, Jiaxin Liu, Xueqing Liu, Weibin Jiang, Xianping Wang, and Qianfeng Fang, *Crystals*, **14**, Iss. 12: 1029 (2024).
15. L. Chmielak, L. Mujica Roncery, P. Niederhofer, S. Weber, and W. Theisen, *SN Applied Sciences*, **3**: Article No. 835 (2021).
16. Tuanwei Zhang, Renlong Xiong, Jae Wung Bae, Peyman Asghari-Rad, Soung Yeoul Ahn, Huabei Peng, Zhihua Wang, and Hyoung Seop Kim, *Journal of Alloys and Compounds*, **1003**: 175698 (2024).
17. Yang Lan, Yong Zhang, Yingbo Peng, Andong Wang, Yuan Gao, Wenfei Yang, Weijie Fan, Wei Zhang, and Yong Liu, *Journal of Alloys and Compounds*, **990**: 174400 (2024).
18. Mateusz Włoczewski, Kinga Jasiewicz, Piotr Jenczyk, Elżbieta Gadalińska, Krzysztof Kulikowski, Yong Zhang, Rui Xuan Li, and Dariusz M. Jarząbek, *Metallurgical and Materials Transactions A*, **56**: 2040 (2025).
19. Tinghui Cao, Yake Wu, Jin Tian, Feng Jiang, and Jun Sun, *Scr. Mater.*, **215**: 114692 (2022).
20. Jie Lu, Ying Chen, Ling Li, Han Zhang, Xiancheng Zhang, and Xiaofeng Zhao, *Composites Part B: Engineering*, **265**: 110933 (2023).
21. Bharat Gwalani, Rizaldy M. Pohan, Junho Lee, Bin Lee, Rajarshi Banerjee, Ho Jin Ryu, and Soon Hyung Hong, *Scientific Reports*, **8**: Article No. 14085 (2018).
22. M. Adil Mehmood, Khurram Shehzad, M. Mujahid, Talha Bin Yaqub, Andy Godfrey, Filipe Fernandes, F. Z. Muhammad, and Khurram Yaqoob, *Scientific Reports*, **12**: Article No. 21486 (2022).
23. M. Y. He, Y. F. Shen, N. Jia, and P. K. Liaw, *Appl Mater Today*, **25**: 101162 (2021).
24. Yemao Lu, Andrey Mazilkin, Torben Boll, Nikita Stepanov, Sergei Zherebtzov, Gennady Salishchev, Éva Ódor, Tamas Ungar, Enrique Lavernia, Horst Hahn, and Yulia Ivanisenko, *Materialia*, **16**: 101059 (2021).
25. Congyan Zhang, Uttam Bhandari, Jialin Lei, Congyuan Zeng, Shengmin Guo, Hyunjoo Choi, Seungjin Nam, Jinyuan Yan, Shizhong Yang, and Feng Gao, *Crystals*, **11**, Iss. 9: 1073 (2021).
26. Zhufeng He, Nan Jia, Haile Yan, Yongfeng Shen, Mingwei Zhu, Xianjun Guan, Xiaoli Zhao, Shenbao Jin, Gang Sha, Yuntian Zhu, and Chain T. Liu, *International Journal of Plasticity*, **139**: 102965 (2021).
27. Meiyan Feng, Tianxiang Lin, Guofu Lian, Changrong Chen, and Xu Huang,

Ceram. Int., **50**, Iss. 24, Part C: 55286 (2024).
28. Lihui Tian, Ming Fu, and Wei Xiong, *Materials*, **11**, Iss. 2: 320 (2018).
29. Long Wu, Aimin Wang, and Wenhao Xing, *Metals (Basel)*, **13**, Iss. 5: 987 (2023).
30. Te-Kang Tsao and An-Chou Yeh, *Materials Transactions*, **56**, Iss. 11: 1905 (2015).
31. Vincent H. Hammond, Mark A. Atwater, Kristopher A. Darling, Hoang Q. Nguyen and Laszlo J. Kecskes, *JOM*, **66**: 2021 (2014).
32. L. Lü and M. O. Lai, *Mechanical Alloying* (New York: Springer: 1998).
33. Nida Tasneem, Shakeel Ahmed, and Mohammad M. Hossain, *Arabian Journal for Science and Engineering*, **50**: 3649 (2024).
34. Challapalli Suryanarayana, *Research*, **2019**: Article ID 4219812 (2019).
35. Angelo F. Andreoli, Andrea Fantin, Sergey Kasatikov, Vinícius P. Bacurau, Michael Widom, Piter Gargarella, Eric M. Mazzer, Thomas G. Woodcock, Kornelius Nielsch, and Francisco G. Coury, *Materials & Design*, **238**, Article No. 112724 (2024).
36. Marek Zajusz, Monika Jawańska, Juliusz Dąbrowa, Katarzyna Berent, Grzegorz Cieślak, Tadeusz Kulik, and Krzysztof Mroczka, *Mater. Res. Lett.*, **10**: No. 8: 556 (2022).

Metallophysics and Advanced Technologies
Металофіз. новітні технол.
Metallofiz. Noveishie Tekhnol.
2026, vol. 48, No. 9, pp. 985–998
https://doi.org/10.15407/mfint.48.09.0985
Reprints available directly from the publisher

© 2026 G. V. Kurdyumov Institute for Metal Physics,
National Academy of Sciences of Ukraine
Published by license under
the G. V. Kurdyumov Institute for Metal Physics–
N.A.S. of Ukraine Publishers imprint.
Printed in Ukraine.

PACS numbers: 68.37.Hk, 68.47.Gh, 81.05.Ni, 81.40.Cd, 81.65.Kn, 81.65.Rv, 82.45.Bb

Characteristic Features of the Selective Dissolution of the NZ30K Magnesium Alloy in Ringer–Locke Solution

V. L. Greshta[*], O. E. Narivskyi[**], A. V. Dzhus[*]

[*]*National University Zaporizhzhia Polytechnic,*
64 Zhukovskogo Str.,
UA-69063 Zaporizhzhia, Ukraine
[**]*Ukrspetsmash LLC,*
7 Haharina Str.,
UA-71100 Berdiansk, Ukraine

The paper investigates the characteristic features of the selective dissolution of the magnesium alloy NZ30K in the Ringer–Locke solution. As found, it is subjected to pitting corrosion. Metallographic analysis using a scanning electron microscopy reveals that the pitting surface has a developed relief characteristic of selective dissolution of steels and alloys. The characteristic features of the selective dissolution of alloy components in pitting are studied using the calculated coefficients of selective dissolution of zinc Z_{Zn}, zirconium Z_{Zr}, and neodymium Z_{Nd}. As believed, if these coefficients are less than one, then, the main component of the alloy, magnesium, dissolves more intensively than a specific alloying element in combination with magnesium. And, if the coefficients $Z_{Zn,\ Zr,\ Nd} > 1$, then, it is *vice versa*. As found, the intensity of selective metal dissolution on the side surface of the pitting increases in the following sequence: Zr, Mg, Nd, Zn; Zr, Nd, Mg, Zn or Mg, Zr, Nd, Zn. Under such conditions, the pitting surface is enriched with zirconium or magnesium and depleted in Mg, Nd, Zn or Zr, Nd, Zn. This contributes to the solid-phase diffusion of zirconium atoms into the alloy bulk, and magnesium, neodymium, and zinc in the opposite direction in the first case, and magnesium atoms into the alloy bulk, and Zr, Nd, and Zn in the opposite direction in the second case. As shown, the processes of solid-phase diffusion of alloy

Corresponding author: Viktor Greshta
E-mail: greshtaviktor@gmail.com

Citation: V. L. Greshta, O. E. Narivskyi, and A. V. Dzhus, Characteristic Features of the Selective Dissolution of the NZ30K Magnesium Alloy in Ringer–Locke Solution, *Metallofiz. Noveishie Tekhnol.*, **48**, No. 9: 985–998 (2026), DOI: 10.15407/mfint.48.09.0985

© Publisher PH 'Akademperiodyka' of the NAS of Ukraine, 2026. This is an open access article under the CC BY-ND license (https://creativecommons.org/licenses/by-nd/4.0)

components supports the anodic dissolution of metals in pitting, which is provided by cathodic reactions of oxygen reduction in their vicinity and hydrogen on their surface, which is formed as a result of hydration of corrosion products. As found, under such conditions, the magnesium content on the side surface of the NZ30K alloy decreases from 95.67 down to 71.84…82.57 wt.%, and it is covered with a passive film with an oxygen content from 10.02 up to 17.18 wt.%. As found, at the bottom of the pitting, the intensity of selective metal dissolution increases in the following sequence: Mg, Zn, Nd, Zr. Under such conditions, the surface of the pitting is enriched with magnesium and depleted in Zn, Nd, and Zr. This contributes to the solid-phase diffusion of magnesium atoms into the alloy bulk, and Zn, Nd, and Zr to the pitting surface. This supports the anodic processes, which are provided by cathodic hydrogen reduction reactions on their surface. As found, the oxygen content on the pitting surface decreases down to 1.92…7.8 wt.%. This shows that the passive film is denser on the side surface of the pitting than on its bottom. As proved, the pittings on the surface of the NZ30K alloy are repassivated, and, therefore, it can be considered as a material for the production of biodegradable implants.

Key words: pitting corrosion, NZ30K alloy, Ringer–Locke solution, selective dissolution of metals in NZ30K alloy pittings, biodegradable NZ30K alloy implant.

В статті досліджували характерні особливості селективного розчинення маґнійового стопу NZ30K у розчині Рінґера–Локка. Встановлено, що він піддався піттінґовій корозії. Металографічною аналізою із застосуванням растрового електронного мікроскопу встановлено, що поверхня піттінґів мала розвинутий мікрорельєф, притаманний селективному розчиненню криць і стопів. Характерні особливості селективного розчинення компонентів стопу в піттінґах досліджували, використовуючи розраховані коефіцієнти селективного розчинення цинку Z_{Zn}, цирконію Z_{Zr} і неодиму Z_{Nd}. Вважали, що, якщо ці коефіцієнти менші за одиницю, то основний компонент стопу Маґній інтенсивніше розчинявся, ніж конкретний леґувальний елемент в парі з Маґнієм. А якщо коефіцієнти $Z_{Zn,\ Zr,\ Nd} > 1$, то навпаки. Встановлено, що на бічній поверхні піттінґа інтенсивність селективного розчинення металів зростала у такій послідовності: Zr, Mg, Nd, Zn; Zr, Nd, Mg, Zn або Mg, Zr, Nd, Zn. За таких умов поверхня піттінґа збагачувалася Цирконієм або Маґнієм і збіднювалася Mg, Nd, Zn або Zr, Nd, Zn. Це сприяло твердофазній дифузії атомів Цирконію в об’єм стопу, а Маґнію, Неодиму та Цинку — в протилежному напрямку у першому випадку, та атомів Маґнію в об’єм стопу, а Zr, Nd і Zn — в протилежному напрямку в другому. Показано, що процеси твердофазної дифузії компонентів стопу підтримували анодне розчинення металів у піттінґах, яке забезпечувалося катодними реакціям відновлення Оксиґену в їхньому околі та Гідроґену на їхній поверхні, який утворювався внаслідок гідратації продуктів корозії. З’ясовано, що за таких умов вміст Маґнію на бічній поверхні стопу NZ30K понизився з 95,67 до 71,84...82,57 мас.%, і вона покрилася пасивною плівкою з вмістом Оксиґену від 10,02 до 17,18 мас. %. Встановлено, що на дні піттінґа інтенсивність селективного розчинення металів зростала у такій послідовності: Mg, Zn, Nd, Zr. За таких

умов поверхня піттінґа тут збагачувалася Маґнієм і збіднювалася Zn, Nd, Zr. Це сприяло твердофазній дифузії атомів Маґнію в об'єм стопу, а Zn, Nd і Zr — до поверхні піттінґа. Це підтримувало анодні процеси, які забезпечувалися катодними реакціями відновлення водню на їхній поверхні. Виявлено, що на поверхні піттінґа тут зменшився вміст Оксиґену до 1,92...7,8 мас.%. Це показало, що на бічній поверхні піттінґа пасивна плівка щільніша, ніж на його дні. Доведено, що піттінґи на поверхні стопу NZ30K репасивувалися, а отже, його можна розглядати як конструкційний матеріял для виробництва біорозкладних імплантів.

Ключові слова: піттінґова корозія, стоп NZ30K, розчин Рінґера–Локка, селективне розчинення металів у піттінґах на стопі NZ30K, біорозкладний імплант зі стопу NZ30K.

(Received 13 August, 2025; in final version, 12 November, 2026)

1. INTRODUCTION

Today, magnesium alloys are used to produce biodegradable implants for surgical treatment in traumatology [1]. However, they often have poor mechanical and biological properties that can be improved by various alloying methods [2–5]. In particular, Mg–Ca alloy is produced to increase bone integration with calcium, which promotes bone formation during implant biodegradation [6–8]. At the same time, it can form MgCa intermetallic inclusions, which are the focus of local corrosion, which is unacceptable in the treatment of broken bones using biodegradable implants [9–11]. At the same time, the mechanisms of these local corrosion processes remain controversial, which 'slows down' the solution of this problem and the use of these alloys in the production of biodegradable implants [12–17]. At the same time, Al–Ca-doped magnesium alloys can contribute to biological complications in fracture treatment, including muscle destruction, reduced osteoclastogenesis, and Alzheimer's disease [18]. Magnesium alloys alloyed with Zn, Zr, Nd and Ag do not have these disadvantages [19, 20]. In addition, Zn and Nd increase their strength and relative elongation, and Zr promotes grain refinement, which increases their specific shock absorption capacity and resistance to shock loads [19]. The resistance of the NZ30K alloy to the activating effect of chloride ions in the Ringer-Locke solution is provided mainly by zinc-containing oxide films on its surface, which, under certain conditions, can lead to pitting and ulcer corrosion with the formation of corrosion pores and channels under them. They are known [21, 22] to be caused by the solid-phase diffusion of atoms of the main components of steels and alloys.

Therefore, we investigated the characteristic features of the selective dissolution of NZ30K alloy in Ringer–Locke solution to substantiate the possibility of its use in the production of biodegradable im-

plants.

2. EXPERIMENTAL/THEORETICAL DETAILS

We studied samples of magnesium alloy NZ30K smelted in an induction crucible furnace and subjected to ageing [23]. The diameter of the samples was 12 and the length was 30 mm. Their chemical composition was determined by the x-ray spectral method using the JNKA ENERGY 350. The chemical composition of the studied samples is shown in Table 1.

Corrosion tests of the samples were carried out in a Ringer–Locke solution (an aqueous solution of undissociated water with the following chemical reagents, in [mg/l]: NaCl—9; $NaHCO_3$, $CaCl_2$, KCl—0.2 for each reagents; $C_6H_{12}O_6$—1) at a temperature of 20 ± 1°C. The surface of corrosion damage on the samples after their testing in Ringer–Locke's solution was examined using an optical microscope MMR-2P and a scanning electron microscope INKA ENERGY 350 with an energy dispersive microanalyser to determine the chemical composition of the alloy in local characteristic damage. The features of selective dissolution of the alloy components were evaluated by their selective dissolution coefficients Z_{Zn}, Z_{Zr}, and Z_{Nd}, which have been determined by the formula:

$$Z_{(Zn,Zr,Nd)} \frac{\Delta(Zn, Zr, Nd) \times Mg}{\Delta Mg \times C_{(Zn,Zr,Nd)}},$$

where $Z_{(Zn,\ Zr,\ Nd)}$ are the coefficients of selective dissolution of Zn, Zr and Nd, Δ(Zn, Zr, Nd) is the difference between the content of the corresponding alloying element in the alloy in the initial state and after corrosion tests in Ringer–Locke solution, wt.%; Mg—magnesium content in the alloy in the initial state, wt.% (Table 1); ΔMg is the difference between the content of Mg in the alloy in the initial state and after corrosion tests in Ringer–Locke solution, wt.%; $C_{(Zn,\ Zr,\ Nd)}$ is the content of Zn, Zr and Nd in the alloy in the initial state, wt.% (Table 1).

The chemical composition of the NZ30K alloy in pittings is presented in Table 2.

The calculated coefficients of selective dissolution of NZ30K alloy components are given in Table 3.

TABLE 1. Chemical composition of the studied samples.

Alloy	Content of chemical elements, wt.%			
NZ30K	Mg	Zn	Zr	Nd
	95.67	0.67	0.89	2.77

TABLE 2. Chemical composition of characteristic places on the surface of NZ30K alloy in pitting after corrosion tests in Ringer–Locke solution.

№	Location on the alloy surface	Content of chemical elements, wt.%				
		Mg	Zn	Zr	Nd	O
1	Fig. 2*a*, spectrum 1	78.08	1.70	0.67	0.00	17.18
		Cl = ±0.88 wt.%, Ca = 1.49 wt.%				
2	Fig. 2*b*, spectrum 3	71.84	1.40	0.87	1.57	10.02
		Cl = 13.29 wt.%				
3	Fig. 2*c*, spectrum 4	82.57	0.00	0.26	0.00	17.17
4	Fig. 3*a*, spectrum 1	90.41	0.58	0.64	5.69	2.68
5	Fig. 3*b*, spectrum 2	96.81	0.05	1.79	0.00	1.92
6	Fig. 3*c*, spectrum 3	89.00	1.00	0.00	2.20	7.80
7	Fig. 3*d*, spectrum 4	62.54	1.11	0.00	0.00	36.35

TABLE 3. Coefficients of selective dissolution of NZ30K alloy in characteristic places.

№	Local corrosion damage of the sample	Coefficients of selective dissolution of metals in local corrosion damage		
		Z_{Zn}	Z_{Zr}	Z_{Nd}
1	Fig. 2*a*, spectrum 1	8.38	0.30	5.45
2	Fig. 2*b*, spectrum 3	4.69	0.09	0.29
3	Fig. 2*c*, spectrum 4	7.33	5.19	7.33
4	Fig. 3*a*, spectrum 1	2.49	7.20	19.29
5	Fig. 3*b*, spectrum 2	73.73	80.58	79.68
6	Fig. 3*c*, spectrum 3	6.47	14.46	2.98
7	Fig. 3*d*, spectrum 4	1.90	2.89	2.89

3. RESULTS AND DISCUSSION

Previously, the corrosion behaviour of magnesium alloy NZ30K in Ringer–Locke solution has been studied in paper [5]. It has been found that it underwent pitting corrosion (Fig. 1).

On the surface of the pitting 0.5 mm to the left of spectrum 1 (Fig. 2*a*), a scanning electron microscope was used to record etched metal in the vicinity of irregularly shaped intermetallic inclusions.

This is most likely due to the increased corrosion activity of the metal on structural imperfections near inclusions in an aggressive corrosive media formed from hydrated corrosion products in pitting [24]. At the same time, as established in Refs. [25, 26], the nature, volume, and size of inclusions significantly affect the probability of metal activa-

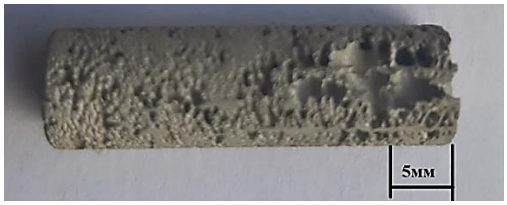


Fig. 1. Cylindrical surface of the NZ30K alloy sample subjected to pitting corrosion in Ringer–Locke solution.

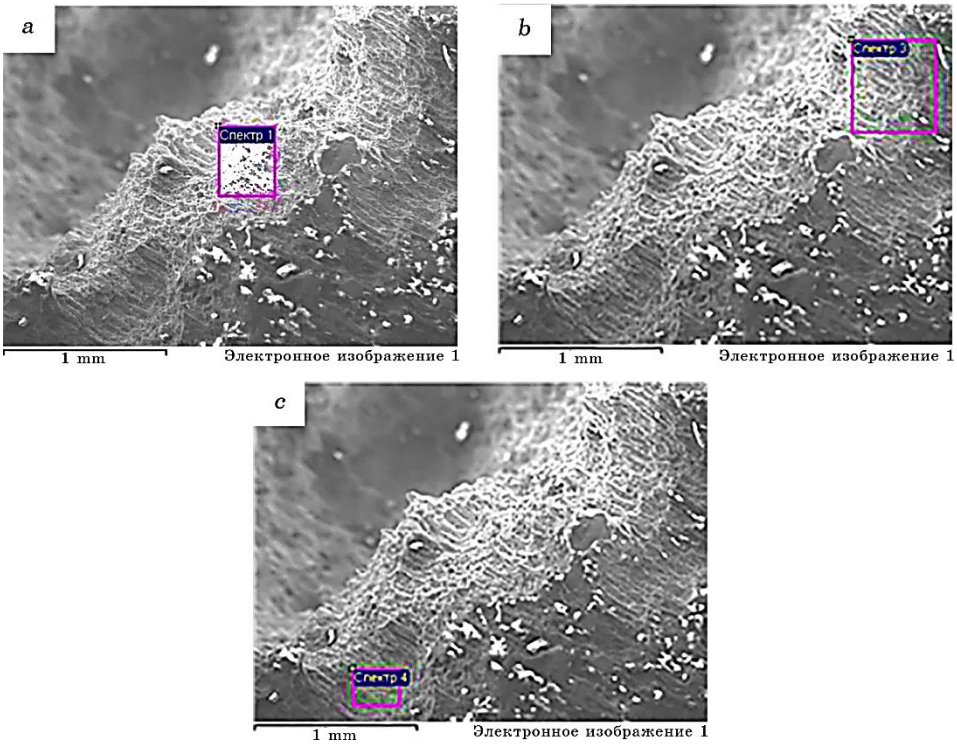


Fig. 2. Pitting surface on a sample of NZ30K alloy after testing in Ringer–Locke solution: *a*—spectrum 1, *b*—spectrum 3, *c*—spectrum 4.

tion in their vicinity, which is characterized by the peculiarities of selective alloy dissolution.

The selective nature of the alloy dissolution in pitting is confirmed by the developed microrelief of its surface, which was recorded using a scanning electron microscope (Figs. 2, 3) and the results of the analysis of the calculated coefficients of selective dissolution of $Z_{Zn,\ Zr,\ Nd}$ metals on their surface (Table 3).

In particular, from the analysis of item 1 of Table 3, it has been

found that the coefficients of selective dissolution of Zn (Z_{Zn}= 8.38) and Nd (Z_{Nd} = 5.45) are greater than one. This indicates that, in this area of the pitting (Fig. 2*a*), Zn and Nd dissolved more intensively than Mg.

Under such conditions, its surface was enriched in Mg and depleted in Zn and Nd. At the same time, it has been calculated that the coefficient Z_{Zr} <1, which indicates a more intense dissolution of Mg than Zr. This led to the fact that the pitting surface (Fig. 2*a*) was enriched in Zr and depleted in Mg. In general, it should be noted that according to the data in item 1 of Table 3, the intensity of metal dissolution in this area of the pitting increased in the following order: Zr, Mg, Nd, Zn. This tendency was supported by the solid-phase diffusion of Mg, Nd, and Zn atoms in the alloy volume to the pitting surface, and Zr in the opposite direction. The solid-phase diffusion of Mg atoms, which is the main component of the alloy, to the surface of the pitting can cause the formation of corrosion pores, channels, *etc.* under their surface. It is known [27] that the ionization of a chemical element with a negative

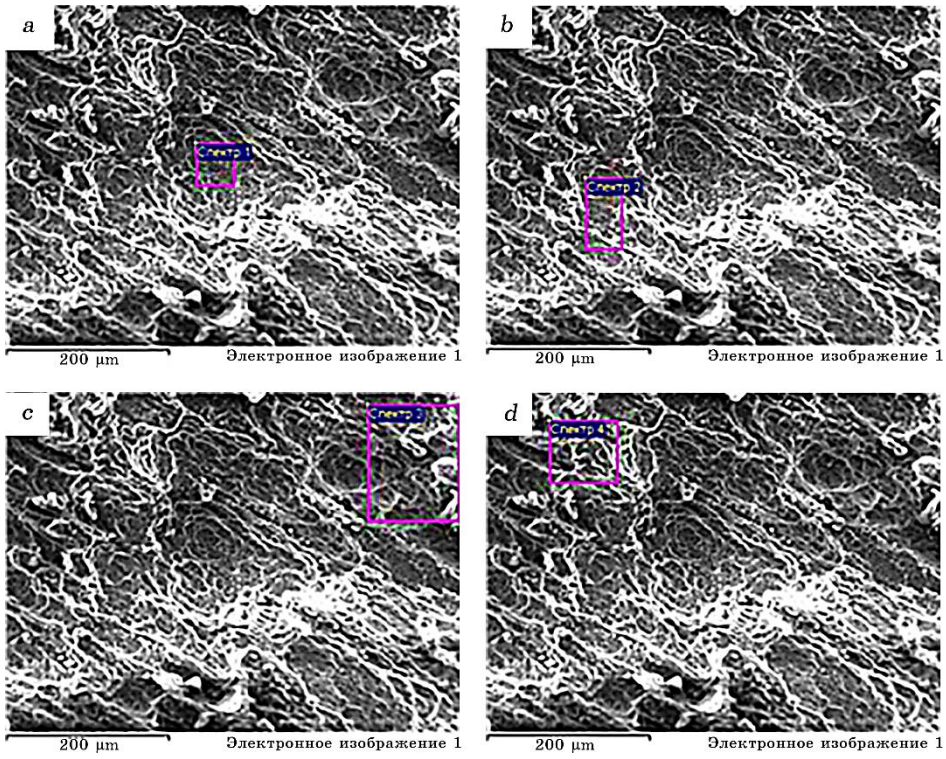


Fig. 3. Microphotography of the bottom of the pitting on the surface of the NZ30K alloy sample after testing in Ringer–Locke solution: *a*—spectrum 1; *b*—spectrum 2; *c*—spectrum 3; *d*—spectrum 4.

electrode potential on the alloy surface promotes the formation of nonequilibrium vacancies that diffuse into the alloy volume, where they coagulate and form pores. Such defects in the structure of the NZ30K alloy, alloyed with silver and clad with a layer of silver, were recorded by the authors of Ref. [20] in pitting. However, no microstructural defects associated with the solid-phase diffusion of atoms of its components in the vicinity of the pittings were observed in the pittings on the surface of the alloy under study (Figs. 2, 3). This is most likely due to the fact that the solid-phase diffusion of Mg atoms, which is the main component of the NZ30K alloy, is much slower than that of Zn and Nd atoms. At the same time, the counter-solid-phase diffusion of atoms of these chemical elements and oxygen to the pitting surface contributes to the formation of a passive film of Zn oxides. Indeed, here (Fig. 2*a*, spectrum 1), the zinc content increased to up 1.7 and oxygen up to 17.18 wt. Zinc, like chromium, is a 'valve' metal, which means that it forms passive films with semiconducting properties. The pitting resistance of steels and alloys depends on the properties of passive films [28]. It is characterized by the pitting potential [29, 30] or critical pitting temperatures [21, 22], which depend on the temperature of chloride-containing media, pH, chloride concentration, *etc.* [25, 31, 32]. At the same time, studies [21, 22, 25, 26] have established that the protective properties of passive films on the surface of passivated steels and alloys depend on the content of chromium, which is a 'valve' metal.

Most likely, the Zn content in NZ30K alloy also affects the characteristics of the passive film on its surface, which consists of Zn, Zr, and Nd oxides. Obviously, the content of these oxides in the passive film depends on the characteristics of the selective dissolution of the components of this magnesium alloy. In particular, on the surface of the pitting (Fig. 2*a*), the content of zinc oxides is maximum, and zirconium is minimal (see item 1, Table 3). The same trend was found in place (Fig. 2*b*). However, the analysis of the coefficients of selective dissolution Z_{Zn}, Z_{Zr}, and Z_{Nd} (item 2 of Table 3) revealed that Mg dissolved much more intensively from the alloy surface than Zr and Nd. After all, their selective dissolution coefficients are much less than one. It should be noted that the passive film on this alloy surface consisted mainly of Zn oxides, since the coefficient $Z_{Zn} >> 1$. Under such conditions, zinc dissolved more intensively than magnesium, and the counter-solid-phase diffusion of its atoms and oxygen on the pitting surface contributed to the formation of a passive film of zinc oxides with a slightly lower oxygen content (up to 10.02 wt.%, item 2 of Table 2). In general, from the analysis of the coefficients Z_{Zn}, Z_{Zr}, and Z_{Nd} (item 2 of Table 3), it turns out that the intensity of selective dissolution of metal atoms in the pitting (Fig. 2*b*) increased in the following order: Zr, Nd, Mg, Zn. Thus, it turns out that its surface was enriched in Zr and de-

pleted in Nd, Mg, and Zn. This contributed to the solid-phase diffusion of Zr atoms into the volume of alloy on the surface of the pitting, and Nd, Mg, and Zn atoms in the opposite direction. This nature of solid-phase diffusion usually contributes to the formation of corrosion pores, channels and tunnels, *etc.* [5, 20, 27]. After all, the dissolution of solid solutions with a high content of a component with a negative electrode potential is accompanied by surface reorganization due to solid-phase diffusion. (Standard electrode potentials: Mg = –2.37; Zn = –0.763; Zr = –1.45; Nd = –2.443 V). However, they were not found here (Fig. 2*b*). This may be due to the fact that only at potentials that exceed the critical ones, reorganization of surface layers with the formation of the above-mentioned structural defects is observed [33–35]. Such a condition for the formation of corrosion pores due to the solid-phase diffusion of the main component of the Mg alloy to the surface of the pitting is more important than the nature of the selective dissolution of metals in them. Indeed, these structural defects were not found on the studied areas of the pitting surface (Fig. 2). It should be noted that a common feature for the studied pitting areas is more intense dissolution of magnesium than zinc. Under such conditions, its surface is covered with a zinc-containing dense oxide film, which is indirectly confirmed by the consistently high oxygen content in these pitting areas (Fig. 2). This correlates with the coefficients of selective dissolution Z_{Zn} and Z_{Nd}, which are much greater than one (Fig. 2*a*, *c*) and their value in place (Fig. 2*b*) (items 1–3 of Table 2). At the same time, it should be noted that at the base of the pitting (Fig. 2*c*), its surface was rapidly repassivated, since a passive film of complex oxides of Zn, Zr, and Nd on it has been formed. This is evidenced by the coefficients Z_{Zn}, Z_{Zr}, and Z_{Nd}, which are much greater than one (item 3 of Table 3). From their analysis, it follows that the alloying elements of the alloy in the pitting were selectively dissolved in the following series: Mg, Zn, Zr, Nd. This process was supported by the solid-phase diffusion of magnesium atoms into the alloy volume, and Zn, Zr, and Nd in the opposite direction. It is known [5, 20] that such a character of solid-phase diffusion of magnesium atoms in the vicinity of pitting does not lead to the formation of the above-mentioned defects in the structure of the NZ30K alloy. At the same time, a general trend should be noted, in particular, the more intense the selective dissolution of Zn, Zr, and Nd on the pitting surface (Fig. 2) (items 1–3, Table 3), the lower the corrosion loss of magnesium in them (items 1–3, Table 2). This makes it impossible to form corrosion pores, channels, *etc.*

The selective dissolution of magnesium in pitting on the surface of NZ30K alloy in Ringer–Locke solution proceeded in stages in pairs Mg–Zn, Mg–Zr, and Mg–Nd and depended on the intensity of neodymium dissolution relative to magnesium. It has been found that the higher the value of the coefficient Z_{Nd}, the lower the corrosion loss of

Mg on the pitting surface (items 1–3 of Tables 2, 3). This is due to the fact that the standard electrode potential of Nd (–2.443 V) is more negative than that of Mg (–2.37 V). According to Refs. [27, 36–38], this is due to the fact that the less thermodynamically stable Nd dissolved selectively, accelerating the dissolution of magnesium.

The analysis of the microphotography of the bottom of the pitting (Fig. 3) showed that its surface has a developed character inherent in the selective dissolution of metals. The peculiarities of selective dissolution of the alloy are associated with the thermodynamic properties of the set of metal atoms that are in their composition [33, 39].

This is consistent with the information presented in [30, 40], since it was found that corrosion losses of steel type 18-10 decrease, and those of alloy 23–28 increase with an increase in their specific paramagnetic susceptibility χ_0. This tendency is explained by the Tammann's limit conditions, which are determined, as mentioned in [33, 39], by the thermodynamic properties of the set of metal atoms in the alloy. That is why, at the bottom of the pitting in the presence of an acidic corrosive media [41–44], more intensive dissolution of alloying elements than the main component of the NZ30K magnesium alloy has been found. Indeed, the coefficients of selective dissolution Z_{Zn} varied from 1.9 (Fig. 3.2, item 7 of Table 3) up to 73.73 (Fig. 3*b*, item 5 Table 3), Z_{Zr} from 2.89 (Fig. 3*d*, item 7 of Table 3) to 80.58 (Fig. 3*b*, item 5 of Table 3), Z_{Nd} from 2.89 (Fig. 3*d*, item 7 of Table 3) up to 79.68 (Fig. 3*b*, item 5 of Table 3). Under such conditions, the surface of the pitting bottom was mainly enriched with magnesium (Fig. 3*a*, *b*; items 4, 5 of Table 2), but it was depleted in oxygen down to 2.68 and 1.92 wt.% (items 4, 5 of Table 2). At the same time, it should be noted that the lateral surface of the pitting (Fig. 2*a*–*c*, items 1–3 of Table 2) is much more depleted in Mg than the surface at its bottom (Fig. 3*a*–*c*, items 4–6 of Table 2). This is most likely due to the lower access of oxygen to it (see items 1–6 of Table 2), which made cathodic depolarization by oxygen impossible and reduced the anodic processes of metal dissolution in the pitting, which were supported almost exclusively by cathodic processes with hydrogen depolarization. It should be noted that the anodic processes of metal dissolution in the pitting (Fig. 3), even in a small area of 500×500 μm, proceeded with different intensities. Indeed, from the analysis of the coefficients of selective dissolution of Zn, Zr, and Nd in the pitting (Fig. 3, items 4–7 of Table 3), it turns out that in the area (Fig. 3*a*) the intensity of metal dissolution in the pitting increased in the following sequence: Mg, Zn, Zr, Nd. Almost the same trend was recorded at the points (Fig. 3*b*, *d*), but at the point (Fig. 3*c*) the intensity of metal dissolution in the pitting increased in the following order: Mg, Nd, Zn, Zr. Thus, summarizing the above, it can be noted that on the entire surface at the bottom of the pitting, magnesium dissolved the slowest, which is typical for metastable pittings that are repassiv-

ated [45], and Nd and Zr mostly dissolved the most intensively. This, taking into account the information from [33, 39], could contribute to the slowdown of selective dissolution of zinc in the Mg–Zn pair and the formation of a zinc-containing oxide film on the pitting surface and its repassivation. It should be noted that at the location of spectrum 4 (Fig. 3*d*), the lowest magnesium content (62.54 wt.%) and the highest oxygen content (36.35 wt.%) were found on the pitting surface (item 7 of Table 2), which is associated with the accumulation of corrosion products here, but this did not affect the overall nature of the selective dissolution of metals.

Summarizing the above-mentioned, it can be noted that the NZ30K alloy dissolved selectively in the pitting formed during the testing of the sample in the Ringer–Locke solution. The most intense dissolution of magnesium on the side surfaces of the pitting has been recorded. This is due to the fact that here the anodic processes of selective dissolution of metals were supported by cathodic reactions of oxygen dissolved in the solution and hydrogen formed as a result of hydration of corrosion products. At the bottom of the pitting, anodic dissolution of metals was supported only by cathodic reactions of hydrogen reduction. Under such conditions, much less oxidation of the pitting surface was recorded with the formation of a passive film, which mainly consisted of zinc oxides. It has been found that the intensity of metal dissolution in the pitting increased in the following sequence: Mg, Zn, Nd, Zr. This process was supported by the solid-phase diffusion of magnesium atoms into the alloy volume, and Zn, Nd, and Zr in the opposite direction. This nature of solid-phase diffusion of the atoms of the main component of the alloy did not contribute to the formation of corrosion pores and channels, which makes it possible to consider the NZ30K alloy as a material for the production of biodegradable implants.

4. CONCLUSION

The results of corrosion tests of NZ30K alloy samples in a chloride-containing Ringer–Locke solution showed that they were subjected to pitting corrosion. It has been found that the alloy components dissolved selectively in the pitting. Energy dispersive analysis of the alloy surfaces showed that the intensity of selective dissolution of metals on the side surface of the pitting increased in the following sequence: Mg, Zr, Nd, Zn or Zr, Mg, Nd, Zn and Zr, Nd, Mg, Zn. These processes were supported by the solid-phase diffusion of zirconium atoms into the alloy volume and magnesium, neodymium, and zinc in the opposite direction, or magnesium atoms into the alloy volume and Zr, Nd, and Zn to the pitting surface. Under such conditions, a decrease in the magnesium content on the pitting surface from 95.67 down to 71.84…82.57

wt.% and its oxidation with an oxygen content of 10.02 to 17.18 wt.%. This is due to the fact that anodic processes were supported by cathodic reactions of hydrogen and oxygen reduction. It has been found that the intensity of selective dissolution of metals on the surface of the pitting bottom mainly increased in the following order: Mg, Zn, Nd, Zr. These processes were supported by the solid-phase diffusion of magnesium atoms into the alloy volume, and Zn, Nd, Zr in the opposite direction. Under such conditions, we recorded lower corrosion losses of magnesium at the bottom of the pitting (Mg content: 89.00…90.48 wt.%) than on its lateral surface and a lower degree of its oxidation (oxygen content from 1.92 to 7.8 wt.%). This is due to the fact that here the anodic processes were supported only by cathodic reactions of hydrogen reduction. Analysis of the characteristics of the selective dissolution of metals in pitting showed that they were repassivated without the formation of corrosion pores and channels, which makes it possible to consider this alloy for the production of biodegradable implants.

AUTHORS' CONTRIBUTIONS

V. L. Greshta conceived and designed the study, planned and coordinated the corrosion tests, analysed the experimental data on selective dissolution and pitting behaviour of NZ30K alloy, interpreted the results in the context of biodegradable implant applications, and wrote the main part of the manuscript. O. E. Narivskyi provided expert consultancy as a corrosion specialist, advised on the choice of testing conditions and electrochemical interpretation of pitting and selective dissolution processes, contributed to the discussion of the results with reference to current corrosion theories and literature, and critically revised the manuscript for important intellectual content. A. V. Dzhus, participated in the organisation and partial performance of corrosion experiments and microstructural/EDS studies, processed and systematized the experimental data (including Tables 1–3 and the analysis of pits morphology), contributed to the literature review and drafting individual sections of the text, and was responsible for the technical preparation and formatting of the manuscript according to the journal requirements.

All authors discussed the results, contributed to the final interpretation, and approved the final version of the manuscript.

REFERENCES

1. H. Li, Y. Zheng, and L. Qin, *Prog. Nat. Sci.-Mater. Int.*, **24**, Iss. 5: 414 (2014).
2. R.-C. Zeng, L. Sun, Y. F. Zheng, H. Z. Cui, and E.-H. Han, *Corros. Sci.*, **79**: 69 (2014).
3. R.-C. Zeng, S. Ii, L.-Y. Cui, X.-T. Li, E.-H. Han, and L. Song, *Front. Mater.*

Sci., **11**: 284 (2017).
4. Y. F. Zheng, X. N. Cu, and F. Witte, *Mater. Sci. Eng.-R-Rep.*, **77**: 1 (2014).
5. V. Greshta, O. Narivskyi, and A. Dzhus, *Eurasian Phys. Tech. J.*, **21**, Iss. 3: 6 (2024).
6. T. C. Lowe and R. Z. Valiev, *Adv. Biomater. Biodevices (Wiley Blackwell)*, p. 1 (2014).
7. J. W. Seong and W. J. Kim, *Corros. Sci.*, **98**: 372 (2015).
8. Z. Li, X. Gu, S. Lou, and Y. Zheng, *Biomaterials*, **29**, Iss. 10: 1329 (2008).
9. F. Cao, Z. Shi, G.-L. Song, M. Lui, and A. Atrens, *Corros. Sci.*, **79**: 69 (2013).
10. K. Gusieva, C. H. J. Davies, J. R. Scully, and N. Birbilis, *Int. Mater. Rev.*, **60**: 169 (2015).
11. W.-C. Kim, J.-G. Kim, J.-Y. Lee, and H.-K. Seok, *Mater. Lett.*, **62**, Iss. 25: 4146 (2008).
12. Y. Jin, C. Blawert, F. Feyerabend, J. Bohlen, M. del R. Silva Campos, S. Gavras, B. Wiese, D. Mei, M. Deng, H. Yang, and R. Willumeit, *Corros. Sci.*, **158**: 108096 (2019).
13. E. K. Brooks and M. T. Ehrensberger, *J. Funct. Biomater.*, **8**, Iss. 3: 38 (2017).
14. M. Esmaily, J. E. Svensson, S. Fajardo, N. Birbilis, G. S. Frankel, S. Virtanen, R. Arrabal, S. Thomas, and L. G. Johansson, *Prog. Mater. Sci.*, **89**: 192 (2017).
15. A. D. King, N. Birbilis, and J. R. Scully, *Electrochim. Acta*, **121**: 394 (2014).
16. M. Curioni, F. Scenini, T. Monetta, and F. Belucci, *Electrochim. Acta*, **166**: 372 (2015).
17. Y. Gao, A. Yerokhin, E. Parfenov, and A. Mathews, *Electrochim. Acta*, **149**: 218 (2014).
18. P. C. Ferreira, K. D. A. Piai, A. M. M. Takayanagui, and S. I. Segura-Mucoz, *Rev. Latino-Am. Enfermagem*, **16**, Iss. 1: 151 (2008).
19. M. D. Lastra, R. Pastelin, A. Camacho, B. Monroy, and A. E. Aguilar, *J. Trace Elem. Med. Biol.*, **15**, No. 1: 5 (2001).
20. V. Greshta, O. Narivskyi, A. Dzhus, V. Vynar, and O. Kuprin, *Int. Multidiscip. Sci. GeoConf. SGEM*, **24**, Iss. 6.1: 41 (2024).
21. O. E. Narivskyi, S. O. Subbotin, T. V. Pulina, S. O. Leoshchenko, M. S. Khoma, and N. B. Ratska, *Mater. Sci.*, **58**, Iss. 5: 1 (2023).
22. O. E. Narivskyi, S. O. Subbotin, T. V. Pulina, S. O. Leoshchenko, M. S. Khoma, and N. B. Ratska, *Mater. Sci.*, **59**, Iss. 5: 275 (2024).
23. V. L. Greshta, V. A. Shalomeev, A. V. Dzhus, and O. A. Mityaev, *New Mater. Technol. Metall. Eng.*, **2023**, Iss. 2: 14 (2023).
24. O. E. Narivs'kyi, *Fiz.-Khim. Mech. Mater.*, **41**, Iss. 1: 104 (2005).
25. O. E. Narivskyi, S. O. Subbotin, and T. V. Pulina, *Phys. Sci. Technol.*, **10**, Iss. 3–4: 48 (2023).
26. A. V. Dzhus, O. E. Narivskyi, S. A. Subbotin, T. V. Pulina, G. V. Snighnoi, and S. D. Leoshchenko, *Metallofiz. Noveishie Tekhnol.*, **46**, No. 4: 371 (2024).
27. J. O. Fritz and H. W. Pickering, *J. Electrochem. Soc.*, **138**, Iss. 11: 3209 (1991).
28. L. Martinez, B. Malki, G. Berthome, B. Baroux, and F. Perez, *Surf. Coat. Technol.*, **201**: 1671 (2006).
29. C. Alonso, M. Castellote, and C. Andrade, *Electrochim. Acta*, **47**: 3469 (2002).
30. O. E. Narivs'kyi, G. V. Snizhnoi, T. V. Pulina, V. L. Snizhnoi, and N. A. Solidor, *Mater. Sci.*, **59**, Iss. 3: 649 (2024).
31. G. Wranglen, *Mater. Sci. Appl.*, **6**, Iss. 4: 62 (2015).
32. Q. Zhang, R. Wang, M. Kato, and K. Nakasa, *Scripta Mater.*, **52**: 227 (2005).

33. V. V. Losev and A. P. Pchelnikov, *Results of Sci. Technol. Electrochemistry*, **15**: 62 (1979) (in Russian).
34. T. P. Moffat, F.-R. F. Fan, and A. J. Bord, *J. Electrochem. Soc.*, **138**, No. 11: 3224 (1991).
35. N. D. Tomashov, *Teoriya Korrozii i Zashchita Metallov* [Corrosion Theory and Protection of Metals] (Moskva: AN USSR: 1959) (in Russian).
36. I. D. Zartsyn, A. E. Shugurov, and I. K. Marshakov, *Zashchita Metallov*, **33**, No. 5: 453 (1997) (in Russian).
37. A. V. Plaskaev and V. M. Knizheva, *Proc. 12th Perm Conf. Corros. Prot. Metals* (1990).
38. M. Pourbaix, *Atlas of Electrochemical Equilibrium in Aqueous Solutions* (Oxford: Pergamon Press: 1974).
39. N. V. Vyazovikina, *Electrochemistry*, **28**, No. 6: 917 (1992).
40. A. V. Dzhus, O. E. Narivskyi, G. V. Snizhnoi, T. V. Pulina, and V. L. Snizhnoi, *Metallofiz. Noveishie Tekhnol.*, **46**, No. 8: 739 (2024).
41. A. Narivskiy, G. Yar-Mukhamedova, E. Temirgaliyeva, M. Mukhtarova, and Y. Yar-Mukhamedov, *Int. Multidiscip. Sci. GeoConf. SGEM*, **1**: 63 (2016).
42. E. G. Wenn and R. C. Alkire, *J. Electrochem. Soc.*, **149**: 280 (2002).
43. H. Krawiec, V. Vignal, O. Heintz, and R. Altra, *Electrochim. Acta*, **51**, Iss. 16: 3235 (2006).
44. G. Lang, M. Ujvari, and G. Horanyi, *Corros. Sci.*, **45**, Iss. 1: 1 (2003).
45. O. Narivs'kyi, R. Atchibayev, A. Kemelzhanova, G. Yar-Mukhamedova, G. Snizhnoi, and S. Subbotin, *Eurasian Chem.-Technol. J.*, **24**, No. 4: 295 (2022).

Metallophysics and Advanced Technologies
Металофіз. новітні технол.
Metallofiz. Noveishie Tekhnol.
2026, vol. 48, No. 9, pp. 999–1010
https://doi.org/10.15407/mfint.48.09.0999
Reprints available directly from the publisher

© 2026 G. V. Kurdyumov Institute for Metal Physics,
National Academy of Sciences of Ukraine
Published by license under
the G. V. Kurdyumov Institute for Metal Physics–
N.A.S. of Ukraine Publishers imprint.
Printed in Ukraine.

PACS numbers: 07.05.Fb, 61.66.Fn, 68.37.Hk, 68.55.Nq, 72.20.Pa, 72.40.+w, 81.15.Cd

Fabrication and Characterization of CuO/Cu_2O Thin-Film Heterostructures on Si/ZnO Substrates *via* Magnetron Sputtering for Photovoltaic Applications

I. O. Kosimov[*], Sh. T. Khozhiev[*,**], K. T. Dovranov[***],
M. A. Davlatov[****], F. F. Arzikulov[**,******], U. Kh. Kholiqov[*****]

[*]*O. S. Sodikov Institute of Bioorganic Chemistry,*
Academy of Sciences of the Uzbekistan Republic,
83 Mirzo Ulugbek Ave.,
UZ-100125 Tashkent, Republic of Uzbekistan
[**]*Tashkent State Medical University,*
2 Farabi Str.,
UZ-100109 Tashkent, Republic of Uzbekistan
[***]*Karshi State University,*
17 Kuchabag Str.,
UZ-180119 Karshi, Republic of Uzbekistan
[****]*Karshi State Technical University,*
225 Mustaqillik Ave.,
UZ-180100 Karshi, Republic of Uzbekistan
[*****]*Termez State University of Engineering and Agricultural Technologies,*
228A Islom Karimov Str.,
UZ-190100 Termez, Republic of Uzbekistan

In this work, CuO and Cu_2O thin-film heterostructures are fabricated on Si/ZnO substrates using the magnetron sputtering technique under varying substrate preparation conditions. The deposition process is performed in three modes: without substrate heating, with heating at 600°C, and with

Corresponding author: Isroil Odinaevich Kosimov
E-mail: isroilkosimov@list.ru

Citation: I. O. Kosimov, Sh. T. Khozhiev, K. T. Dovranov, M. A. Davlatov, F. F. Arzikulov, and U. Kh. Kholiqov, Fabrication and Characterization of CuO/Cu_2O Thin-Film Heterostructures on Si/ZnO Substrates *via* Magnetron Sputtering for Photovoltaic Applications, *Metallofiz. Noveishie Tekhnol.*, **48**, No. 9: 999–1010 (2026), DOI: 10.15407/mfint.48.09.0999

© Publisher PH 'Akademperiodyka' of the NAS of Ukraine, 2026. This is an open access article under the CC BY-ND license (https://creativecommons.org/licenses/by-nd/4.0)

heating at 600–800°C followed by glow discharge ion cleaning. Comprehensive characterization is carried out to investigate the crystallinity, phase composition, surface morphology, and optical properties of the films. X-ray diffraction (XRD) analysis reveals that high-temperature heating combined with ion cleaning results in well-crystallized, dense, and smooth films with a pure-phase composition. Particularly, Cu_2O films grown on ion-cleaned substrates at 800°C exhibited 100% crystalline-phase formation. Scanning electron microscopy (SEM) and energy-dispersive spectroscopy (EDS) confirmed the uniform distribution of nanosize grains, while Raman spectroscopy validated the phase identification of CuO and Cu_2O. The results indicate that optimizing substrate temperature and surface pretreatment significantly enhances the structural and optical quality of copper-oxide semiconductor layers. The fabricated CuO/Cu_2O heterostructures demonstrate strong potential for use in efficient and environmentally friendly solar-cell devices.

Key words: CuO, Cu_2O, thin films, magnetron sputtering, heterostructures, crystallinity, SEM, Raman spectroscopy, solar cells.

У цій роботі тонкоплівкові гетероструктури CuO і Cu_2O були виготовлені на підкладинках Si/ZnO за допомогою методи магнетронного напорошення за різних умов підготовки підкладинки. Процес осадження проводився у трьох режимах: без нагрівання підкладинки, з нагріванням до 600°C та з нагріванням до 600–800°C із подальшим очищенням йонами жеврійного розряду. Було проведено всебічну характеризацію для дослідження кристалічности, фазового складу, морфології поверхні й оптичних властивостей плівок. Рентґенівська дифракційна аналіза (XRD) показала, що високотемпературний нагрів у поєднанні з йонним очищенням приводить до формування добре кристалізованих, щільних і гладких плівок із чистим фазовим складом. Зокрема, плівки Cu_2O, вирощені на очищених йонами підкладинках за 800°C, продемонстрували формування 100% кристалічної фази. Сканувальна електронна мікроскопія (CEM) та енергодисперсійна спектроскопія (EDS) підтвердили рівномірний розподіл нанорозмірних зерен, а Раманова спектроскопія верифікувала фазову ідентифікацію CuO та Cu_2O. Результати свідчать, що оптимізація температури підкладинки та попереднє оброблення поверхні істотно підвищує структурну й оптичну якість напівпровідникових шарів оксиду Купруму. Створені гетероструктури CuO/Cu_2O демонструють високий потенціял для використання у високоефективних та екологічно чистих сонячних елементах.

Ключові слова: CuO, Cu_2O, тонкі плівки, магнетронне розпорошення, гетероструктури, кристалічність, CEM, Раманова спектроскопія, сонячні елементи.

(Received 16 August, 2025; in final version, 16 June, 2026)

1. INTRODUCTION

In the modern era, the generation, storage, and efficient transmission of energy remain among the most critical global challenges. Research

efforts in this domain are largely focused on the development of cost-effective and high-performance materials for energy producing, storing, and delivery systems.

Over the past several decades, copper (Cu) has been extensively employed in semiconductor technology as a contact metal. Replacing aluminium, which was previously dominant, copper has become an essential component in high-temperature-resistant semiconductor devices. Notably, copper atoms possess a significantly higher diffusion coefficient in materials such as silicon and germanium [1].

Copper (I) oxide (CuO) has emerged as a promising candidate for solar cell applications. This is attributed to its high optical absorption coefficient, excellent chemical and thermal stability, nontoxic nature, lower production cost compared to materials like Ni, Ag, and Au, natural abundance, and outstanding optical, electrical, magnetic, and catalytic properties [2–5].

Although magnetron sputtering has previously been used to fabricate CuO and Cu_2O thin films [6–8], the present work reports, for the first time, the growth of such films on Si substrates preheated to 600°C and subjected to glow discharge ion cleaning prior to deposition. Copper oxide thin films can be synthesized using various techniques, including sol–gel, pulsed laser deposition, pyrolysis, chemical vapour deposition, and magnetron sputtering (the latter being particularly advantageous for achieving uniform surface morphology) [11–18].

In this study, CuO/ZnO/Si and Cu_2O/ZnO/Si heterostructures were fabricated *via* magnetron sputtering, with the ZnO/Si substrates preheated to 600°C and cleaned by glow-discharge ion bombardment. The effects of thermal treatment and gamma irradiation on the structural and morphological characteristics of the heterostructures were examined using x-ray diffraction phase analysis, scanning electron microscopy, and complementary characterization techniques.

2. EXPERIMENTAL/THEORETICAL DETAILS

The effect of thermal treatment on the electronic properties of Cu_2O/ZnO heterostructures grown by the magnetron sputtering method was investigated. In the heterojunction, ZnO was employed as a *p*-type and Cu_2O as an *n*-type semiconductor. To achieve surface uniformity and smoothness, an optimal regime was developed for heating the Si substrate to 600°C followed by cleaning under glow-discharge ion bombardment. The samples were deposited using a direct-current magnetron sputtering system, with a copper (Cu) target in an $Ar–O_2$ inert gas mixture (Fig. 1).

In this study, CuO and Cu_2O thin films were deposited onto Si/ZnO substrates under three different experimental conditions in an $Ar–O_2$ inert gas atmosphere using a Cu target:

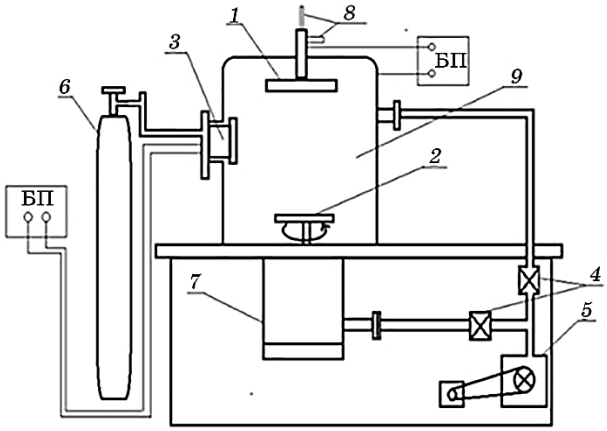


Fig. 1. Schematic diagram of the magnetron sputtering system: *1*—magnetron, *2*—target, *3*—ionizer, *4*—solenoid valve, *5*—fore pump, *6*—gas cylinder, *7*—diffusion pump, *8*—cooling system, *9*—vacuum chamber.

Condition 1—direct deposition without any pre-treatment of the substrate;
Condition 2—deposition after heating the substrate to 600°C;
Condition 3—deposition after heating the substrate to 600°C and performing glow discharge ion cleaning.

The crystallographic structure of the thin films prepared under these three conditions was examined using x-ray diffraction (Rigaku), while the degree of crystallinity and crystallite size were determined by x-ray phase analysis. Surface morphology, layer formation, and emission characteristics were studied using scanning electron microscopy (SEM). Structural changes and material characteristics were further analysed *via* Raman spectroscopy [19]. In addition, the electrical and optical properties of the films were systematically evaluated.

3. RESULTS AND DISCUSSION

In this study, a single-layer epitaxial structure KDP 0.5–1bk 2(III) standard silicon substrate was used. The x-ray phase analysis of this substrate is shown in Fig. 2, where characteristic diffraction peaks corresponding to silicon were observed at diffraction angles $2\theta \cong 28.5°$, 48.2°, 57.3°, 69.8°, and 76.7°, with interplanar spacings $d_{hkl} \cong 3.13$ Å, 1.91 Å, 1.63 Å, 1.35 Å, and 1.24 Å, respectively, corresponding to Miller indices (*hkl*) of (111), (202), (311), (400), and (313).

From these results, it can be concluded that the absence of additional phase peaks confirms the high purity of the silicon substrate. Initially, the Si substrate was heated to 300°C, and under identical deposition

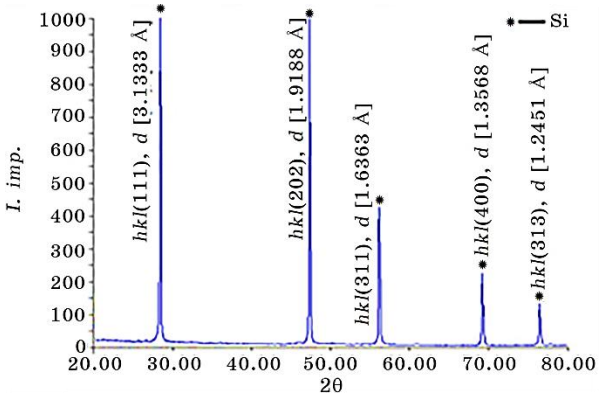


Fig. 2. X-ray phase analysis of the Si substrate sample.

conditions, three identical thin ZnO layers were grown on its surface using the magnetron sputtering method. The x-ray phase analysis of the ZnO-coated sample is shown in Fig. 3, while the SEM images are presented in Fig. 4 (*a*–*c*), and the EDS analysis in Fig. 5.

The x-ray phase analysis in Fig. 3 shows that in the Si/ZnO sample, the diffraction peaks of the Si phase were observed at $2\theta \cong 28.5°$ and 69.2°, corresponding to interplanar spacings $d_{hkl} \cong 3.13$ Å and 1.36 Å, with Miller indices (111) and (400), respectively. The ZnO phase exhibited diffraction peaks at $2\theta \cong 31.8°$, 34.4°, 36.3°, 47.5°, 56.6°, 62.8°, 66.4°, 68.0°, 69.1°, and 77.0°, corresponding to $d_{hkl} \cong 2.81$ Å, 2.60 Å, 2.47 Å, 1.91 Å, 1.24 Å, 1.48 Å, 1.41 Å, 1.38 Å, 1.24 Å, and Miller indices (100), (002), (101), (012), (110), (013), (200), (112), and (202), re-

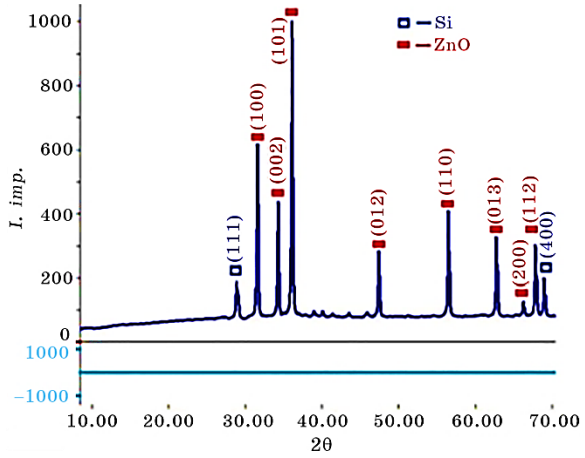


Fig. 3. X-ray phase analysis of the ZnO thin film grown on the Si substrate under identical deposition conditions by magnetron sputtering.

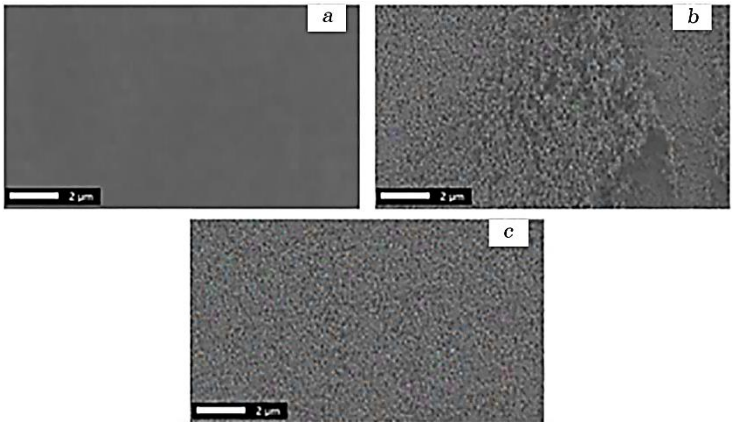


Fig. 4. SEM micrographs: *a*—Si substrate; *b*—Si/ZnO grown at 300°C; *c*—Si/ZnO grown at 600°C.

spectively.

Figure 4 (*a*–*c*) presents the SEM images of Si/ZnO samples grown under three different conditions: without heating, heated to 300°C, and heated to 600°C prior to ZnO deposition. In Figure 4*a*, corresponding to the unheated Si substrate with a ZnO thin film, the surface appears smooth and uniformly arranged. In Figure 4*b*, representing the sample grown at 300°C, the SEM image shows that ZnO nanoparticles are irregularly shaped and unevenly distributed over the surface. In contrast, Fig. 4*c*, corresponding to growth at 600°C, reveals a well-ordered surface morphology with good adhesion, where dense, spherical structures are formed. The surface is fully covered with uniformly distributed, pure-phase ZnO nanoparticles of similar size.

This observation is further supported by the EDS analysis in Fig. 5, which shows that the surface composition for ZnO is approximately: 35 at.% O and 65 at.% Zn, corresponding to mass percentages of 11.6% O

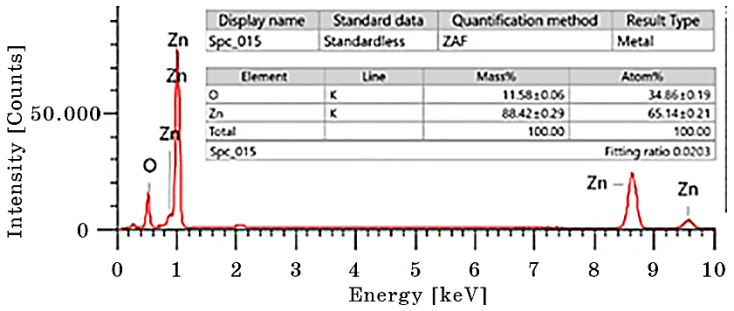


Fig. 5. EDS spectrum of the ZnO thin film grown on the Si substrate.

and 88.4% Zn.

The x-ray quantitative phase analysis of the Si/ZnO structure (Fig. 6*a*) revealed elemental contents of 74.6% Zn, 18.2% O, and 7.2% Si. As shown in Table 1, the average crystallite size, calculated using the Debye–Scherrer equation, was found to be approximately 28–35 nm. These results indicate that heating the substrate to 600°C prior to ZnO nanolayer deposition *via* magnetron sputtering is the most favourable condition. Under this regime, the substrate surface becomes well ordered, exhibits strong adhesion, and develops dense spherical structures, leading to complete coverage by a pure-phase ZnO thin film.

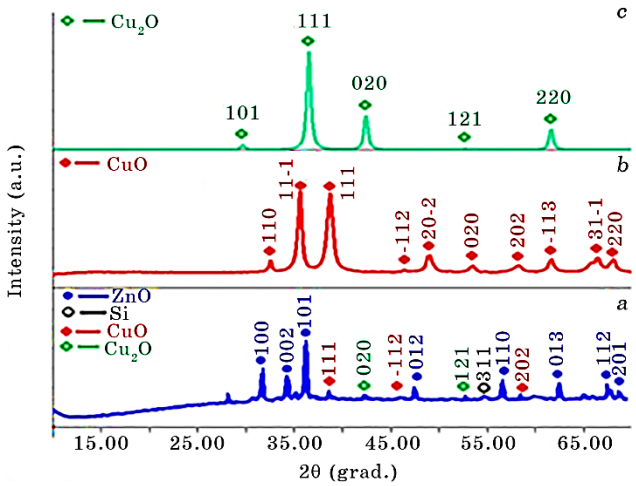


Fig. 6. XRD patterns of CuO and Cu_2O thin films grown on Si/ZnO substrates under different conditions: (*a*) without heating, (*b*) heated to 500°C, and (*c*) heated to 800°C with pre-cleaning by glow discharge ions.

TABLE 1. Quantitative phase and elemental composition of thin films grown on Si/ZnO under different conditions.

Sample/Condition	Elemental composition (%)	Phase composition (%)	Crystallite size (nm)
Si/ZnO (substrate)	Zn — 74.6, O — 18.2, Si – 7.2	ZnO — 100	28–35
Si/ZnO/CuO, no heating	Cu — 4.5, Zn — 56.9, O — 14.9, Si — 23.6	CuO — 1, Cu_2O — 4.6, ZnO — 70.9, Si — 23.6	≅14
Si/ZnO/CuO, 800°C	Cu — 79.9, O — 20.1	CuO — 100	≅14
Si/ZnO/ Cu_2O, 800°C	Cu — 88.8, O — 11.2	Cu_2O — 100	≅14

The main objective of this study was to deposit a thin copper oxide layer on the Si/ZnO surface prepared under the above conditions and to investigate its potential application in solar cells. To achieve this goal, the following experiments were conducted: CuO and Cu_2O thin films were grown on Si/ZnO samples under three different conditions, as shown in Fig. 6: *a*—without heating, *b*—heated to 500°C, and *c*—heated to 800°C. The x-ray phase analysis of the CuO and Cu_2O samples was used to determine their interplanar spacings, Miller indices, average crystallite sizes, quantitative and qualitative phase compositions, and degrees of crystallinity and amorphousness.

When CuO and Cu_2O thin layers were deposited on the Si/ZnO film surface without heating (Fig. 6*a*), the resulting layers were weakly bonded to the substrate, and numerous ZnO peaks were still visible in the XRD pattern. For the CuO sample grown at 800°C (Fig. 6*b*), the diffraction peaks were observed at $2\theta \cong 32.5°$, 35.5°, 38.7°, 48.8°, 53.4°, 58.2°, and 61.6°, corresponding to interplanar spacings $d_{hkl} \cong 2.75$ Å, 2.52 Å, 2.32 Å, 1.86 Å, 1.71 Å, 1.58 Å, and 1.50 Å, respectively. For Cu_2O (Fig. 6*c*), the diffraction peaks were found at $2\theta \cong 29.6°$, 36.2°, 42.4°, 52.6°, 61.5°, and 69.8°, with d_{hkl} values of approximately 3.01 Å, 2.46 Å, 2.13 Å, 1.74 Å, 1.50 Å, and 1.35 Å, respectively. In addition to peak identification, the amorphous–crystalline phases, quantitative phase composition, and qualitative phase analysis of CuO and Cu_2O are presented in Fig. 7.

Figure 7 shows the quantitative and qualitative phase analyses for: *a*—the Si/ZnO substrate, *b*—CuO and Cu_2O films deposited on Si/ZnO without heating, *c*—CuO films grown at 800°C, and *d*—Cu_2O films grown at 800°C. When CuO and Cu_2O were deposited without substrate heating (Fig. 7*b*), the quantitative analysis revealed elemental compositions of 4.5% Cu, 23.6% Si, 56.9% Zn, and 14.9% O. The qualitative phase analysis showed 1% CuO, 4.55% Cu_2O, 70.9% ZnO, and 23.6% Si. In contrast, when the substrate was heated to 800°C, the CuO sample (Fig. 7*c*) had a quantitative composition of 79.9% Cu and 20.1% O, with 100% CuO phase purity. Similarly, the Cu_2O sample (Fig. 7*d*) had a quantitative composition of 88.8% Cu and 11% O, with 100% Cu_2O phase purity (Table 1).

For the CuO thin films grown on Si/ZnO, the crystallite size was found to be approximately 14 nm, indicating the formation of nanostructured layers. When the samples were heated to 500°C and 600°C, the surface roughness gradually decreased, resulting in a smoother morphology. At 600°C, a uniformly ordered thin film composed of homogeneously distributed nanoparticles was successfully obtained.

Analysis of the spectrum in Fig. 9 obtained using the Raman spectroscopy method reveals three peaks corresponding to CuO at vibrational frequencies of 301, 363, and 623 cm^{-1}. In addition, peaks char-

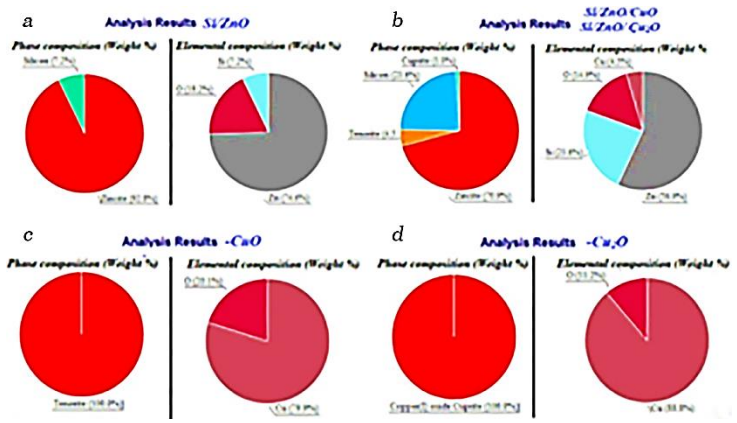


Fig. 7. Quantitative phase composition analysis of (*a*) Si/ZnO, (*b*) Si/ZnO/CuO and Si/ZnO/Cu_2O, (*c*) CuO, and (*d*) Cu_2O.

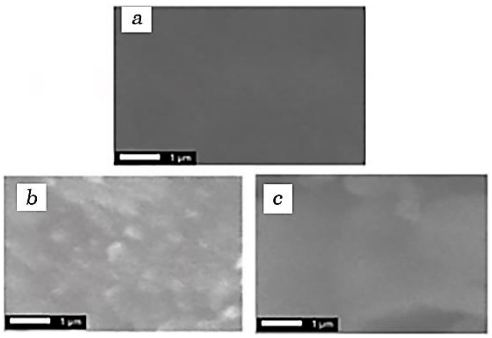


Fig. 8. SEM micrographs of: (*a*) CuO grown without substrate heating, (*b*) CuO grown at 500°C, and (*c*) Cu_2O grown at 800°C after glow-discharge ion cleaning of the substrate.

acteristic of Cu_2O at vibrational frequencies of 114, 141, 165, and 218 cm^{-1} are observed, which are associated with changes in microstructure or phase transitions induced by heating. The maximum positions of these peaks correspond to reported values for CuO [16], confirming that the chemical composition of the investigated element matches CuO. The peaks appearing after heating copper oxide to 800°C may be related to modifications in the crystal structure of CuO and Cu_2O, and indicate the coexistence of crystalline and amorphous-crystalline phases, as also shown in Fig. 10 and Table 2.

When the grown thin films of CuO and Cu_2O were examined separately using a Rigaku Oxford diffraction system (XtaLAB Synergy-i), the crystallographic structures and lattice parameters were determined as follows: for CuO, monoclinic $C12/c1$ with $a = 4.6832$ Å,

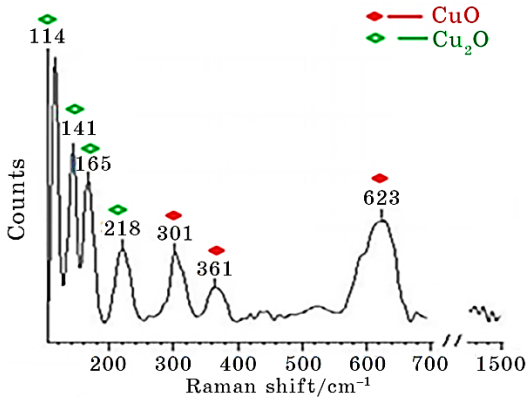


Fig. 9. Raman spectrum of copper oxide grown on the Si/ZnO surface *via* magnetron sputtering.

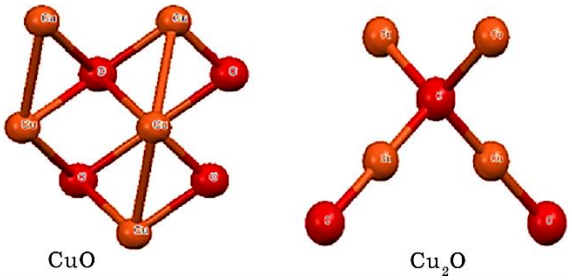


Fig. 10. X-ray structural analysis of CuO and Cu_2O thin films grown on the Si/ZnO surface.

TABLE 2. Crystallographic parameters of CuO and Cu_2O thin films grown on Si/ZnO.

Material	Crystal system	Space group	Lattice parameters (Å)	Main diffraction peaks (2θ, °)	Raman active modes (cm^{-1})
CuO	Monoclinic	$C12/c1$	$a = 4.6832$, $b = 3.4288$, $c = 5.1297$	32.5, 35.5, 38.7, 48.8, 53.4, 58.2, 61.6	301, 363, 623
Cu_2O	Cubic	$Pn{-}3m$	$a = 4.2580$	29.6, 36.2, 42.4, 52.6, 61.5, 69.8	114, 141, 165, 218

$b = 3.4288$ Å, and $c = 5.1297$ Å; for Cu_2O, cubic $Pn{-}3m$ with $a = 4.2580$ Å.

4. CONCLUSION

In this study, CuO and Cu_2O thin-film heterostructures were fabricated on Si/ZnO substrates using the magnetron sputtering method. Experiments were carried out under three different conditions: without heating, with substrate heating at 600°C, and with heating at 600–800°C followed by surface cleaning using glow discharge ions. The crystallinity, phase composition, morphology, as well as the electrophysical and optical properties of the obtained layers were thoroughly investigated. The analyses revealed that substrate preheating at high temperatures combined with ion cleaning significantly enhanced crystallinity, resulting in smooth, dense structures with a pure phase composition. In particular, for Cu_2O layers grown on ion-cleaned surfaces at 800°C, a 100% crystalline phase was achieved. SEM and EDS analyses, along with Raman spectroscopy, confirmed these findings. The results demonstrate that appropriate temperature control and surface pretreatment can substantially improve the quality of copper oxide semiconductor layers. Consequently, the fabricated CuO/Cu_2O heterostructures can be proposed as promising materials for the development of efficient and environmentally friendly solar cells.

AUTHORS' CONTRIBUTIONS

I. O. Kosimov conceived the research idea and led the research. carried out the electronic structure using theoretical calculations. Sh. T. Khozhiev developed the project, reviewed the literature and collected data on electronic and mechanical properties, supervised the results of this work and wrote the manuscript taking into account the contributions of all authors. K. T. Dovranov supervised the project, developed the main conceptual ideas, checked the analytical approaches and provided critical feedback. M. A. Davlatov conducted thin-film deposition experiments and contributed to the analysis of electrophysical properties. F. F. Arzikulov participated in the experimental design and preparation of samples. U. Kh. Kholikov performed experimental work and thin film deposition and performed structural, optical analysis. All authors approved the final version of the manuscript.

REFERENCES

1. T. Minami, Y. Nishi, T. Miyata, and J. I. Nomoto, *Appl. Phys. Express*, **4**, No. 6: 062301 (2011).
2. A. Mittiga, E. Salza, F. Sarto, M. Tucci, and R. Vasanthi, *Appl. Phys. Lett.*, **88**, No. 16: 163502 (2006).
3. M. Izaki, T. Shinagawa, K. T. Mizuno, Y. Ida, M. Inaba, and A. Tasaka, *J. Phys. D: Appl. Phys.*, **40**, No. 11: 3326 (2007).

4. S. S. Jeong, A. Mittiga, E. Salza, A. Masci, and S. Passerini, *Electrochim. Acta*, **53**, No. 5: 2226 (2008).
5. M. Izaki, K. T. Mizuno, T. Shinagawa, M. Inaba, and A. Tasaka, *J. Electrochem. Soc.*, **153**, No. 9: C668 (2006).
6. K. Fujimoto, T. Oku, T. Akiyama, and A. Suzuki, *J. Phys.: Conf. Ser.*, **433**: 012024 (2013).
7. K. Nakaoka and K. Ogura, *J. Electrochem. Soc.*, **149**, No. 11: C579 (2002).
8. K. Fujimoto, T. Oku, and T. Akiyama, *J. Ceram. Soc. Jpn.*, **119**, No. 1390: 402 (2011).
9. T. Oku, T. Noma, A. Suzuki, K. Kikuchi, and S. Kikuchi, *J. Phys. Chem. Solids*, **71**, No. 4: 551 (2010).
10. T. Oku, R. Motoyoshi, K. Fujimoto, T. Akiyama, B. Jeyadevan, and J. Cuya, *J. Phys. Chem. Solids*, **72**, No. 11: 1206 (2011).
11. M. I. Domnina, S. K. Filatov, I. Zyuzyukina, and L. P. Vergasova, *Neorg. Mater.*, **22**: 1743 (1986).
12. M. A. Davlatov, K. T. Davranov, X. T. Dovranov, S. N. Xusanov, A. R. Kodirov, and S. Xolikulova, *East Eur. J. Phys.*, **2**: 330 (2025).
13. H. Kidowaki, T. Oku, and T. Akiyama, *J. Phys.: Conf. Ser.*, **352**: 012022 (2012).
14. T. Oku, A. Takeda, A. Nagata, K. Fujimoto, T. Akiyama, and A. Suzuki, *J. Phys.: Conf. Ser.*, **352**: 012024 (2012).
15. K. T. Dovranov, M. Vinnichenko, M. Normuradov, X. Davranov, D. Nabiyev, M. Davlatov, A. Kodirov, P. Parmonov, and N. Kurbonov, *Proc. Int. Conf. Electrical Engineering and Photonics (EExPolytech)* (2024), p. 308.
16. T. Oku, A. Takeda, A. Nagata, R. Motoyoshi, K. Fujimoto, T. Noma, and E. Ōsawa, *Light Harvesting Nanomaterials* (Bentham Science Publishers: 2015).
17. K. T. Dovranov, M. T. Normuradov, M. A. Davlatov, K. T. Dovranov, T. Toshev, and N. Kurbonov, *East Eur. J. Phys.*, No. 3: 350 (2024).
18. P. Engelhart, N. P. Harder, R. Grischke, A. Merkle, R. Meyer, and R. Brendel, *Prog. Photovolt. Res. Appl.*, **15**, No. 3: 237 (2007).
19. B. K. Meyer, A. Polity, D. Reppin, M. Becker, P. Hering, P. J. Klar, and C. Ronning, *Phys. Status Solidi B*, **249**, No. 8: 1487 (2012).